Nanoscale chemical and mechanical characterization of thin films: sum

frequency generation (SFG) vibrational spectroscopy at buried interfaces


Sasha Joseph Kweskin

B. S. (Brown University) 2002


A dissertation submitted in partial satisfaction of the

requirements for the degree of

Doctor of Philosophy

in

Chemistry

in the

GRADUATE DIVISION

of the

UNIVERSITY OF CALIFORNIA, BERKELEY

Committee in charge:

Professor Gabor A. Somorjai (Chair)
Professor Kyriakos Komvopoulos
Professor Phillip Geissler


Spring 2006

This dissertation of Sasha Joseph Kweskin is approved:

_____

Chair                                                                        Date

_____

                                                                             Date

_____

                                                                             Date

University of California, Berkeley

Spring 2006

Nanoscale chemical and mechanical characterization of thin films: sum

frequency generation (SFG) vibrational spectroscopy at buried interfaces


Copyright (2006)


by


Sasha Joseph Kweskin

Abstract

Nanoscale chemical and mechanical characterization of molecules at

material interfaces: Sum frequency generation (SFG) surface vibrational

spectroscopy

by

Sasha Joseph Kweskin

Doctor of Philosophy in Chemistry

University of California, Berkeley

Professor Gabor A. Somorjai (Chair)

Sum frequency generation (SFG) surface vibrational spectroscopy was used to characterize interfaces pertinent to current surface engineering applications, such as thin film polymers and novel catalysts. An array of advanced surface science techniques like scanning probe microscopy (SPM), x-ray photoelectron spectroscopy (XPS), gas chromatography (GC) and electron microscopy were used to obtain experimental measurements complementary to SFG data elucidating polymer and catalyst surface composition, surface structure, and surface mechanical behavior. Experiments reported in this dissertation concentrate on three fundamental questions: (1) How does the interfacial molecular structure differ from that of the bulk in real world applications? (2) How do differences in chemical environment affect interface composition or conformation? (3) How do these changes correlate to properties such as mechanical or catalytic performance?

1

The density, surface energy and bonding at a solid interface dramatically alter the polymer configuration, physics and mechanical properties such as surface glass transition, adhesion and hardness. The enhanced sensitivity of SFG at the buried interface is applied to three systems: a series of acrylates under compression, the compositions and segregation behavior of binary polymer polyolefin blends, and the changes in surface structure of a hydrogel as a function of hydration. In addition, a catalytically active thin film of polymer coated nanoparticles is investigated to evaluate the efficacy of SFG to provide in situ information for catalytic reactions involving small mass adsorption and/or product development.

Through the use of SFG, in situ total internal reflection (TIR) was used to increase the sensitivity of SFG and provide the necessary specificity to investigate interfaces of thin polymer films and nanostructures previously considered unfeasible. The dynamic nature of thin film surfaces is examined and it is found that the non-equilibrium states contribute to practical applications of acrylates, blends and hydrogels. Lastly, nanoparticle surfaces and the catalytic activity and selectivity of platinum cube nanoparticles are correlated to the surface intermediates in a high pressure flow reactor.

# Table of Contents

## Acknowledgements

# Introduction

The density, surface energy and bonding of a contacting medium dramatically alter the polymer surface configuration in air. Molecular restructuring of a series of acrylates was investigated. Side branch ordering and the effect of glass transition temperature were shown to influence interfacial reconstruction. Total internal reflection (TIR) geometry was implemented to enhance the sensitivity at the interface of interest (polymer/solid) under the application of pressure. C-H vibrational resonances were probed optically to nondestructively examine the buried polymer/sapphire interfaces and obtain information about the molecular orientation in situ. These findings are contrasted with those of the same polymers cast from a toluene solution directly on the sapphire prism surface and annealed. Compared to polymer surface conformation in air, the SFG spectra of the deformed (compressed) PBMA at the sapphire interface illustrate that the ester butyl side-chain restructures and tilts away from the surface normal. However, the molecular conformation in the similarly deformed PMMA at the sapphire interface is identical to that obtained in air, which is dominated by the upright oriented ester methyl

side chains. For PBMA and PMMA spin cast on sapphire and annealed, the surface structure of the undeformed PBMA at the sapphire interface is identical to that of the deformed PBMA at the sapphire interface, while the PMMA conformation is different and shows $\alpha$-methyl group ordering. Since the glass transition temperature of PBMA is below room temperature, the rubbery state of PBMA demonstrates a melt-like behavior, evidenced by the fact that PBMA is in conformation chemical equilibrium at the sapphire surface even under compression. Due to the high glass transition temperature of PMMA, compression freezes PMMA in a metastable state, revealed by the restructured molecular conformation when annealed against the sapphire surface.

The surface compositions and segregation behavior of binary polymer polyolefin blends were characterized at hydrophilic solid sapphire and air interfaces. SFG spectra were collected from a bulk miscible blend consisting of identical molecular weight (~54000) and similar surface free energy (29-35 dyne/cm) components of atactic polypropylene (*a*PP) and aspecific poly(ethylene-co-propylene) rubber (*a*EPR). Characteristic CH resonances of the blend were contrasted with those of the individual components at both buried (sapphire/polymer) and free (air/polymer) interfaces. Preferential segregation of the *a*PP component was observed after annealing at both air/polymer and sapphire/polymer interfaces. SFG spectra revealed ordering of the polymer backbone segments with the methylene ($CH_2$) groups perpendicular to the surface at the sapphire interface and the methyl ($CH_3$) groups upright at the air interface. The SFG results indicate that the surface composition can be determined from the peak intensities that are characteristic of each component and that conformational entropy played a likely role in surface segregation. *a*PP occupied a smaller free volume at the

surface because of a statistically smaller segment length (*a*PP is more flexible and has a shorter length). In addition, the high density of the ordered $CH_3$ side branches enhanced the surface activity by allowing the long-chain backbone segments of *a*PP to order at the surface.

Changes in surface structure of a hydrogel were characterized as a function of hydration by various liquids. Molecular restructuring at the free surface of poly(2-hydroxyethyl methacrylate) (PHEMA) films and buried interface with a sapphire substrate due to submersion in deuterated water ($D_2O$) and acetonitrile ($d_3ACN$) was investigated by infrared-visible sum frequency generation vibrational spectroscopy. Film hydration by saturation with water and acetonitrile resulted in polymer swelling. Because of the amphiphilic nature of PHEMA, direct information about polymer restructuring was obtained due to the existence of hydrophilic and hydrophobic moieties. SFG results provided insight into the restructuring behavior at the PHEMA surface upon swelling due to the diffusion of the two different liquids. Identical polymer surface conformations were observed at the hydrophilic sapphire/polymer and $D_2O$/polymer interfaces, while the amphiphilic $d_3ACN$ solvent resulted in ordering of the hydrophobic polymer groups. The solid interface influenced polymer conformation upon hydration by the amphiphilic $d_3ACN$ altogether differently from the restructuring at the free surface. In addition, the properties of the plasticizer (i.e., surface tension, dipole moment, and hydrogen bonding) strongly affected which groups restructured upon contact as well as the extent of the conformational changes.

Quantitative results were obtained elucidating the dynamic nature of moisture at an interface and its correlation to bulk hydration. Upon hydration by saturating the films

with deuterated water ($D_2O$~73.1dyn/cm), poly(2-hydoxyethyl methacrylate) (PHEMA) and poly(2-hydroxypropyl methacrylate) (PHPMA) swell as the liquid penetrates the film. The hydrogel's hydrophobic and hydrophilic moieties compete for van der Waals and hydrogen bonding interactions between neighboring chains and water. The nature of water sorption in the bulk affects the water intensity measured at the solid/polymer interface. Increasing the hydrophobicity of the hydrogel film not only decreases bulk water content, but also water signal at an oxide interface. In contrast, urea increases the water content of the bulk film by disturbing chain interactions and correspondingly intensifies the water signal at the solid/polymer interface. Finally, the dynamics of drying are investigated demonstrating the sensitivity of SFG for solid/solid interface edge studies otherwise difficult to obtain.

Subsequently, a method was developed, using SFG, to probe the surface species present under reaction conditions on a catalytically active nanoparticle. Coherent SFG is collected from metal cubes smaller than ever investigated before (~7nm). The adsorption and oxidation of CO on monolayer films of cubic Pt nanoparticles synthesized by a modified solution phase polyol process were examined. Poly(vinylpyrrolidone)-capped Pt nanoparticles deposited on single-crystal sapphire were monitored under high-pressure reaction conditions in a spectroscopy-catalytic reactor cell. Extremely low incident laser power (i.e., ~5 μJ of infrared) yields sufficient SFG intensity in TIR geometry and reduces destructive interference. Because internal reflection does not require a correction for bulk gas absorption, CO spectra can be obtained over a wide pressure range (i.e., from <1 mtorr up to 700 torr). The effect of the capping polymer on the position and intensity of the CO peak was studied before and after low-temperature calcination. The polymer

decreased the CO adsorption and caused a slight red-shift of the atop CO band relative to a surface treated in oxygen at 373 K. The mass of the adsorbed CO (measured with a quartz crystal microbalance) was used to determine the surface coverage by CO. Oxidation rates were determined by measuring the intensity of the atop CO peak as a function of time in the presence of flowing oxygen. The activation energy (~19.8 kcal/mol) determined from the SFG data is close to that obtained from gas chromatography measurements of CO oxidation rates at different temperatures. The SFG and chromatography results are in good agreement with published data for Pt(100) surfaces.

Finally, SFG is employed to characterize the nanoparticles during oxidation/reduction cycles and in the presence of ethylene. A monolayer of coloidal 7.1 nm {100} platinum cubes is investigated on an alumina single crystal support. Spectra are measured of poly(vinylpyrrolidone) capped nanoparticles before and after cleaning by cyclic oxidation/reduction. Adsorption of carbon monoxide is utilized as a probe of local platinum surface structure. In the presence of CO, the capping agent restructures and a large atop CO peak is measured. Once oxidation/reduction exposes active sites, the nanoparticles are subsequently exposed to an atmosphere of ethylene. The SFG spectrum corresponds well with published data for a {100} platinum single crystal. In total internal reflection geometry, the sensitivity is increased with extremely low incident laser power, and the effect of destructive interference from opposite sides of the particle is minimized. The spectra require no bulk gas absorption correction and scattering losses are minor.

In conclusion, the increase in the sensitivity of SFG due to TIR geometry provides the necessary specificity to investigate interfaces of thin polymer films and

nanostructures previously considered and determined unfeasible. The dynamic nature of thin film surfaces are examined because the non-equilibrium states contribute to practical applications of acrylates, blends and hydrogels. Lastly, TIR increases the signal from nanoparticle surfaces, and the catalytic activity and selectivity of a platinum cubes are correlated to the surface intermediates in a high pressure flow reactor.

# Chapter 1

# Application of sum frequency generation (SFG) vibrational spectroscopy

## 1.1 Introduction to SFG surface vibrational spectroscopy

One of the main challenges in surface chemistry has been to develop characterization methods that enable in situ monitoring of surfaces under realistic conditions. Recently, infrared visible sum frequency generation (SFG) spectroscopy has emerged as the most surface specific technique for analyzing interface chemical conformation. Traditional vacuum surface techniques like low-energy electron diffraction (LEED), Auger electron spectroscopy (AES), high-resolution electron energy loss spectroscopy (HREELS), near edge x-ray absorption fine structure (NEXAFS), and x-ray photoemission spectroscopy (XPS) use electrons to determine surface structures, chemical compositions, bonding geometries, surface molecular vibrations, and oxidation states.[1,2,3,4,5] Whereas vacuum techniques often utilize the large mean free path required for probe electrons to reach the sample or detector, SFG is a photon-in photon-out spectroscopy that can operate at high pressures, solid/liquid, or solid/solid interfaces, only limited by the attenuation of the light.

In SFG vibrational spectroscopy, a tuned infrared (IR) beam of frequency $\omega_{ir}$ is overlapped with a visible beam of frequency $\omega_{vis}$ in a second-order nonlinear optical process. These two input beams are spatially and temporally superimposed to produce an output beam of sum frequency $\omega_{sfg} = \omega_{ir} + \omega_{vis}$, which satisfies momentum and energy conservation. The process essentially consists of simultaneous infrared absorption by a vibrational mode coupled with upconversion via a Raman process.[6] Therefore, for a mode to be SFG active, it must obey both IR and Raman selection rules. Since no mode that possesses inversion symmetry can be infrared and Raman allowed (e.g. benzene has no common modes), signal is primarily generated from interfaces and surfaces where centrosymmetry is broken.

SFG is a three-wave mixing process, and theoretical details beyond those presented here can be found in publications by Shen[7,8,9,10] and Hirose.[11] Under weak electric fields, the polarization $\vec{P}$ expansion has two terms governed by Eq. 1-1, where $\vec{P}^{(0)}$ is the static polarization, $\vec{P}^{(1)}$ is the first-order linear polarization, $\varepsilon_0$ is the permittivity of free space, $\tilde{\chi}^{(1)}$ is the linear susceptibility and $\vec{E}$ describes the electric field.

$$\vec{P} \approx \vec{P}^{(0)} + \vec{P}^{(1)} = \vec{P}^{(0)} + \varepsilon_0 \tilde{\chi}^{(1)} \vec{E} \qquad (1\text{-}1)$$

This expansion is sufficient for linear polarization spectroscopies such as Raman spectroscopy. In the presence of more intense electric fields, higher order polarization terms are required in the expansion. The sum frequency polarization, $\vec{P}^{(2)}$, induced at the interface is given by Eq. 1-2, where $\tilde{\chi}^{(2)}$ is the second-order nonlinear susceptibility of the polymer and $\vec{E}(\omega_{ir})$ and $\vec{E}(\omega_{vis})$ are the two input fields at different frequencies. The

electric fields $\vec{E}$ of the visible and infrared beams induce a nonlinear polarization, $\vec{P}^{(2)}$, which is proportional to the nonlinear susceptibility $\vec{\chi}^{(2)}$, i.e.,

$$\vec{P}^{(2)}\left(\omega_{sfg}\right) = \vec{\chi}^{(2)}\left(\omega_{sfg}\right) : \vec{E}(\omega_{ir})\vec{E}(\omega_{vis}) \tag{1-2}$$

The intensity of the SFG signal $I_{sfg}$ is proportional to the square of the nonlinear susceptibility and modeled by a Lorentzian distribution

$$I_{sfg} \propto \left|\chi_{NR}^{(2)} + \chi_{R}^{(2)}\right|^2 = \left|\chi_{NR}^{(2)} + \sum_q \frac{\vec{A}_q}{\omega_{ir} - \omega_q + i\Gamma}\right|^2 \tag{1-3}$$

where $\chi_{NR}^{(2)}$, $\chi_{R}^{(2)}$, $\vec{A}_q$, $\omega_q$, and $\Gamma$ are parameters extracted from the fit that represent the non-resonant contribution, resonant contribution, oscillator strength, resonant frequency, and damping coefficient, respectively. The oscillator strength $A_q$ is related to the number density of contributing oscillators, orientation-averaged coordinate transformation, and product of the derivatives of the polarizability and dipole moments. The nonresonant contribution originates from the substrate and is typically invariant to the incident infrared frequencies. The phase of the nonresonant background dictates the level of interference with resonant terms. SFG spectra are fit using Eq. 1-3 and parameters corresponding to the frequency center of the mode, amplitude, width, and complex phase relative to the background. The surface nonlinear susceptibility contains a vibrational resonant contribution, $\vec{A}_q = n_s \langle \vec{a}_q \rangle_f$. The two quantities, $\vec{A}_q$ and $\vec{a}_q$, are related to each other by the number density of contributing oscillators, $n_s$, and the orientation averaged coordinate transformation. This term is written as the product of the number density of contributing molecular groups at the surface, $n_s$, and the orientation averaged nonlinear polarizability of those groups (brackets denote an average over a distribution function $f$).

The resonant term is enhanced when the infrared beam ($\square_{IR}$) is tuned near a vibrational mode, $q$, belonging to one of the molecular groups at the interface ($\square_q$). The gross infrared and Raman selection rules are imposed on the equation $a_{q,lmn} \propto \left( \dfrac{\partial \alpha_{lm}}{\partial Q_q} \right) \left( \dfrac{\partial \mu_n}{\partial Q_q} \right)$ where $\mu_n$ is the dipole moment and $\alpha_{lm}$ is the polarizability. $a_{q,lmn}$ is proportional to the derivatives of the dipole moment and polarizability with respect to the vibration coordinate $Q_q$. Therefore similar to liner vibrational spectroscopies, a change in dipole moment and first order polarizability is at the core of SFG.

Within the dipole approximation (e.g. excluding quadropolar interactions), each of the 27 elements of a third rank tensor $\tilde{\chi}^{(2)}$ vanishes in materials that possess inversion symmetry. This can be understood because in a centrosymmetric medium, $\tilde{\chi}^{(2)}$ must be invariant under inversion; however the electric field and polarization vectors must change signs. Therefore, the inversion operator implies $\tilde{\chi}^{(2)} = -\tilde{\chi}^{(2)}$ or $\tilde{\chi}^{(2)} = 0$. Elements of $\tilde{\chi}^{(2)}$ can be nonzero in molecules that lack inversion symmetry. Often, a material that is randomly oriented in the bulk will assume a preferred orientation at an interface in order to reduce the surface energy, leading to broken symmetry in the surface plane. Thus, measurement of $\tilde{\chi}^{(2)}$ can be specifically sensitive to polar ordering of molecular groups at interfaces. Additionally, since SFG spectroscopy probes an ensemble, the average value of $\tilde{\chi}^{(2)}$ is zero in randomly oriented SFG active materials. Since it is experimentally unfeasible to apply SFG to single molecules, this will be discussed further in regards to orientational analysis of many contributing molecules.

The intensity of the generated SFG is proportional to the effective surface nonlinear susceptibility, $I(\omega_s) \propto \left| \chi_{eff}^{(2)} \right|^2$. $\chi_{eff}^{(2)}$ includes the unit polarization vector $\hat{e}_s$ and Fresnel factors $\vec{L}(\omega)$, which are dependent on the refractive indices of the two media forming the interface. In quantitatively comparing SFG signals generated from different types of interfaces (polymer/air vs. polymer/solid) or SFG signals that were collected using different polarization combinations of light, it is necessary to account for these differences:

$$\chi_{eff}^{(2)} = \left[ \hat{e}_s \cdot \vec{L}(\omega_s) \right] \tilde{\chi}^{(2)} : \left[ \hat{e}_1 \cdot \vec{L}(\omega_1) \right] \left[ \hat{e}_2 \cdot \vec{L}(\omega_2) \right]$$

These important factors will be discussed in further detail in chapter 2.

Various polarization combinations (of incident and collected SF photons) probe different elements of the surface nonlinear susceptibility. If there are SFG active groups at an interface that are azimuthally ordered and if the molecular groups are isotropic in the surface $x$-$y$ plane ($x=y=-x=-y$), then there are four unique elements of the surface nonlinear susceptibility tensor: $\chi_{yyz}$, $\chi_{yzy}$, $\chi_{zyy}$, and $\chi_{zzz}$. In our experiments, we have primarily used the $s_{sum}s_{vis}p_{IR}$, $p_{sum}p_{vis}p_{IR}$ and $s_{sum}p_{vis}s_{IR}$. Fig. 1-1 demonstrates incident polarizations $s$ and $p$, where $p$ refers to parallel polarized radiation and $s$ to perpendicular polarized radiation with respect to the plane of incidence determined by the line of incident laser direction and the laboratory z-axis.
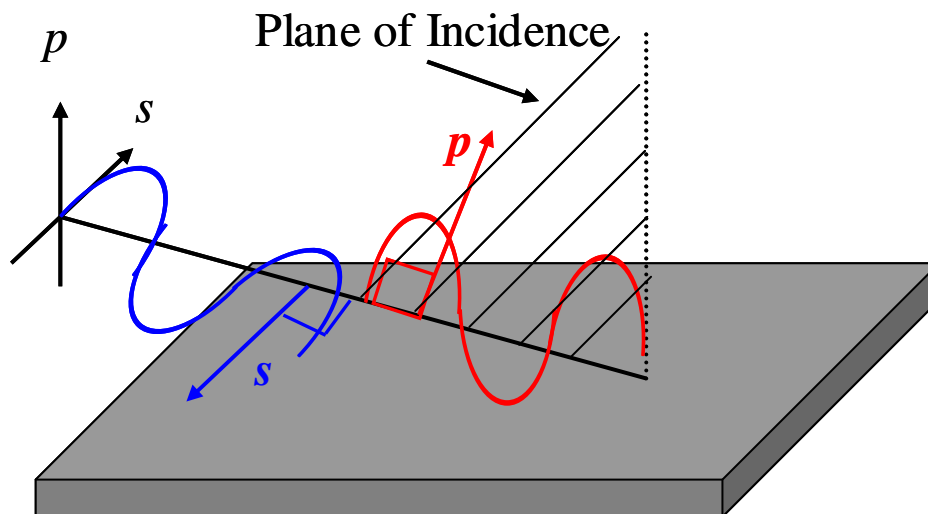
**Figure 1-1:** Schematic representation of *s* and *p* polarized radiation.

Primarily, spectra were obtained in $s_{sum}s_{vis}p_{IR}$ polarization combination, which imparts the greatest signal-to-noise ratio and is sensitive to $\chi_{yyz}$ element of the nonlinear susceptibility tensor. This polarization combination is most sensitive to vibrations that have a component of the vibrational dipole $(\mu_n)$ along the surface normal, *z*, and a component of the polarizability tensor $(\alpha_{lm})$ in the surface plane *(x-y)*. Spectra were also collected using the $p_{sum}p_{vis}p_{IR}$ and $s_{sum}p_{vis}s_{IR}$ polarization combinations, which are sensitive to $A_{zzz}$, $A_{yyz}$, and $A_{yzy}$. If the derived (experimentally or theoretically) components of $\vec{a}_q$ for a vibrational resonance are known (e.g. bond polarizability), then the fitted vibrational mode strengths, $\vec{A}_q$, can be used to determine changes in number density and/or orientation of the molecular group giving rise to the vibration. The decoupling of orientation from number density is extremely difficult because only contributing groups are factored into calculations. Aside from the experimental difficulties in instrument execution of orientational studies, the ability of SFG for accurate spectral assignment and

polarization analysis is still in its early stages. Recently, the use of Raman and IR spectroscopic assignments applied to SFG has been disputed.[12] The deconvolution of peaks is often times difficult, and the environments of the chemical groups under investigation are in unique surrounding. Additionally, a serious problem has been exposed by Wang et al.[12] because the accumulation of experimental data and theoretical calculations on Raman depolarization ratios and bond polarizability tensors was oversimplified in previous analyses. The following examples illustrate the basic methodology that can be used for quantitative investigations. Although more complicated than initially anticipated, the following demonstrations explore the dependence of SFG signal in an idealized model where complete assignment in a unique uncoupled environment, and the bond polarizability are known exactly.

For example, a single C-H vibration is explored. The vibrational dipole change is along the bond axis (the C-H) and the polarizability derivative is strongest in the plane perpendicular to this axis. Therefore, the largest component of the nonlinear polarizability tensor will be $a_{ccc}$. Molecular $(a,b,c)$ coordinate systems used in describing the CH, $CH_2$ and $CH_3$ groups. The relationship between the molecular and lab fixed $(x,y,z)$ coordinate systems is shown in Fig. 1-2. Coordinate transformations from the molecular frame to the laboratory frame involve a standard three Euler angles $\chi$, $\theta$, and $\phi$ transformation. The angle $\chi$ is a rotation about the lab fixed z-axis. For an x-y isotropic surface containing a collection of C-H groups, this angle is integrated over its full range of values. The angle $\theta$ (referred to here as tilt angle) related the z-axis to the molecule frame c-axis. The final rotation, $\phi$, is about the new z-axis (c-axis). The dependence of the SFG signal intensity as a function of orientation due to an ensemble of molecular

7

moieties measured by *ssp* SFG spectra is given by the relationship,

$$A_{yyz} = \langle (\hat{y} \cdot \hat{c})(\hat{y} \cdot \hat{c})(\hat{z} \cdot \hat{c}) \rangle a_{ccc} .$$
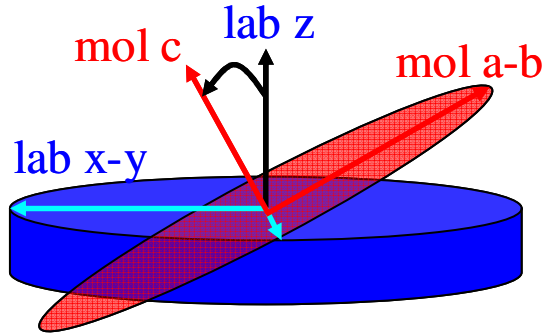


**Figure 1-2:** The relationship between the molecular (a,b,c) and lab fixed (*x,y,z*) coordinate systems. Coordinate transformations from the molecular frame to the laboratory frame involve a standard three Euler angles $\chi$, $\theta$, and $\phi$ transformation.

A plot of the SFG amplitude dependence vs. azimuthal tilt angle is shown in Fig. 1-3. As the tilt angle, $\theta$, between the laboratory fixed frame of reference and the molecular axis of the bond reorients, the measured SFG intensity would dramatically vary. The coordinate transformation can be understood qualitatively because if the azimuthal tilt is zero (molecule is upright), then $(\hat{y} \cdot \hat{c})$ will be zero and no SFG signal will be measured. If the bond is perpendicular to the z-axis (lying in the plane of the surface), then $(\hat{z} \cdot \hat{c})$ will vanish, and correspondingly so will the SFG. Therefore normal ordering is not the only prerequisite for SFG signal. In plane and normal to the x-y plane alignment of bonds produces no signal at an interface. However, for a single molecule

heteroatom vibration, tilting with respect to the surface normal produces SFG intensity. The system becomes more complicated for many atom systems.
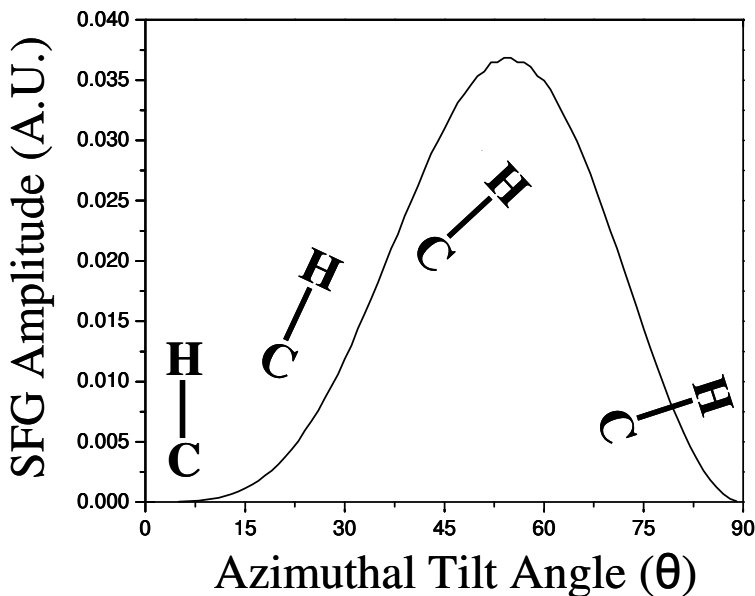


**Figure 1-3:** Calculated orientation dependence of the ssp SFG amplitude, $A_{yyz}$, for a C-H vibration.

Hirose's bond additivity model[11] extends the previous calculations to a slightly more complicated molecule such as a $CH_2$. Shen[6] gives the nonzero components of $\vec{a}_q$ for the $CH_2$(s) ($a_{aac}$, $a_{bbc}$, $a_{ccc}$) and $CH_2$(a) ($a_{aca}$ and $a_{caa}$) vibration, and can be estimated for any C-H vibration using the C-H bond additivity model. The SFG amplitude strength $A_{yyz}$ depends on the azimuthal tilt angle, $\theta$, for the $CH_2$(s) and $CH_2$(a) stretches. As previously stated, SFG is sensitive to the orientation of an ensemble. Therefore, this calculation includes a distribution function usually assumed in the orientation averaged nonlinear polarizability of the $CH_2$ a distribution function. Considering only the dipole moment change, the bond additivity model can be understood by adding the vectors due to the

9

vibrational mode. Fig. 1-4 demonstrates the addition of $CH_2(s)$ and $CH_2(a)$ vibrations. Notice that the vector sum is parallel to the $C_2$ rotation axis for symmetric and perpendicular for asymmetric modes. In the *ssp* spectra, where the ir (dipole moment) is perpendicular to the laboratory x-y plane, the $CH_2(s)$ vibration will be largest if the vector sum is oriented along the surface normal. In *sps* spectra, where the IR (dipole moment) is mainly in the laboratory x-y plane, the $CH_2(a)$ vibration will be largest if the molecular group is upright.
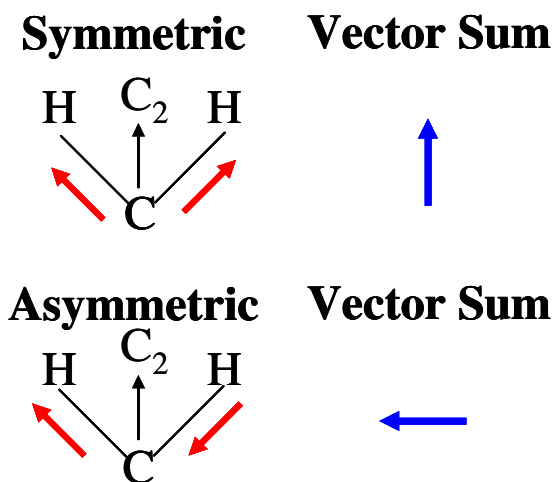
**Figure 1-4:** Application of the bond additivity model to the ideal $CH_2(s)$ and $CH_2(a)$.

Calculated ssp SFG spectra generated from a surface made up of an x-y isotropic collection of $CH_2$ groups are presented in Fig. 1-5. These plots compare SFG spectra expected to be measured from a collection of $CH_2$ groups at an interface that have tilt angle orientation distributions centered at 0°, 30°, 60°, and 90° and Gaussian distribution widths of 2°(narrow), 40°(wide), and 70°(very wide). From Fig. 1-5, large ssp SFG signal intensities are expected from interfaces where the $CH_2$ groups are upright oriented with a

narrow distribution of orientations. Smaller signal intensities are expected from more randomly oriented interfaces.
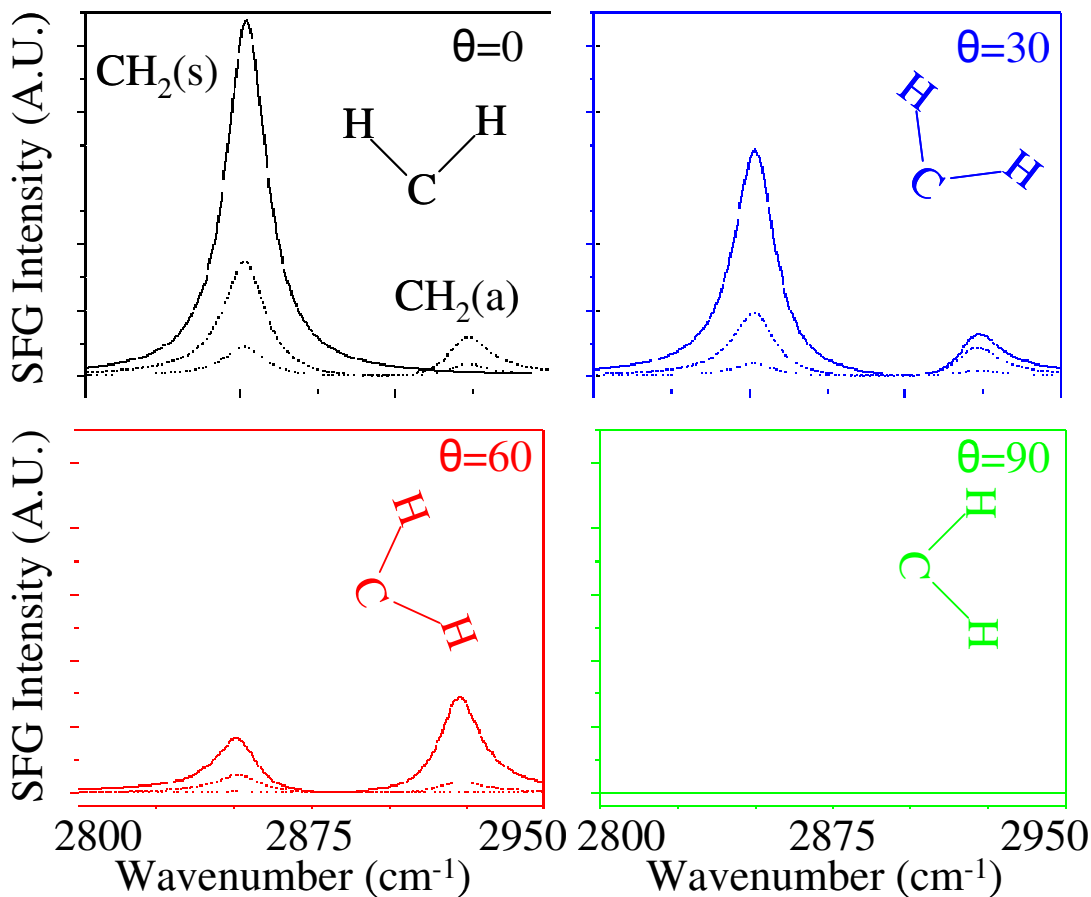


**Figure 1-5:** Calculated SFG spectra demonstrating the $CH_2(s)$ and $CH_2(a)$ vibrations signal intensity variation with tilt ($\theta$) and distribution. Solid lines denote a narrow orientation distribution ($\Delta\theta=2°$, Gaussian), dashed lines denote a normal orientation distribution ($\Delta\theta=40°$, Gaussian) of dotted lines denote a broad orientation distribution ($\Delta\theta=70°$, Gaussian). ($\phi_c=0°$, $\Delta\phi=5°$)

For a fixed number density, from the ratio of the vibrational mode amplitudes, fit spectral parameters can be used to infer orientation of molecules at an interface.

11

Additionally, Figure 1-5 shows that the ratio between the $CH_2(s)$ and $CH_2(a)$ peaks decreases as the distribution width increases. SFG spectra obtained from a surface where the species have a small $\theta_c$ and large $\Delta\theta$ may be quantitatively identical to spectra obtained from surfaces where the species have a larger $\theta_c$ but smaller $\Delta\theta$. In most cases, it is impossible to distinguish these two cases, especially after considering additional variables such as surface roughness, chemical environment, mode assignment and number density. It is usually not possible to describe orientation and concentration of molecular groups at an interface from SFG data. Albeit, sometimes the SFG spectra can be used to infer the general orientation of molecules at an interface, and quantitatively compare number density relative to other spectra.

## 1.2 SFG experimental setup

SFG spectra were obtained using a mode-locked Nd:YAG laser (Leopard, Continuum, Santa Clara, CA). The 1064-nm light generated by this laser has a pulse width of 21 ps at a repetition rate of 20 Hz. The sum frequency generation (SFG) vibrational spectroscopy studies undertaken as part of this work were performed using a custom LaserVision KTP ($KTiOPO_4$) optical parametric generation and amplification (OPG/OPA) system driven by the fundamental output of the commercial Nd:YAG laser. The energy per pulse of the 1064 nm maximum fundamental beam was between 30 and 35 mJ.

The OPG/OPA system uses three distinct nonlinear crystal stages to generate the beams necessary for SFG experiments. A frequency doubling stage coverts the 1064nm photons to 532 nm laser beam. The second OPG/OPA stage generates a beam tunable

from 710 to 860 nm, and a difference frequency mixing (DFM) stage generates the tunable mid-infrared beam used in our experiments. These three main stages are shown in Fig. 1-6. A fourth nonlinear crystal stage (AgGaSe$_2$ or AgGaS$_2$) can be used to generate a beam that is tunable from 1000 to 2000 cm$^{-1}$ and pulse of FWHM = 7 cm$^{-1}$.
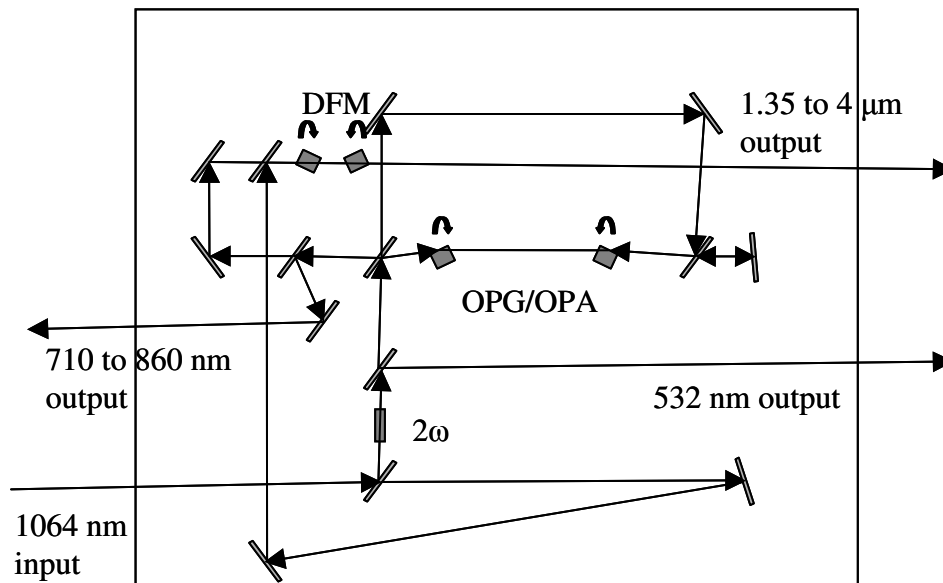


**Figure 1-6:** Schematic of LaserVision OPG/OPA system.

Once the infrared and green laser beams exit the LaserVision box, they are directed, through a series of optics, to the sample, Fig. 1-7. The laser beam polarization and delay are controlled during the SFG experiments. The beams are temporally and spatially overlapped on the surface striking the surface at a variable angle. The sum-frequency signal was measured in the reflected direction. The sum frequency beam generated during SFG experiments is sent through a monochrometer and green notch filter to eliminate scattered light. A photomultiplier tube (Hamamatsu) is used to detect the signal intensity and a gated integrator (Stanford Research) is used to improve our signal to noise ratio during SFG experiments.
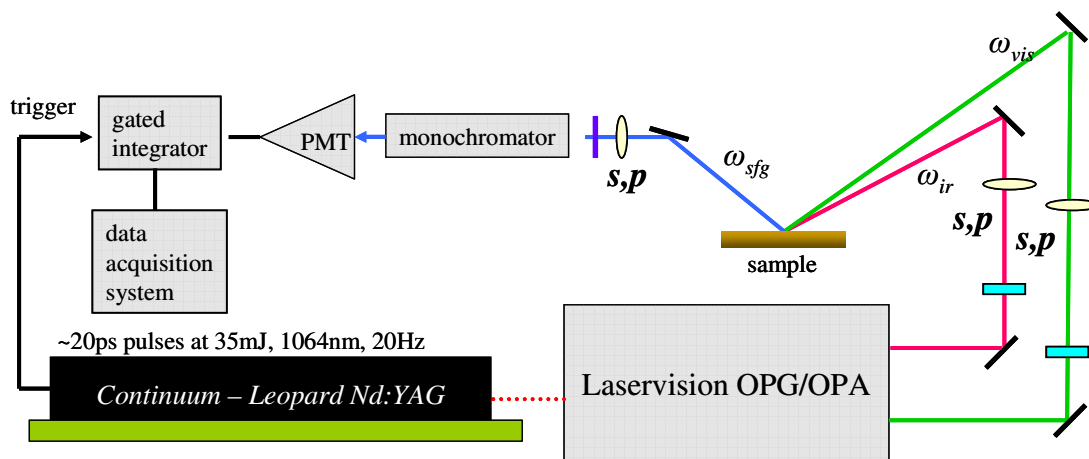
**Figure 1-7:** Schematic setup of laser system, sample, and data acquisition.

## 1.3 Examples of SFG spectra

SFG spectra (*ssp* polarization combination) obtained from methanol and acetonitrile surfaces at room temperature are shown in Fig. 1-8. Peak assignments were made according to previously published data.[13,14] The SFG spectrum of methanol/air interface shows two primary peaks located at 2850 and 2965cm$^{-1}$. These are assigned to the symmetric and asymmetric $CH_3$ stretches. In addition, there is a shoulder around 2920cm$^{-1}$ that is due to the Fermi resonance of the $CH_3$(s) stretch and an overtone of a $CH_3$ bending mode. The SFG spectrum of the acetonitrile/air interface contains one peak at 2940cm$^{-1}$ that is due to the symmetric stretching mode $CH_3$. The large SFG signal implies that the surface has well-ordered methyl groups. Since the symmetric stretches are much greater than asymmetric modes, the spectra imply that the molecules are more or less oriented with the $C_3$ axis normal to the plane of the liquid surface. This agrees with predictions hydrophobic groups orient outward into air. This lowers the overall surface energy. [15]
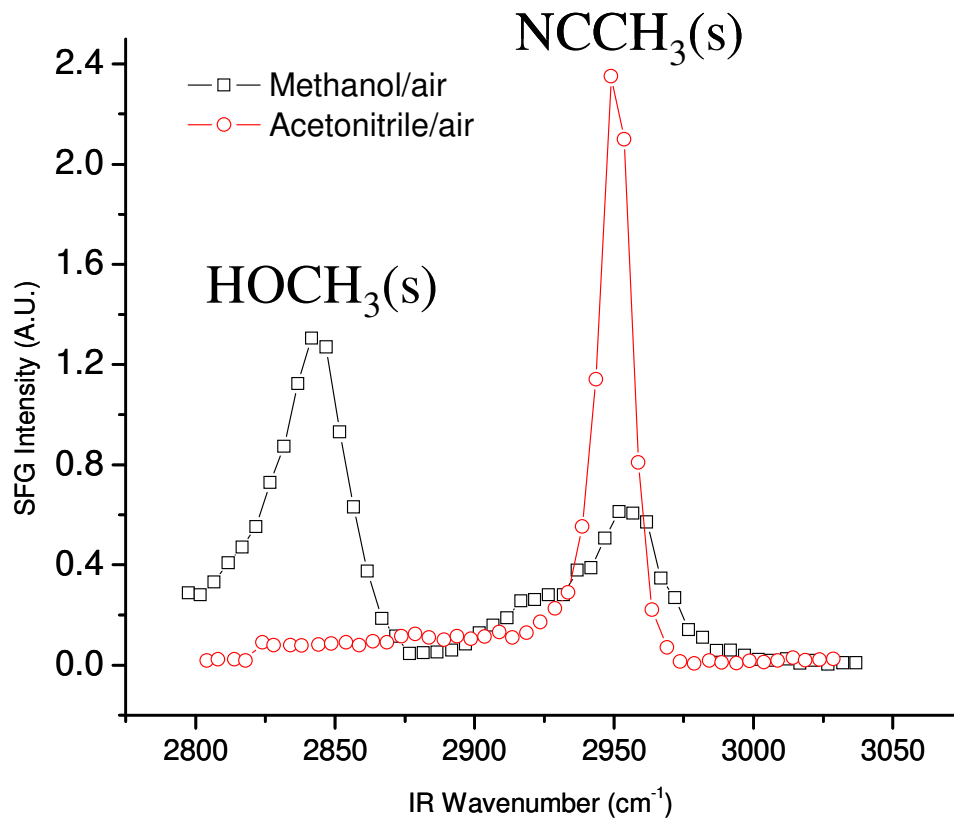
**Figure 1-8:** SFG spectra of (a) neat methanol/air (□)and (b) neat acetonitrile/air (○) interfaces. Both spectra were generated using the *ssp* polarization combination

SFG collected from polymer/air interfaces collected in *ssp* polarization are shown in Fig. 1-9. The spectra show how the atactic polypropylene (aPP) and atactic polybutylene orient their hydrophobic bulky side chains outward in an analogous way to the liquids. Low surface energy side branches have a significant effect on SFG spectra measured at the polymer/air interface. Polymer side chains have an additional driving force for this surface structure. Loops of the polymer chain often lie flat against the surface and the side chains sterically bump against each other and induce ordering. The SFG spectra of the *a*PP and *a*PB films show a feature at ~2880cm$^{-1}$ that is assigned to the

$CH_3(s)$ stretch from the side branch. The features at ~2960 and ~2945cm$^{-1}$ are assigned to the $CH_3$ antisymmetric ($CH_3$(a)) stretch and Fermi resonance with a bending mode from the methyl side branch. Peaks at ~2850cm$^{-1}$ and ~2920cm$^{-1}$ are assigned as the $CH_2$ symmetric ($CH_2$(s)) and antisymmetric ($CH_2$(a)) stretches, respectively. [16] The SFG spectrum of *a*PB has qualitatively similar features to the spectra of *a*PP. In comparing the spectra in Fig. 1-8, notice the difference in the ratio of the $CH_3$(s)/$CH_3$(a) stretch. For *a*PB, this ratio is smaller than it is for *a*PP, indicating that the *a*PB methyl groups at the surface may be more tilted than the *a*PP methyl groups – consistent with the extra degree of freedom afforded by the longer side branch.
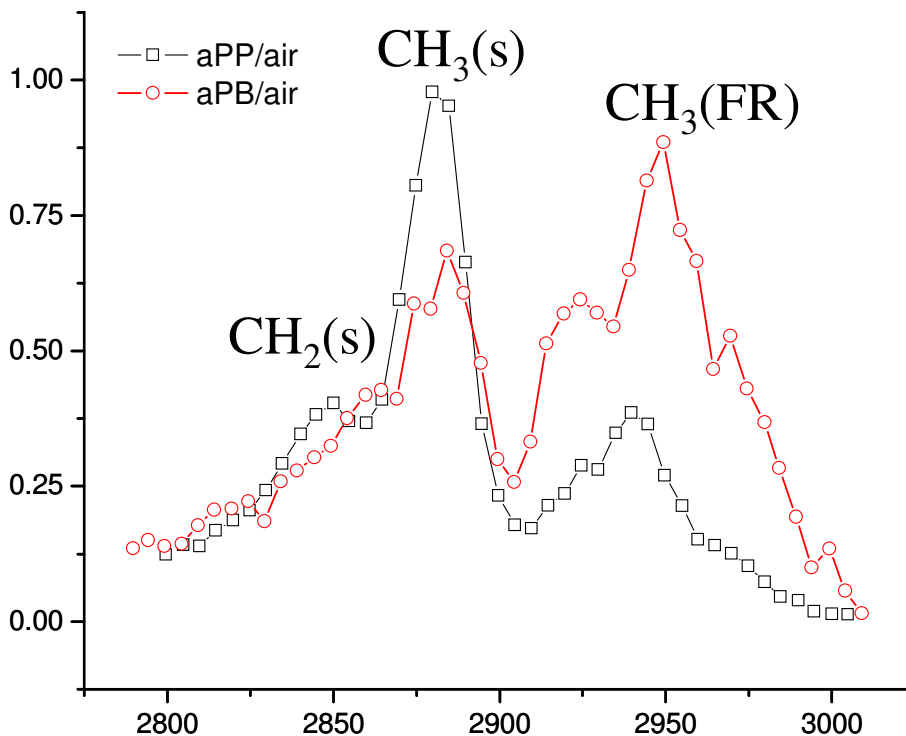


**Figure 1-9:** SFG spectra of (a) aPP/air (□)and (b) aPB/air (○) interfaces. Both spectra were generated using the *ssp* polarization combination

The previous examples show that bulky low surface energy side branches tend to order at the air interface. In contrast, if the polymer has a hydrophilic side branch instead of a hydrophobic branch, then the low surface tension component will tend to order at the air interface.[17] In general, the bulky, low surface tension branch is upright oriented at the interface. The following chapters discuss the effects of surface energy and density on the molecular rearrangement of the polymer surface.

## 1.4 Scanning probe microscopy (SPM) and X-ray photoelectron spectroscopy (XPS)

SPM and SFG can provide surface details that complement each other. Various problems in polymer surface science have been studied by this combination. Strong correlations were obtained between surface structure, chemistry and mechanical properties of polymers.[18] This indicates that a number of surface properties are rooted in molecular level behavior. The preceding SFG examples show that SFG is very sensitive to the orientation and density of molecular groups at an interface, and therefore gives insight into the general structure of the surface. When data from SFG spectra can be analyzed alongside data obtained from other surface sensitive techniques, such as nanometer-scale indentations and friction studies, interpretations of the overall polymer surface behavior are more lucrative. Atomic force microscopy (AFM) is a member of the family of scanned probe techniques, and was initially demonstrated in the mid 1980's.[19] A Hysitron Triboindentor is another SPM that differs from AFM in its feedback loop.

Instead of deflection of a cantilever detected by a laser diode position, the triboindenter measures force and position by means of capacitive transducers (Fig.1-10).
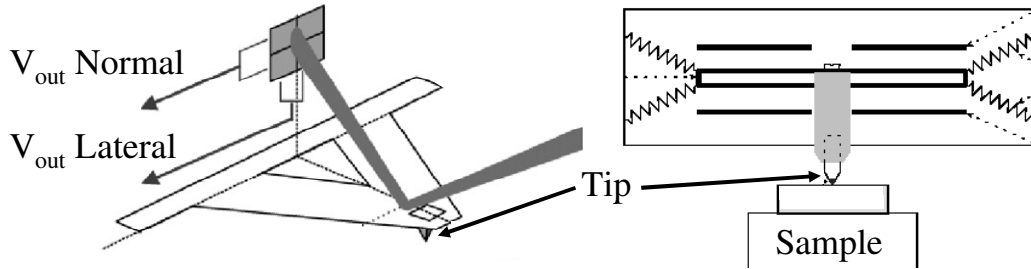


**Figure 1-10:** AFM experimental scematic (left) and triboscope experimental schematic (right).

AFM is used in these experiments to impart lateral resolution and measure surface roughness or film thickness. In some cases AFM and triboindentation is used to measure the surface mechanical behavior. Essentially, each instrument has a tip of a variety of materials and a range of sharpnesses. The sharpest tip mainly consisting of silicon based materials, radius of curvature <20 nm, is used exclusively for AFM experiments. Blunter tips fabricated from diamond, radius of curvature ~ 100 nm-20 μm, are the mainstay of the triboindentor. This tip is brought into contact with the surface of interest by a stepper motor or other micron-scale approach mechanism. Angstrom-scale manipulation of the tip/cantilever position is achieved through the use of piezoelectric actuators. As the tip interacts with the surface either attractively or repulsively, the cantilever bends or the springs suspending the capacitive element flex. The movement can be measured by

monitoring the position of light (generated by a diode laser) reflected off the topside of the cantilever (AFM) or electronically through a transducer (triboscope).

AFM topographic images are obtained by maintaining a constant feedback between the photodiode detector and piezoelectric actuator. The tip is rastered across the surface and a plot is created. In a similar fashion, a feedback loop maintains the displacement of the pressure transducer in the triboscope, and images of the surface can be produced using sharp tips (100 nm-1 μm). Polymers are soft materials, and even though the force exerted is usually on the orders of nanonewtons, the pressures exerted on the surface are usually in the gigapascal range due to the small contact area. Fig. 1-11 demonstrates images of a polyethylene film obtained after a series of indentations with an AFM (silicon nitride tip of nominal radius of curvature ~20 nm) and a series of lateral scratches with a triboscope (diamond tip of ~100 nm radius of curvature).
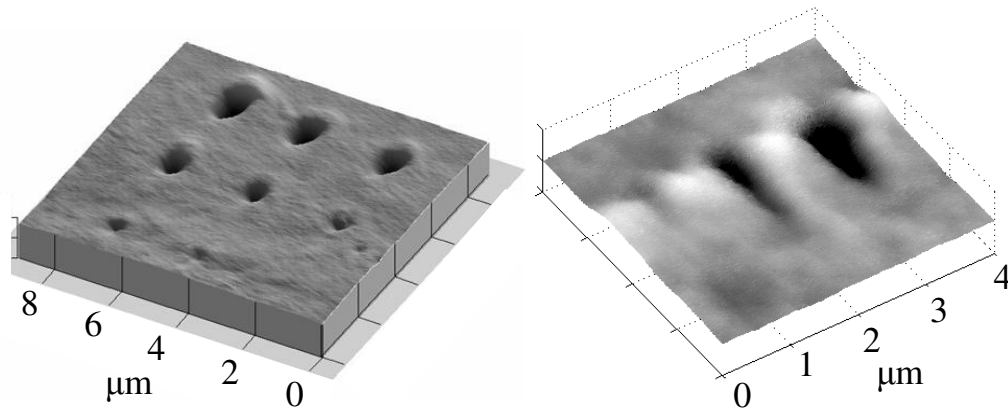


**Figure 1-11:** AFM (left) contact mode topography image and triboindentor contact mode image (right) polyethylene.

The indentations shown previously produce force/displacement curves that can be used to extract quantitative behavior of the surface mechanical behavior. The contact

19

mechanics of indentation are shown in Fig. 1-12, where $P_{max}$ is the maximum force, $R$ is the radius of curvature of the tip, $d$ is the indentation depth, and $h_c$ is the contact depth.[20] For AFM, as the tip approaches the surface, there is usually an attractive interaction between the tip and sample. After contact, the tip can be retracted from the surface. An adhesive interaction between the tip and the surface, leading to a maximum "pull-off force" that can be used to calculate the work of adhesion. The correlation between the loading and unloading paths indicates if the surface was deformed elastically or plastically. If there is no deformation of the surface, or if the surface was deformed elastically, the two paths overlap each other. If there is plastic deformation, a load hysteresis is produced due to separation of the loading and unloading paths. In both situations, Oliver and Phar[20] assert that the initial slope of the unloading curve represents the stiffness, and is assumed to be primarily dependent on the elastic behavior of the sample and the apparatus. Surface mechanical properties such as elastic modulus, hardness and friction can be measured with the SPM and compared to the bulk values.
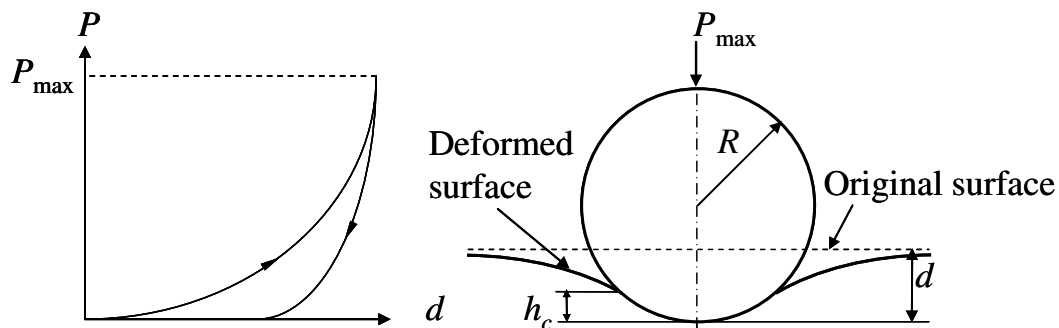


Fig

**Figure 1-12:** Illustration of important parameters extracted from nanoindentation

XPS experiments were performed on a Perkin-Elmer PHI 5300 XPS spectrometer with a position sensitive detector and a hemispherical electron energy analyzer. Typically

Mg Kα x-ray emission (1253.6eV) was used as the probe and was generated with 400 W (15 kV acceleration voltage) at the Mg cathode. An electron with a kinetic energy of ~1200 eV has an attenuation length of 2.9±0.4 nm measured by Roberts et al.[21] for photoelectrons ejected from PMMA. The photoemission process is illustrated in Fig. 1-13. Briefly, an incident x-ray photon ionizes a core electron and the ejected photoelectron energy is measured. This energy relates to the binding energy and characteristic peak intensities and shifts can be related to composition and chemical identity of the uppermost nanometers of a surface.
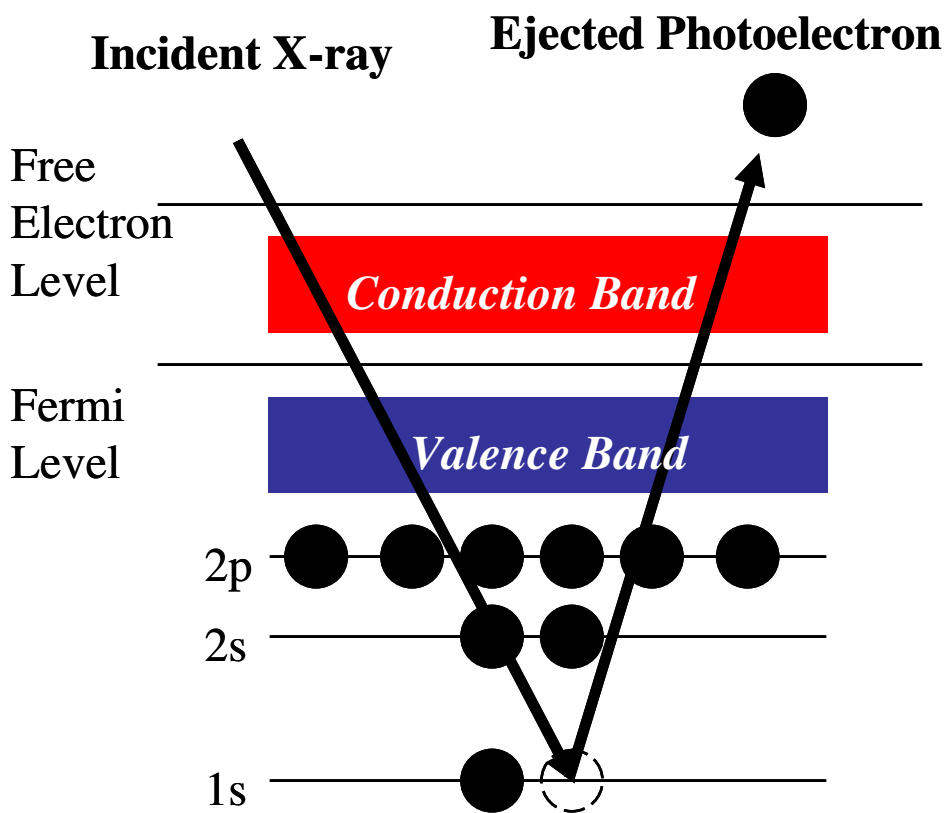


**Figure 1-13:** Schematic of the x-ray photoemission process.

## 1.5 Complementary use of SFG, XPS, and SPM

The surface chemistry and topography of polyethylene (PE) was characterized by a combination of complementary techniques after exposure to high energy argon plasma. XPS is extremely sensitive to the change in the surface of the polymer film upon treatment. Fig. 1-14 shows XPS survey spectra for untreated and Ar plasma treated PE films. O1s and C1s reveal the formation of oxygen containing functional groups at the polymer surface for high power treatments. Upon closer inspection, small shifts due to the formation of C-O, C=O, and O-C=O can be observed.
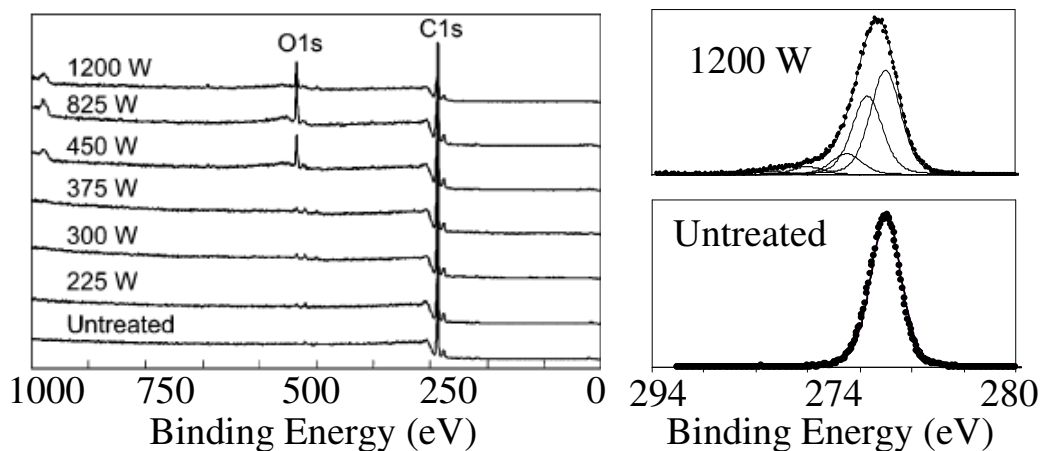


**Figure 1-14:** XPS spectra of polyethylene versus argon plasma treatment power (left). C 1s region demonstrating fit peaks (right).[22]

Since the formation of surface active species in complex, and the plasma treatment simultaneously modifies and roughens the surface, complementary techniques facilitate the understanding of this process. Since the recipe must be fine tuned for the desired application, topography and molecular structure of the surface is needed. Fig. 1-15 shows how the combination of AFM and SFG can advance the understanding of a surface treatment. AFM demonstrates an increase in roughness with the increase in

plasma power. SFG, sensitive to submonolayer molecular coverages, illustrates the formation of $CH_3$ moieties. Hence, a combination of techniques is useful to characterize the physical and chemical modification of films.
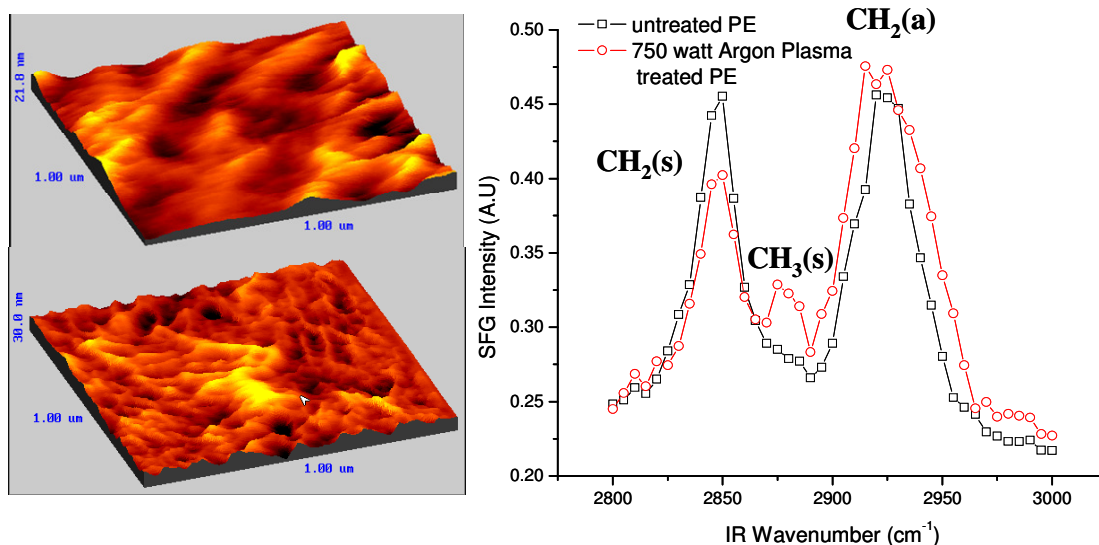


**Figure 1-15:** AFM images 1 μm X 1 μm of polyethylene before and after argon plasma treatment (left) and corresponding SFG spectra collected in *ssp* polarization combination before and after argon treatment.

## 1.6 Conclusion

This chapter introduced SFG surface vibrational spectroscopy at interfaces, SPM and its use in topographic and material characterization, and the complementary use of these techniques with XPS. The basic equations of SFG vibrational spectroscopy, relevant to understanding and interpreting SFG spectra, were presented. Illustrations of the unique properties of SFG were presented, demonstrating the sensitivity of SFG

spectra obtained from liquid/air and polymer/air interfaces to molecular ordering at the interface.

The subsequent chapters emphasize some of the unique information that can be extracted from SFG spectra collected mainly from solid/solid or solid/liquid interfaces. Additionally, SFG was used in catalytic studies of nanostructures. Of special interest are the cases where SFG data can be correlated to material properties such as glass transition temperature, radii of gyration of polymers, and reactivity of nanoparticles. Various materials such as acrylate/oxide, hydrogel/liquid, and platinum/gas are highlighted in terms of their performance in industrial applications.

## References

[1] G. A. Somorjai, *Introduction to Surface Chemistry and Catalysis*, John Wiley & Sons, Inc., New York, 1994.

[2] G. A. Somorjai, *Surf. Sci.* 1994, **299/300,** 849.

[3] D. W. Goodman, *Chem. Rev.* 1995, **95,** 523.

[4] Woodruff, D. P., and T. A. Delchar, *Modern Techniques of Surface Science*, Cambridge University Press, New York, 1986.

[5] G. Ertl, *Surf. Sci.*1994, **299/300,** 742.

[6] Shen, Y.R. Surf. Sci. 1994, 299, 551.

[7] Shen, Y.R., *Principles of Nonlinear Optics*, John Wiley & Sons, New York, 1984.

[8] Wei, X.; Hong, S.C.; Zhuang, X.W.; Goto, T.; Shen, Y.R. *Phys. Rev. E* **2000**, *62*, 5160.

[9] Miranda, P.B.; Shen, Y.R. *J. Phys. Chem. B* **1999**, *103*, 3292.

[10] Zhuang, X.; Miranda, P.B.; Kim, D.; Shen, Y.R. *Phys. Rev. B* **1999**, *59*, 12632.

[11] Hirose, C.; Akamatsu, N.; Domen, K. *Appl. Spect.* **1992**, *46*, 1051.

[12] Lu, R., Gan, W., Wu, B., Zhang, Z., Guo, Y. and Wang, H.F. *J. Phys. Chem. B* **2005** *109*, 14118.

[13] Wang, C., Groenzin, H., Shultz, M.J., *J Phys. Chem B* **2004**, 108, 265.

[14] Hatch, S.R., Polizzotti, R.S., Dougal, S., Rabinowitz, P., *J. Vac. Sci. Technol. A* **1993,** *11*, 2232.

[15] Wang, J.; Chen, C.; Buck, S. M.; Chen, Z. *J. Phys. Chem. B.* **2001**, *105*, 12118.

[16] Zhang, D.; Shen, Y.R.; Somorjai, G.A. *Chem. Phys. Lett.* **1997**, *281*, 394.

[17] Wei X. Zhuang XW. Hong SC. Goto T. Shen YR. *Phys. Rev. Lett.* **1999***, 82,* 4256.

[18] D. Zhang, D. H. Gracias, R. Ward, M. Gauckler, Y. Tian, Y. R. Shen, and G. A. Somorjai *J. Phys. Chem. B;* **1998;** *102*, 6225.

[19] Binnig, G.; Quate, C.F.; Geber, C. *Phys. Rev. Letters*, **1986**, *56*, 930.

[20] W. C. Oliver, G. M. Pharr, *J. Mater. Res.* **1992**, *7*, 1564.

[21] Roberts, R.F.; Allara, D.L., Pryde, C.A., Buchanan, D.N.E.; Hobbins, N.D. *Surf. Interface. Anal.* **1980**, *2*, 5.

[22] Tajima, S.; Komvopoulos, K., *J. Phys. Chem. B* **2005**; *109*, 17623

# Chapter 2

# Enhancement of sum frequency generation (SFG) vibrational spectroscopy sensitivity at problematic interfaces

## 2.1 Introduction to total internal reflection (TIR) SFG

A brief overview of important influences on SFG sensitivity when the interface optical properties change will be first provided for intrinsic purposes. A buried interface is defined as the boundary between two materials, such as solid/solid or solid/liquid interfaces. Investigations of these surfaces present particular difficulties. A few instances where it has successfully been applied to buried interfaces are presented. The advantages of SFG and the use of local fields to enhance the sensitivity at the desired interface are discussed. Finally, the signal improvement by TIR enables the study of structures less than the wavelength of light and surface plasmon modes are explored.

SFG vibrational spectra of interfaces are obtained by employing intense electric fields and measuring the light generated from a nonlinear process. The sum frequency polarization, $\vec{P}^{(2)}$, at the interface is given by Eq. 2-1, where $\overset{\leftrightarrow}{\chi}^{(2)}$ is the second-order

nonlinear susceptibility of the polymer and $\vec{E}(\omega_{vis})$ and $\vec{E}(\omega_{ir})$ are the vector quantities

of the two input fields. [1]

$$\vec{P}^{(2)}(\omega_{sfg}) = \tilde{\chi}^{(2)}(\omega_{sfg}) : \vec{E}(\omega_{ir})\vec{E}(\omega_{vis}) \qquad (2\text{-}1)$$

The intensity of the generated sum frequency signal is given by Eq. 2-2 and is

proportional to the square of the effective surface nonlinear susceptibility, $\chi_{eff}^{(2)}$.

$$I_{sfg}(\omega_s) \propto \left|\chi_{eff}^{(2)}\right|^2 \qquad (2\text{-}2)$$

The effective surface nonlinear susceptibility is given by Eq. 2-3 where $\hat{e}$ is the unit

polarization vector and $\vec{L}(\omega)$ are Fresnel factors, which are strongly dependent on the

refractive indices of the two media forming the interface and the incident angles. In

quantitatively comparing SFG signals generated from different types of interfaces

(polymer/air vs. polymer/liquid) or SFG signals that were collected using different

polarization combinations of light, it is necessary to account for these differences using

Eq. 2-3. The field intensity at the interface can be calculated by superimposing the

incident and reflected fields.[2] The electric field at the interface is related to the electric

field of a plane wave in the incident medium through the Fresnel equations. *L* denotes the

ratio of the electric field intensities at the interface in a specified coordinate direction and

the incident medium. Therefore, the intensity of the SFG signal can be related to the

laboratory coordinate vectors $\hat{e}$ through the effective nonlinear susceptibility $\tilde{\chi}^{(2)}$.

Hence, Eq. 2-2 can be written as

$$\chi_{eff}^{(2)} = \left[\hat{e}_{sfg} \cdot \vec{L}(\omega_{sfg})\right]\tilde{\chi}^{(2)} : \left[\hat{e}_{ir} \cdot \vec{L}(\omega_{ir})\right] \cdot \left[\hat{e}_{vis} \cdot \vec{L}(\omega_{vis})\right] \qquad (2\text{-}3)$$

To connect the macroscopic electric field strength in air (experimentally measurable) to

the field at the interface, Fresnel's equations account the effects due to the superposition

of incident and reflected fields and smaller local field corrections from issues like induced dipoles in surrounding media.[3] We use the symbol $L_{s,y}$ for the calculated ratio of the electric field in the *y*-direction in the surface plane to the s-polarized beam in the incident medium (experimentally measured). The enhancement at a buried interface in total internal reflection can increase the signal by orders of magnitude.[4]

Fig. 2-1 shows the spectrum of acetonitrile at the sapphire interface. The spectrum was collected in *ssp*, with only 20 shots per data point. Collection time is approximately ten times less (then internal reflection compared to external reflection) due to the signal intensity. The asymmetric stretch of acetonitrile is visible alongside the dominant symmetric $CH_3$ at 2940cm$^{-1}$. Although the Somorjai group has published eight papers on acetonitrile, TIR has provided the first observation of the asymmetric peak.
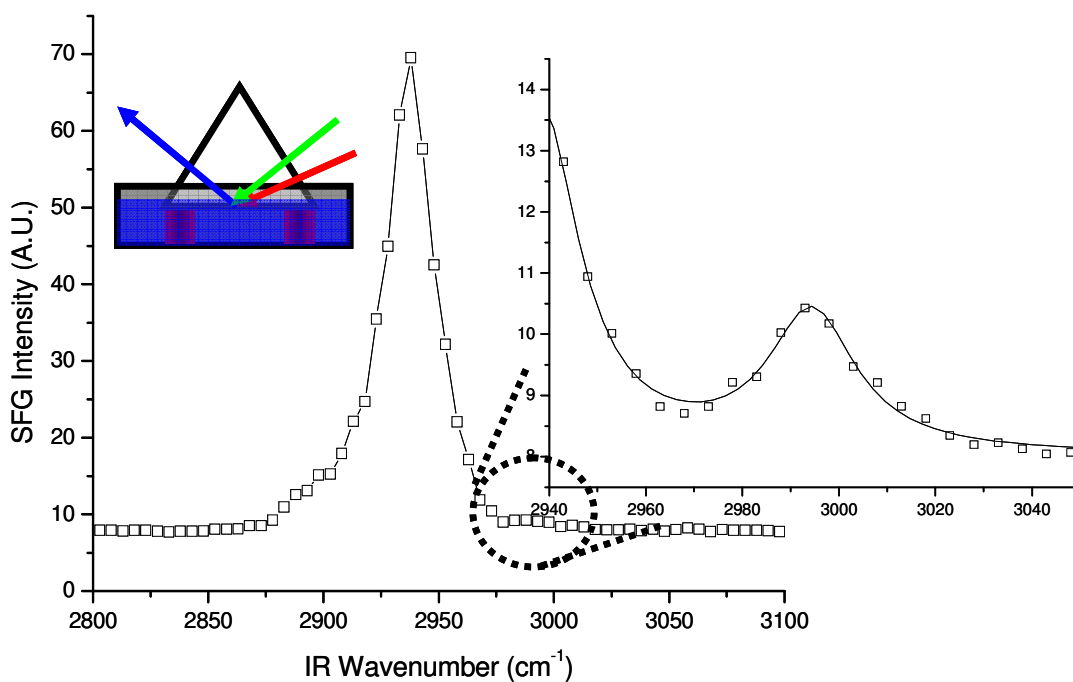


**Figure 2-1:** SFG spectrum generated in ssp polarization of the acetonitrile/sapphire interface.

## 2.2 TIR-SFG field enhancement and Fresnel coefficients

The electric fields in all of the presented experiments pass through multiple interfaces. Therefore it is important to understand how the Fresnel coefficients affect the signal intensity at a given interface. For example, a thin (100nm) polymer film on a solid substrate is explored. In order to compare the signal generated from the air/polymer and the polymer/glass interfaces, the SFG equation (*ssp*) is expanded as

$$I_{sfg}(\omega_s) = \frac{2e_0 A\tau \cos\theta_{sfg,s} I_{vis,s} I_{ir,p}}{\hbar\omega_{sfg}c} \left| L^r_{sfg,s} \chi^{(2)}_{yyz} L^i_{vis,s,y} L^i_{ir,p,z} \right|^2 \tag{2-4}$$

where $L^r_{sfg,s,y}$, $L^i_{vis,s,y}$ and $L^i_{ir,p,z}$ are the reflected sum frequency and incident visible and infrared Fresnel coefficients at s and p polarizations. $A$ and $\tau$ are the spatial and temporal overlap, $\hbar$ is Plank's constant, and $\theta_{sfg}$ is the azimuthal angle between the wavevector of the emitted SFG and the surface normal.

Three chief features that dominate the Fresnel factors are the change in index of refraction across the interface, and its dependence on angle and on the wavelength of light. For example, SFG spectra are collected at the same incident angle, concentrating on the atactic polypropylene (aPP) surface in air, the aPP/glass interface, and the aPP/sapphire interface (Fig. 2-2). Even though glass and sapphire have similar surface energy and active chemical groups, the SFG spectra are distinct. Almost no SFG is measured from the aPP/glass interface ($I_{sfg}(\omega_s) \neq 0$, but the intensity is at the noise level). This is due to the different changes in index of refraction at the material interfaces. Air/aPP is approximately 1/1.4, glass/aPP is 1.45/1.4, and sapphire/aPP is 1.8/1.4. When the change in index of refraction is large, there is an automatic increase in the local field

29

due to the Fresnel coefficients. Because the reflection increases when the index change across the interface increases, more of the electric fields superimpose, and the resulting local filed is bigger.
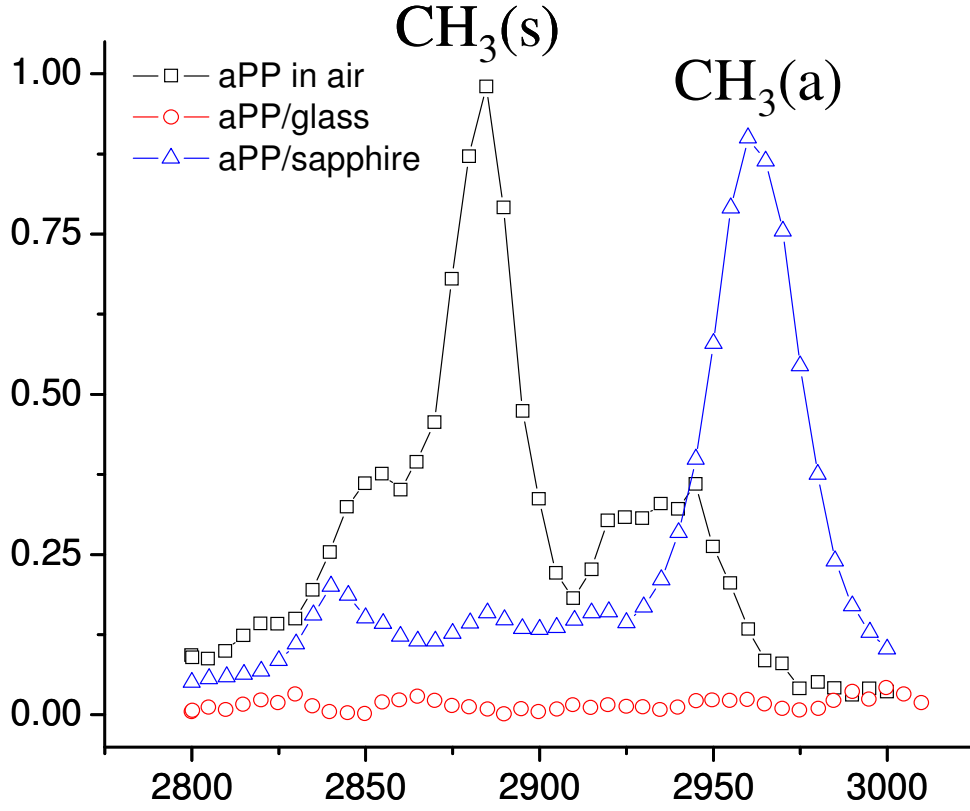


**Figure 2-2:** SFG spectrum generated in ssp polarization of the acetonitrile/sapphire interface.

In order to quantify $L$, the reflection coefficient is found for p polarized light[5]

$$r_p = \frac{n_t \cos\theta_i - n_i \cos\theta_t}{n_t \cos\theta_i + n_i \cos\theta_t} \qquad (2\text{-}5)$$

where $n_i$ and $n_t$ are the complex refractive indices of the incident and transmitted media and both $\theta_i$ and $\theta_t$ are incident and transmitted angles with respect to normal. The term $\cos\theta_t$ can be the real or complex number associated with Snell's law $\left(1 - \sin^2\theta_t\right)^{1/2}$. The modulus of $L^i_{ir,p,z}$ can therefore be calculated in Eq 2-6.

$$\left|L^i_{ir,p,z}\right| = \left|\left(1 + r_p\right)\sin\theta_i\right| \tag{2-6}$$

Throughout the calculations, the interfacial region and polymer monolayer is assumed to have the same index has the index as the bulk. The variation of $L$ with incident angle is demonstrated in Fig. 2-3. The incident angles are chosen to maximize the local field at the interface of interest. By calculating the critical angle ($\sin\theta_t = 1$) from known values, experiments are designed to have the desired incident angles.
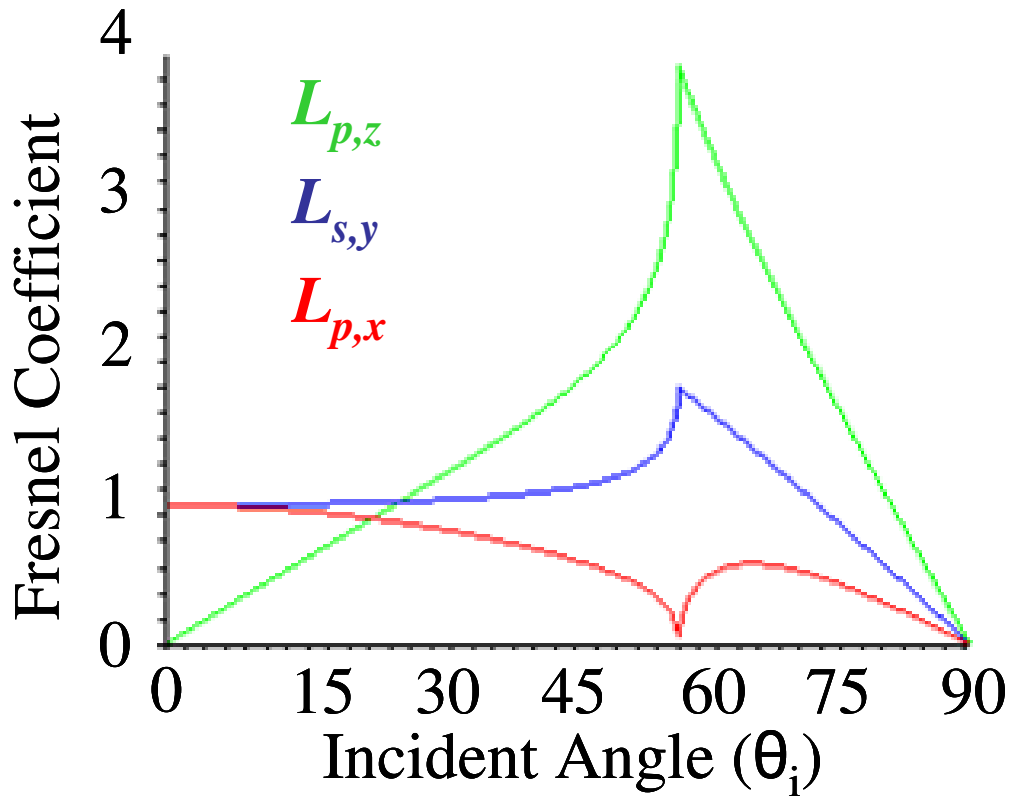
**Figure 2-3:** Calculated Fresnel Coefficient dependence on the incident angle for the polystyrene/sapphire interface.

By tuning the incident angles of the IR and VIS (thereby changing the angle of sfg as well) multiple Fresnel coefficients can increase signal intensity by up to 100-fold. Fig. 2-4 shows the Fresnel coefficients as a function of both IR and VIS incident angles. An overall maximum is apparent for each input beam in the given domain.
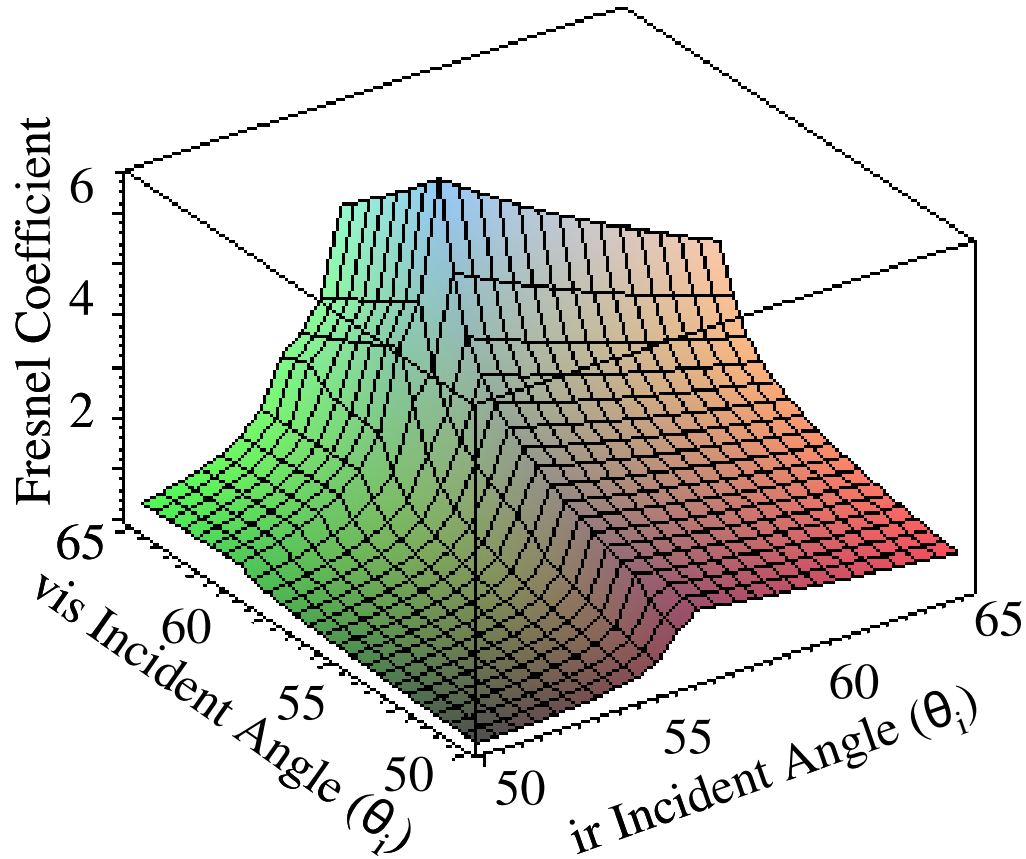
**Figure 2-4:** Calculated $\left| L^i_{vis,s,y} L^i_{ir,p,z} \right|$ dependence on the incident angle for the polystyrene/sapphire interface.

## 2.3 Important considerations due to dispersion

The variation of $L^i_{ir,p,z}$ with wavelength is due to the dispersion of the materials present at the interface. The dielectric properties of the media depend on the wavelength in a well known manner. This behavior is most evident when white light is separated based on its wavelength in a prism. Since the index of refraction is wavelength dependent, the angles at which each frequency exits is slightly different. The nonlinear nature of this system complicates it even further. The emission angle of the SFG varies

with wavelength since the conservation of momentum will bias the produced photon in the direction of the more energetic light. Since the incident ir and sfg wavelength, and sfg angle are changing as the IR is scanned during the course of an experiment, the Fresnel coefficients can vary dramatically.

In order to avoid this correction, optimum angles can be chosen that maximize the enhancement and minimize the effect of dispersion. Slightly above the critical incident angle ($\theta_t = \frac{\pi}{2}$) in Fig. 2-3 (~62° from normal) enhances the SFG from the PS/sapphire interface while the correction due to dispersion is less than 5%. Water poses an especially problematic challenge since the ir absorption changes the dielectric properties significantly.[6] Fig. 2-5 demonstrates the calculated Fresnel coefficients for the sapphire water interface as a function of ir wavenumber and incident angle. As shown, $L_{ir,p,z}^{i}$ peaks sharply near the IR critical angle, which is determined by the refractive indices of the bounding media, water. If the dielectric of one material varies, $L_{ir,p,z}^{i}$ will change accordingly. In this situation, it occurs when the infrared is scanned over a resonance. The refractive index of water changes from 1.46 to 1.12 around the OH resonance.[7] If the critical angle is chosen for an experiment involving water, the SFG spectrum will appreciably respond to the local field changes instead of the desired $\ddot{\chi}^{(2)}$ resonances. This will result in a spectrum identical to a bulk absorption scan instead of an SFG spectrum. Enhancement can still be achieved at the interface of interest, but the beam must be set far from the critical angle. Moreover, since water attenuates light drastically, interface specificity at the polymer/water interface is usually a negligible problem.
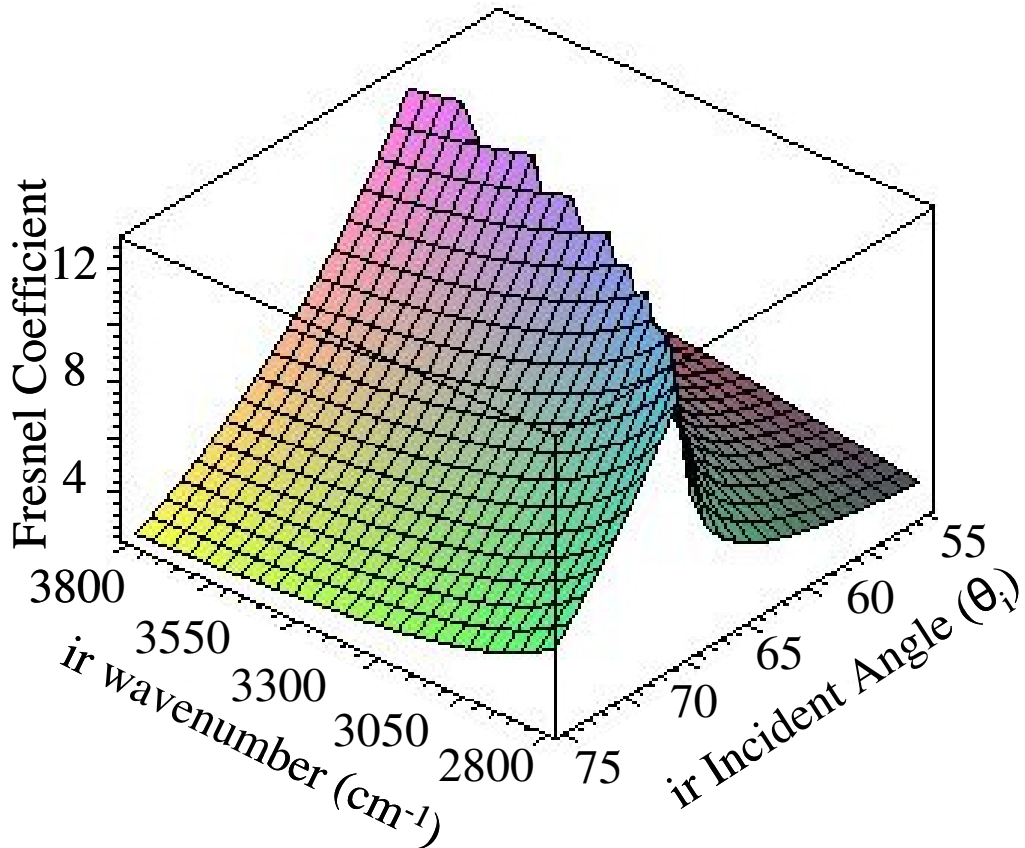
**Figure 2-5:** Calculated $L^i_{ir,p,z}$ Fresnel Coefficient dependence on the infrared incident angle and frequency for the pHEMA/water interface.

## 2.4 Interface sensitivity and specificity due to Fresnel enhancement

When multiple interfaces are present, careful selection of incident angle can provide specificity by washing out the signal from undesired surface. Fig. 2-6 demonstrates a case where choosing a specific incident angle can enhance the SFG signal from various interfaces of a poly(2-hydroxyethyl methacrylate) (PHEMA) thin film. These Fresnel factors can be further exaggerated by tuning the IR, VIS and SFG angle for maximum local field.
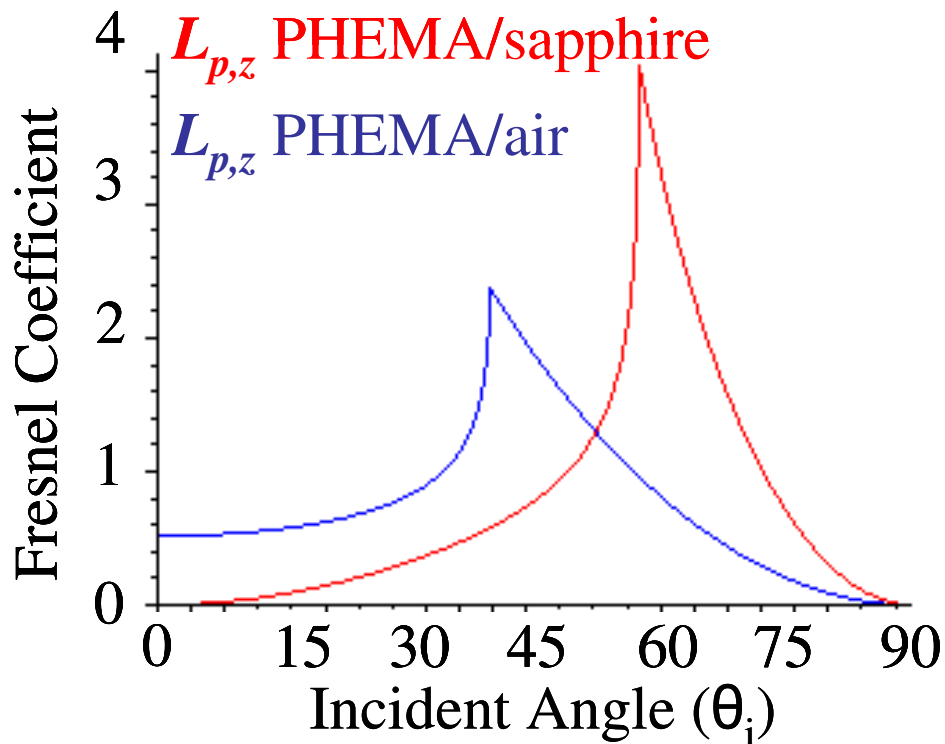
**Figure 2-6:** Calculated $L^i_{ir,p,z}$ Fresnel Coefficient dependence on the incident angle for

the pHEMA/sapphire and pHEMA/air interfaces.

Thus, TIR at the solid/solid or solid/liquid interfaces amplifies the signal such that

it overwhelms any SFG signal from an unwanted surface. Even more important, signal

that was otherwise impossible to observe (at the noise level) is enhanced. By careful use

of exact complex dielectrics and cautious normalization, signal sensitivity and specificity

are achieved. Consideration of the complex dielectric is very important when

investigating platinum (the subject of the next section).

## 2.5 Local field enhancement due to plasmon modes in nanoparticles

Plasmonics have fascinated people for centuries. During the middle ages and Qing dynasties, Europeans and Chinese discovered that infusions of nanoparticle colloidal metal particles in glass produced brilliant colors for objects like cathedral windows and vases.[8] The colors are due to the resonant modes of bound oscillations of electron in the particle. The conduction electrons in the metal are free to move and the electric field of incoming light produces a polarization. At the surface, the net charge produces a restoring force, and the electrons oscillate coherently. Noble metals like silver, gold and copper are commonly used in plasmon studies because their nanoparticle resonances occur in the visible region. This effect is not restricted to particles. Films, wires and dielectric/metal interfaces may also support plasmons.

The optical properties of metal nanoparticles have been the subject of intensive research because of their applications in areas such as surface enhanced spectroscopy[9,10] and chemical/biological sensing.[11,12] This optical response is collectively known as localized surface plasmon resonance (LSPR). A localized surface plasmon can act as nano-antennae, concentrating energy in the nanoscale region surrounding the particle known as a physical enhancement. Large fields can be created in the gaps between particles as well as the edges. Mie theory, developed in 1908, can be used to understand LSPR for a sphere.[13] For more intricate shapes complex numerical electrodynamic theories have been developed. Finite difference time domain (FDTD) is a common technique that explores the local field dynamics around diverse geometries.[14] Due to

these large shape and size dependent electromagnetic enhancements, surface spectroscopy can be performed with greater sensitivity and specificity.

The increased surface intensity of electromagnetic fields may be due to a chemical or physical enhancement. Chemical enhancement mechanisms are often due to the formation of a new surface complex that contains electronic transitions that are resonant with the field oscillation. [15,16] For CO on platinum, this mechanism might contribute because of the electronic coupling,[17] but the physical enhancement probably dominates in the case of small particles.

Since the mean free path of the conduction electrons is less than the particle dimensions we must consider the size dependent complex dielectric of Pt (Bulk refractive index for platinum in the ir is -1.96+3.42i). The size dependent $\varepsilon$ follows Drude-Sommerfeld theory.[18,19] Shown in Fig. 2-7, as the dimensions of the particle shrink, the imaginary component of the dielectric increases. A 7 nm platinum particle feels a 207% increase in the dielectric whereas the visible and sfg see less than a 2% increase.
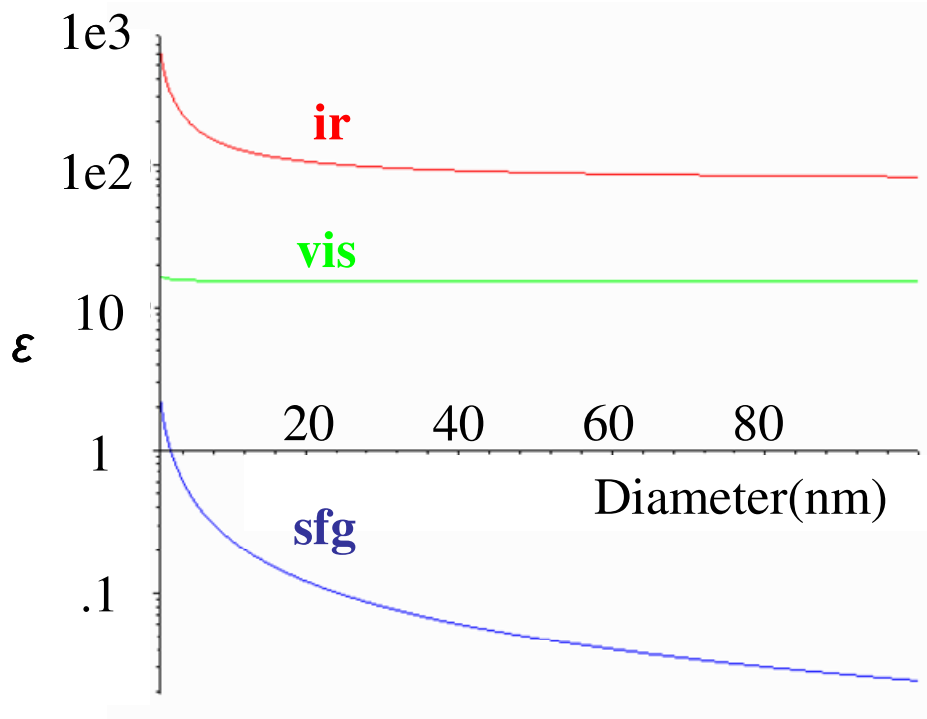
**Figure 2-7:** Calculated $\varepsilon$ dependence on platinum nanoparticle size (logarithmic scale).

The local field enhancement due to plasmon resonance is shown in Eq. 2-7 where $\varepsilon$ is the size dependent complex dielectric of platinum, and A is the depolarization factor (shape). The particle size and shape is explicitly included in the Mie resonance criteria. As the geometry shifts from spherical to ellipsoidal to rod-like, the resonance shifts to lower energies. Therefore, since the incident beam is visible, the more needle-like the shape, the more enhancement (e.g. lightning rod effect). Qualitatively, any small shape would produce some local field amplification for polarizability spectroscopies due to the polarization of the conduction electrons.

$$E_{pr}^2 = \frac{|\varepsilon|^2}{\left\{1 - [1 - \mathrm{Re}(\varepsilon)]A_{eff} + \mathrm{Im}(\varepsilon)\left(4\pi^2 V / 3\lambda^3\right)\right\}^2 + \left\{\mathrm{Im}(\varepsilon)A_{eff} + [1 - \mathrm{Re}(\varepsilon)]\left(4\pi^2 V / 3\lambda^3\right)\right\}^2} \quad (2\text{-}7)$$

where $\varepsilon$ is the complex dielectric, $A_{eff}$ is the depolarization factor (shape). The depolarization ratio decreases from 0.5 (rod) to .3 (sphere). The term $\left(4\pi^2 V / 3\lambda^3\right)$ of Eq. 2-7 is due to the radiation damping, or boundary conditions of the particle. $V$ is the particle volume and $\lambda$ is the wavelength of light. This term accounts for the change in enhancement and resonant frequency with size. Fig. 2-8 demonstrates the effect of particle size and shape on the enhancement factor
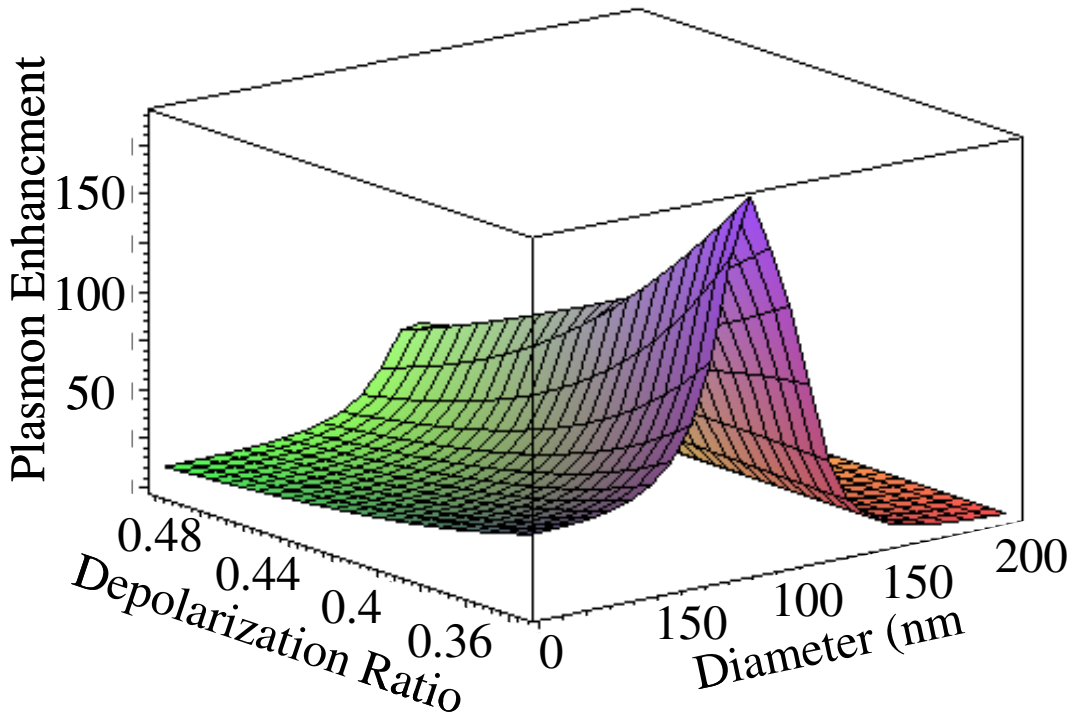


**Figure 2-8:** Enhancement of SFG, calculated as a function of size and depolarization ratio for platinum nanoparticles.

Therefore, Eq. 2-7 predicts a large enhancement depending on the size and shape of the field. Additionally, the localized "hot spots" caused by the lightning rod effect will likely produce high electromagnetic intensity at the corners of a cube. The consequence polarized electron is improved signal intensity at the surfaces and edges of nanoparticles.

40

## 2.6 Detection of SFG from centrosymmetric media by TIR

The fundamental limitation on the size of a particle for nonlinear optical studies has been the wavelength of light. When the dimension of a feature is less than the wavelength of light, destructive interference occurs between $\ddot{\chi}^{(2)}$ active species on opposite sides. Essentially, the particle becomes an ensemble that exhibits inversion symmetry. Using TIR, Yeganeh et. al[20] has demonstrated that light can be manipulated on small particles to avoid strong interference effects. When considering a slab with equal numbers of adsorbed molecules on both the top and bottom of the film, the sfg intensity is a function of the electric field of the incoming laser beams and the distance between the molecules. This setup produces few photons for sizes less than a few microns. In TIR geometry, the amplitude of the electric fields decays exponentially away from the surface reducing the effect of destructive interference. Fig. 2-9 demonstrates the sfg light scattering from the slab in both external reflection and TIR geometries.
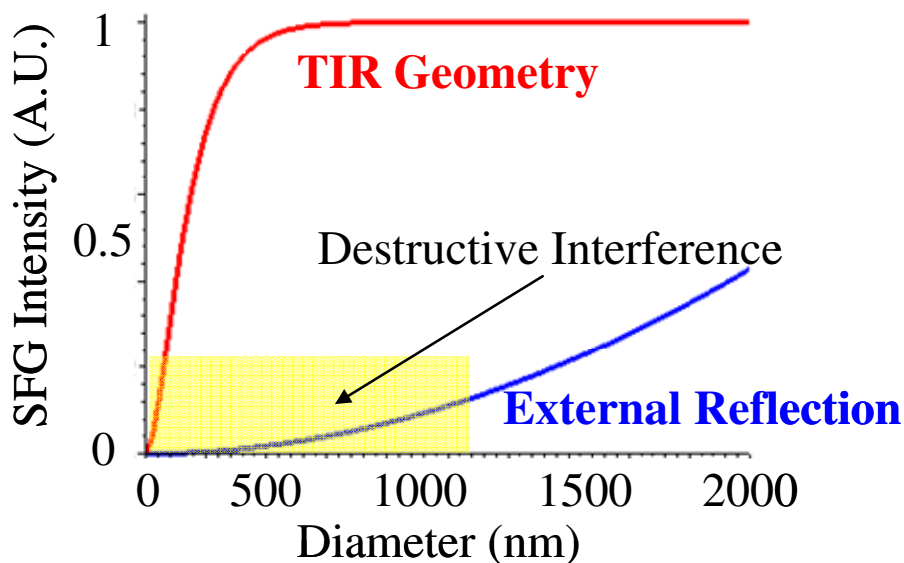
**Figure 2-9:** Variation of sfg intensity with particle size in TIR and external reflection geometry.

It should be noted that in the previous plot (idealized situation of a perfect slab), the calculation of the SFG intensity does not take into account the orientation distribution. Since, realistically, the molecules at opposing sides of particles of a slab usually have a broad distribution and/or surface roughness, inversion symmetry is expected to be broken to some extent. Also, signal intensity will vary with small changes in the environment (dielectric constant) around the sample. In the same manner, the transmission across a high dielectric material in reflection geometry will attenuate the scattered light from the far side of the slab. Even though the origin of the signal is complicated by this geometry enhancement from this critical material is essential and advantageous.

# References

[1] Shen, Y.R., *Principles of Nonlinear Optics*, John Wiley & Sons, New York, 1984.

[2] Knock, M. M.; Bell, G. R.; Hill, E. K.; Turner, H. J.; Bain, C. D.; *J. Phys. Chem. B* **2003**, 107, 10814.

[3] Ye, P., Shen, Y.R., *Phys. Rev. B* **1983**, 28, 4288.

[4] Hatch, S.R., Polizzotti, R.S., Dougal, S., Rabinowitz, P., J. *Vac. Sci. Technol. A* **1993**, 11, 2232.

[5] Born, M., Wolf, E., Principles of Optics, $6^{th}$ ed.; Cambridge University Press; Cambridge, U.K. 1980 pg. 40.

[6] P. B. Miranda and Y. R. Shen *J. Phys. Chem. B*; **1999;** *103*, 3292.

[7] Conboy, J.C., Messmer, M.C., Richmond, G.L., *J. Phys. Chem.* **1996;** *100*, 7617.

[8] http://www.ceramicsglasscircleaustralia.org/catchineseglasstaster.html

[9] Haynes, C. L.; Van Duyne, R. P. *J. Phys. Chem. B* **2003**, *107*, 7426.

[10] Hao, E. C.; Schatz, G. C.; Johnson, R. C.; Hupp, J. T. *J. Chem. Phys.* **2002**, *117*, 5963.

[11] Haes, A. J.; Zou, S.; Schatz, G. C.; Van Duyne, R. P. *J. Phys. Chem. B* **2004**, *108*, 6961.

[12] McFarland, A. D.; Van Duyne, R. P. *Nano Lett.* **2003**, *3*, 1057-1062.

[13] Mie, G. *Ann. Phys.* **1908**, *25*, 377.

[14] Chang, S.-H.; Gray, S. K.; Schatz, G. C. *Opt. Express* **2005**, *13*, 3150.

[15] Hallmark V. M., and Campion, A. *J. Chem. Phys.* **1986** *84*, 2933.

[16] Kambhampati, P., Child, C.M., Foster, M.C., and Campion, A. *J. Chem. Phys.* **1998** *108*, 5013.

[17] Chou, K.C., Westerberg, S., Shen, Y.R., Ross, P.N., and Somorjai, G.A. *Phys. Rev. B* **2004,** *69,* 15.

[18] Kreibig U., and Fragstein,C.V., *Phys.* **1969** *224*, 307.

[19] Bergman, J.G., Chemla, D.S., Liao, P.F., Glass, A.M., Pinczuk, A., Hart, R. M., and Olson, D.H. *Opt. Lett.* **1981** *6,* 33.

[20] Yeganeh, M. S.; Dougal, S. M.; Silbernagel, B. G. *Langmuir* **2006,** *22,* 637.

# Chapter 3

# Contact interfaces with compressed polymer films

## 3.1 Introduction

The contact between polymer and solid surfaces is of great significance in various fields of science and technology where effective operation and longevity of components are strongly dependent on adhesion and friction phenomena occurring at contact interfaces. Adhesion and wetting of polymers are important properties controlled by the polymer molecular structure at the interface with the contacting solid. The mechanical properties of polymer surfaces, such as elastic modulus and yield strength, are greatly affected by the interface molecular structure and chemical composition.[1,2,3,4] However, techniques that enable probing the polymer surface structure at buried interfaces are sparse and provide limited molecular-level specificity. Vibrational resonant sum frequency generation (SFG) spectroscopy is a surface-specific spectroscopic technique with monolayer sensitivity, which can yield information about the molecular

45

conformation at polymer surfaces.[5] SFG has been used to examine the molecular structure and behavior of polymer surfaces and self-assembled monolayers under various environments, such as adsorbed molecules, humidity, temperature,[6,7] and mechanical effects (e.g., compression, stretching, and rubbing).[8,9,10] The amplitude, polarization, and resonance frequencies of the SFG spectrum can be used to determine the polymer chemical composition and structure at interfaces under in situ conditions.

Buried interfaces of deformed monolayers demonstrate a range of reversible and permanent effects in the SFG spectra at high pressures. SFG studies have been performed for compressed organic coatings, such as Langmuir-Blodgett films and self-assembled monolayers.[11,12] An enhancement of the SFG sensitivity by orders of magnitude was obtained at incident angles resulting in total internal reflection (TIR).[11,12] To achieve TIR at the solid/polymer interface, optically transparent bodies in both infrared and visible regions with high refractive indices (e.g., sapphire and zirconia) must be brought into contact with the polymer surfaces. Interface specificity and sensitivity has been demonstrated in studies in which outward tilting of aromatic groups was detected at the polystyrene/sapphire interface.[13]

Basic understanding of the orientation of surface functionalities and ordering of polymeric materials is important to the design of interfaces with specific properties. At the air interface, a number of SFG studies have shown that well-ordered hydrophobic side branches are are oriented away from the polymer bulk.[14,15,16,17,18] Two contributing factors have been found (1) air is considered hydrophobic, thus hydrophobic side branches should be favored and (2) the low density air interface (an increase in free volume) may favor a large concentration of bulky side branches in the interface region.[19]

Amorphous polymers are more desirable than crystalline polymers for investigating molecular ordering and dynamic processes at surfaces of conforming plastics due to their more homogeneous structures. The objective of this chapter is to examine changes in the surface molecular structure of annealed poly(n-butyl methacrylate) (PBMA) and poly(methyl methacrylate) (PMMA) spin cast on fused quartz due to compression by a smooth sapphire surface. Polymer films cast from toluene solution directly on the sapphire surface and, subsequently, thermally annealed were also examined to evaluate the effect of conformation chemical equilibrium on the surface molecular structure. Changes in the surface molecular structure of the compressed (deformed) polymers are discussed in light of SFG spectra and differences in the glass transition temperature of the polymers.

## 3.2 Experimental Procedures

The occurrence of vibrational modes, which are both Raman and IR active and exist where symmetry is broken, enhances the SFG signal significantly. In this study, two different polarization combinations of input-output laser beams were used to obtain the SFG spectra, i.e., $s_{sfg}s_{vis}p_{ir}$ and $p_{sfg}p_{vis}p_{ir}$, where $s$ and $p$ denote $s$- and $p$-polarized beams, respectively. SFG spectra for $s_{sfg}p_{vis}s_{ir}$ polarization combination were also obtained but are not presented here because interpretation is difficult due to the low signal intensity. Hereafter, the above polarizations will be referred to as $ssp$ and $ppp$ for simplicity. These polarization combinations were used to excite different vibration modes and to study changes in the molecular orientations at the polymer/air and polymer/sapphire interfaces.

**Apparatus and Data Acquisition**. The tunable IR beam is combined with the 532-nm visible light at the sample interface at incident angles of ~58° and ~63° from the surface normal, respectively. The SFG signal from the sample is collected by a photomultiplier tube, transmitted to a gated integrator, and stored digitally. For each scan, data was obtained at increments of 5 cm$^{-1}$ in the range of 2800-3100 cm$^{-1}$ using 100 shots per data point. The SFG spectra were normalized by the product of the IR and visible intensities. Normalization of the Fresnel coefficients was ignored because it did not yield a significant effect on the results. For each experimental condition, SFG measurements were repeated at least three times to increase the signal-to-noise ratio, and the final spectra were obtained by averaging the data recorded from each similar experiment.

**Sample Preparation**. Specimens were fabricated from powders of commercially available polymers with different molecular weight $M_w$ and glass transition temperature $T_g$, namely PBMA ($M_w = 330000$, $T_g \approx 15$ºC), PMMA ($M_w = 102000$, $T_g \approx 105$ºC), and poly(methacrylate) (PMA) ($M_w = 30000$, $T_g \approx 9$ºC) all from Aldrich, St. Louis, MO, and ester methyl deuterated poly(methyl methacrylate) (d3-PMMA) ($M_n = 19000$, $T_g \approx 105$ºC) from Polymer Source, Dorval, Quebec, Canada. The chemical structures of these polymers are shown in Fig. 3-1. Polymer films were spin cast at 3000 rpm directly onto fused quartz or sapphire substrates from a d8-toluene solution (5 wt%) and annealed at 110°C for 12 h. To ensure that the SFG signal originated from the polymer material, the thickness of the spin cast polymers was maintained above 300 nm.

a)

b)

c)

d)
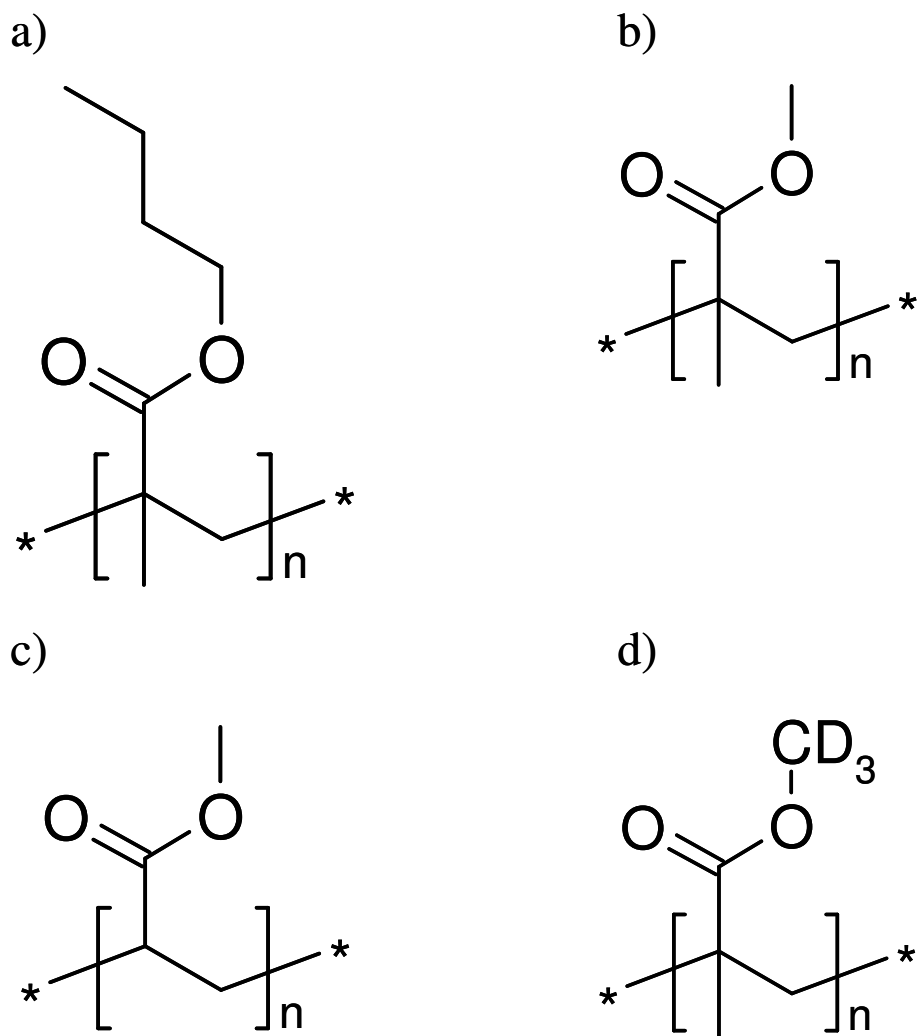
**Figure 3-1:** Molecular structures of (a) poly(n-butyl methacrylate) (PBMA), (b) poly(methyl methacrylate) (PMMA), (c) poly(methacrylate) (PMA), and (d) ester methyl deuterated poly(methyl methacrylate) (d3-PMMA).

**Testing and Characterization Techniques**. A trapezoidal prism with 60° base angles was used to compress the polymers by hydraulic means. The prism consisted of synthetic single-crystal sapphire ($\alpha$-Al$_2$O$_3$) possessing a root-mean-square roughness of 5-10 nm (Red Optronics, Mountain View, CA) with optical ĉ-axis perpendicular to the

49

free surface. The flatness of the sapphire and polymer surfaces and the polymer surface composition were examined with an atomic force microscope (AFM) fitted with an M5 head (Park Scientific Instruments, Sunnyvale, CA) and X-ray photoelectron spectroscopy (XPS) spectrometer (PHI 5300, Perkin-Elmer, Boston, MA), respectively. AFM surface mapping confirmed the flatness of the contacting surfaces, while the XPS provided information about the chemical composition and the absence of surface contaminants. The prism was cleaned with concentrated chromic acid, rinsed thoroughly in high-purity water, and, finally, exposed to UV-initiated ozone for at least 1 h. The sapphire prism was used immediately after cleaning to minimize contamination from the atmosphere. In view of the complex hydroxyl region, dangling oxygen atoms or hydroxyl groups from the sapphire surface are not addressed in the following SFG spectra. Interference from these hydroxide modes may occur as far down as the hydrocarbon region.[20] Boiling the sapphire in $D_2O$ eliminated the interference effects due to the hydroxide modes on the SFG results.[21] A small non-resonant background, which has its origins in the nonlinear susceptibility of an interface, was observed in each SFG spectrum.

## 3.3 Results and Discussion

SFG results for polymer/air interfaces and polymer/sapphire interfaces are compared in this section to determine the effect of the contacting sapphire surface on the surface molecular orientation.
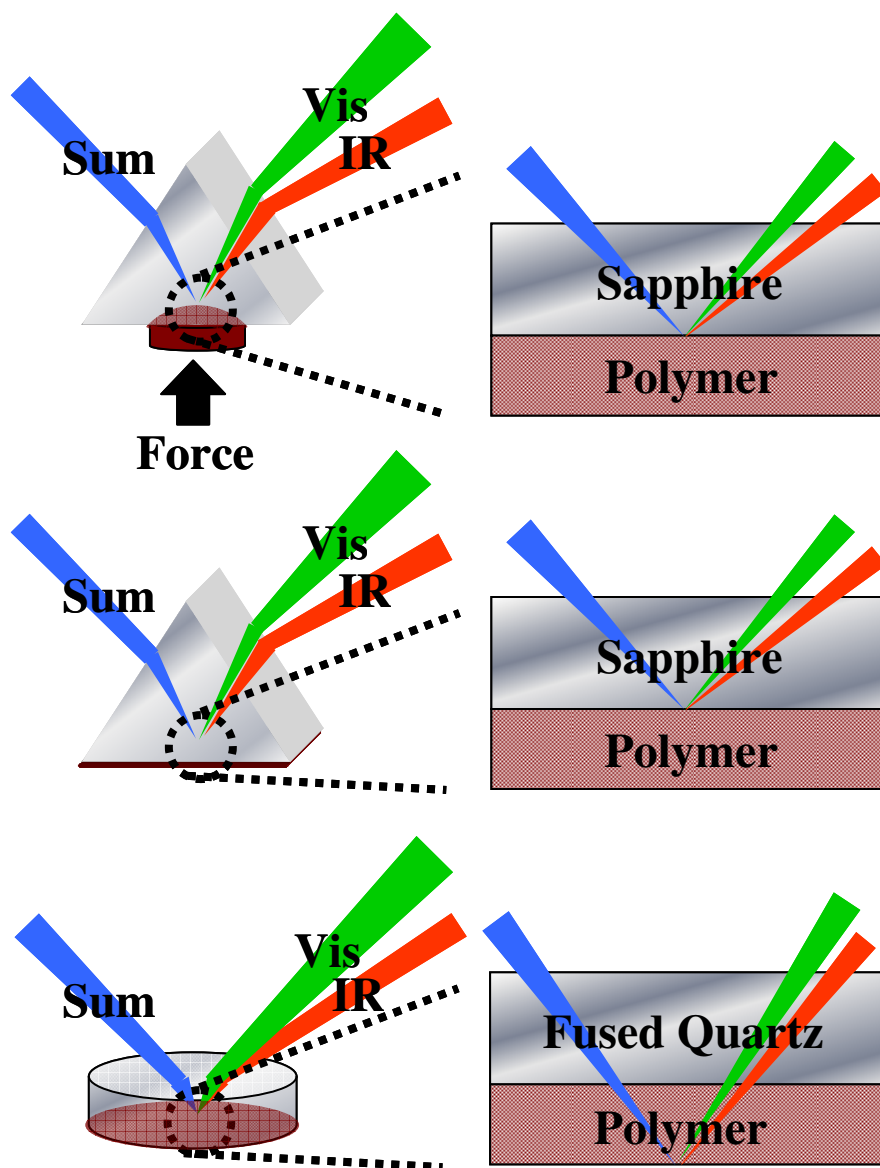
**Figure 3-2:** Schematic illustration of experimental geometries for simultaneous polymer film compression by a sapphire prism and in situ SFG spectroscopy analysis of the polymer/sapphire and polymer/air interfaces.

Hereafter, polymer surfaces exposed to ambient air, surfaces of polymers compressed by the sapphire prism, and interfaces of polymers cast on sapphire will be referred to as polymer/air, deformed polymer/sapphire, and undeformed

polymer/sapphire interfaces, respectively. The SFG experiments of the previous geometries are shown schematically in Fig. 3-2. The SFG spectra of the undeformed polymer/sapphire interfaces provide information about the conformation chemical equilibrium of the polymers on the sapphire surface.

**Polymer/air and polymer/sapphire interfaces**. SFG spectra of the polymer/air interfaces were obtained in external reflection geometry (ERG). The identical ERG-SFG spectra of the polymer/air interfaces for films spin cast on sapphire and fused quartz indicated that the substrate effect on the polymer surface structures was insignificant. SFG spectra (*ssp* polarization) of PBMA and PMMA surfaces (i.e., polymer/air interfaces) are shown in Figs. 3-3 and 3-4, respectively. The spectra are in qualitative agreement with previously published data.[22] The assignment of the vibrational modes was based on studies of the vibrational spectra of the corresponding bulk polymers and selective deuteration of the functional groups.[23] The SFG spectrum of the PBMA/air interface (Fig. 3-3) shows strong features due to the C-H stretches of the ester butyl chain. Vibrational modes of the symmetric and asymmetric methyl groups of the ester butyl side-chain [$CH_3$(s) and $CH_3$(a), respectively] and Fermi resonance appear at 2880, 2960, and 2940 $cm^{-1}$, respectively. Contributions from the ester methylene ($CH_2$) and $\Box$-methyl groups are small, and it is clear that the ester butyl $CH_3$ signal is very strong. Ester $CH_2$ vibrations corresponding to symmetric and asymmetric stretches may be observed at 2855 and 2915 $cm^{-1}$, while symmetric and asymmetric stretches of the $\Box$-methyl group can be found at 2930 and 2990 $cm^{-1}$, respectively.[6] Both SFG spectra of the PBMA/air and PMMA/air interfaces demonstrate a dominance of the $CH_3$(s) stretch of the ester side-chain, which for the PMMA/air interface (Fig. 3-4) has shifted to a higher

wavenumber (~2955 cm$^{-1}$) due to its closer proximity to the ester linkage. The highest intensity of the CH$_3$(s) stretch in the *ssp* polarization combination is obtained when the CH$_3$ group is oriented upright at the interface. The SFG spectra of the PBMA and PMMA surfaces in ambient air demonstrate a preferred orientation of the hydrocarbon ester side-chain away from the polymer surfaces, possibly due to surface energy and steric effects.
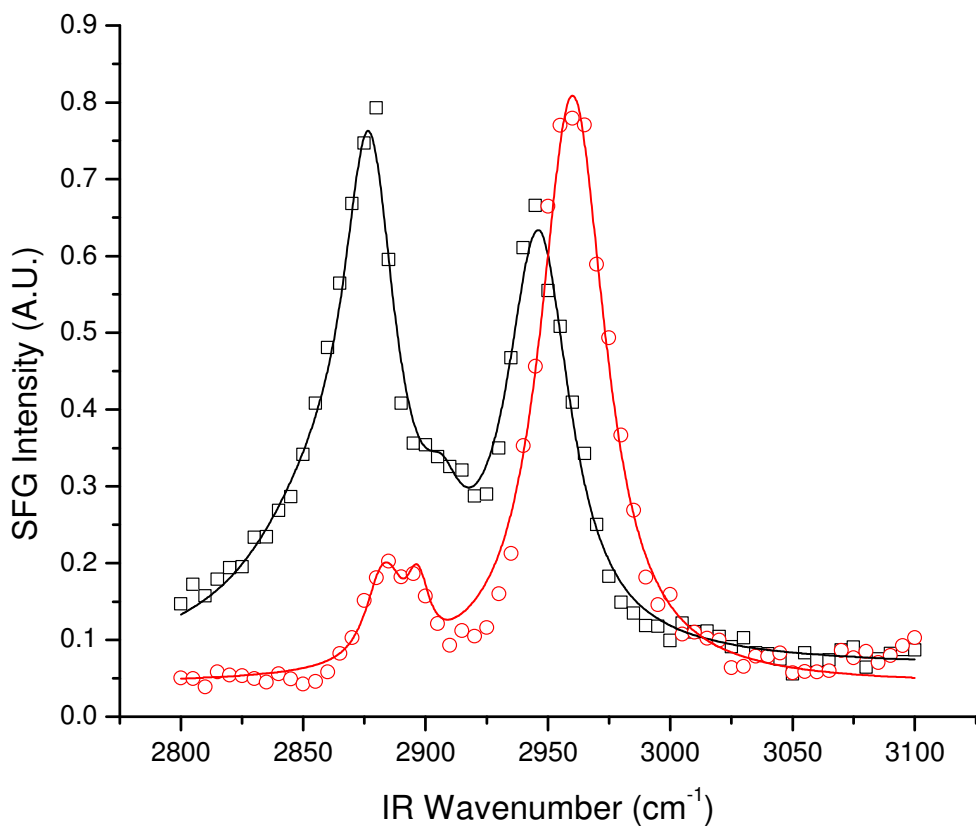


**Figure 3-3:** SFG spectra of PBMA/air (□) and deformed PBMA/sapphire (○) interfaces for *ssp* polarization combination.
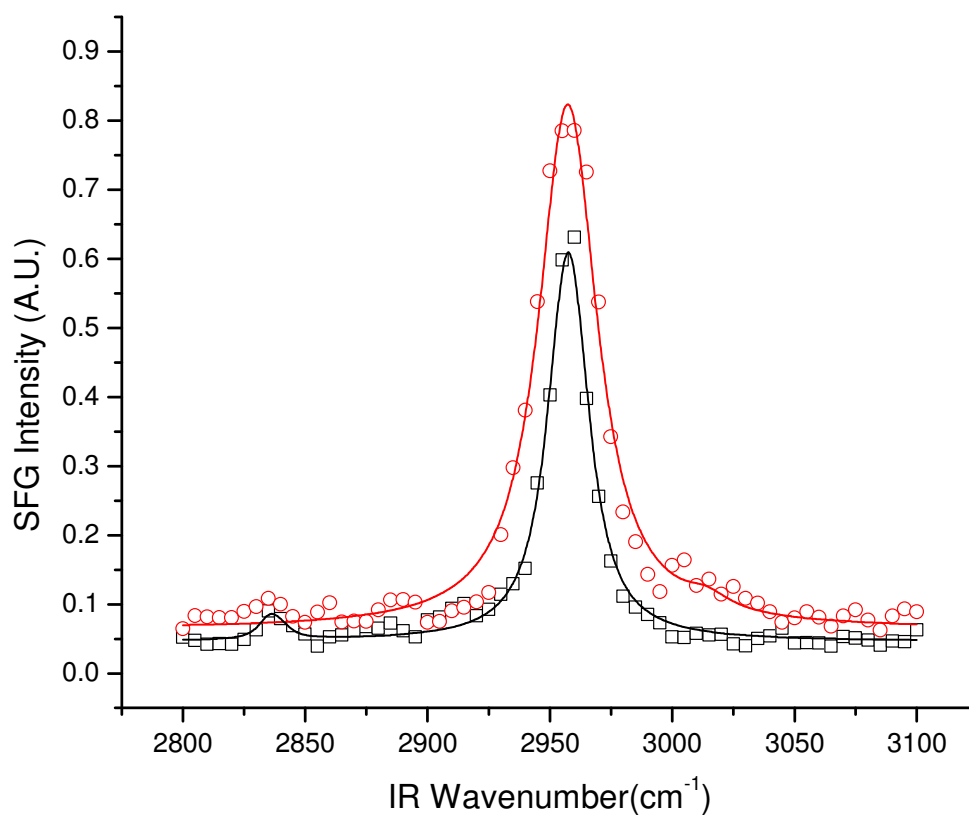
**Figure 3-4:** SFG spectra of PMMA/air (□) and deformed PMMA/sapphire (○) interfaces for *ssp* polarization combination.

A comparison of the SFG spectra of the PBMA/air and PBMA/sapphire interfaces, shown in Fig. 3-3, indicates that contact and compression of the sapphire prism produced profound changes in the chemical conformation of the ester butyl-chain $CH_3$ groups. The $CH_3(s)$ stretch at 2880 cm$^{-1}$ decreased significantly, while the intensity of the $CH_3(a)$ at ~2960 cm$^{-1}$, which is absent in the PBMA/air interface, is the dominant feature in the spectrum of the deformed PBMA surface. The smaller contribution of the peak at ~2880 cm$^{-1}$ is attributed to the symmetric stretch of the side-chain methyl group

[CH$_3$(s)]. Therefore, the PBMA surface underwent molecular restructuring upon contact with the sapphire surface, which can be attributed to changes in the surface chemical environment and the presence of a hard wall. The hydrocarbon side-chain alters its configuration to allow the more hydrophilic ester carbonyl and acyl carbon to interact with the oxide surface. This restructuring of the PBMA surface was observed immediately after contact with the sapphire surface. However, increasing the contact pressure by a factor of 3-4 produced negligible additional changes in the SFG spectrum.

Conversely to PBMA, compression of the PMMA did not yield any discernible changes in the SFG spectrum (Fig.3-4). A dominant stretch at 2955 cm$^{-1}$ still originated mainly from the CH$_3$(s) of the ester methyl group, as confirmed by the SFG results for d3-PMMA presented below. It is well known that the origin of the 2955 cm$^{-1}$ peak at the surface of PMMA exposed to ambient air is due to the CH$_3$(s) stretch of the ester methyl chain.[19] This moiety orients perpendicular to the free polymer surface. At the instant of contact, well-ordered ester methyl groups and disordered α-methyl groups from the polymer backbone dominate the PMMA surface. The close similarities of the features and corresponding intensities in the SFG spectra of the PMMA/air and deformed PMMA/sapphire interfaces indicate that the molecular conformation at the polymer/air interface was maintained at the deformed PMMA surface. Similar results have been reported for PMMA/water and PMMA/silanized interfaces.[24,25] Molecular reorientation has been observed with low-T$_g$ methacrylates.[19] This might indicate that molecular reordering in PMMA did not occur due to the restricted chain mobility below T$_g$.

While the surface structure of PMMA was not altered by compression, restructuring of the PBMA surface was complete and irreversible after the retraction of

the sapphire prism. The relatively high $T_g$ of PMMA implies a relatively rigid polymer structure. Therefore, the PMMA spectrum was not affected by the application and removal of the contact pressure. Also, the ester methyl group is slightly less hydrophobic than the ester butyl group.[19] Therefore, the driving force for the PMMA ester methyl group to tilt away from the hydrophilic sapphire surface to reduce the surface free energy is weaker than that of the methyl group of the ester butyl chain in PBMA. Hence, while compression by the sapphire caused the PBMA surface to restructure, the effect on the surface molecular structure of PMMA was negligible.

Fig. 3-5 shows a comparison between the SFG spectra (obtained with *ssp* polarization combination) of the interface of PMMA cast on sapphire and the contact interface of PMMA cast on fused quartz and the compressing sapphire prism (i.e., undeformed and deformed PMMA/sapphire interfaces, respectively). Since the PMMA deposited on the sapphire prism was annealed after spin casting, the SFG spectrum of the undeformed PMMA/sapphire interface is indicative of the conformation chemical equilibrium of PMMA on the hydrophilic sapphire surface. Ester methyl stretches are typically assigned to the feature at 2955 cm$^{-1}$ as symmetric, and the two low-intensity modes at 2990 and 3015 cm$^{-1}$ are typically attributed to asymmetric stretches of these groups. Although both spectra reveal the dominance of the symmetric ester methyl stretch, the deformed PMMA exhibits a different spectrum. However, a closer examination of the changes in this spectrum requires deconvolution of the methyl and *a*-methyl contributions.
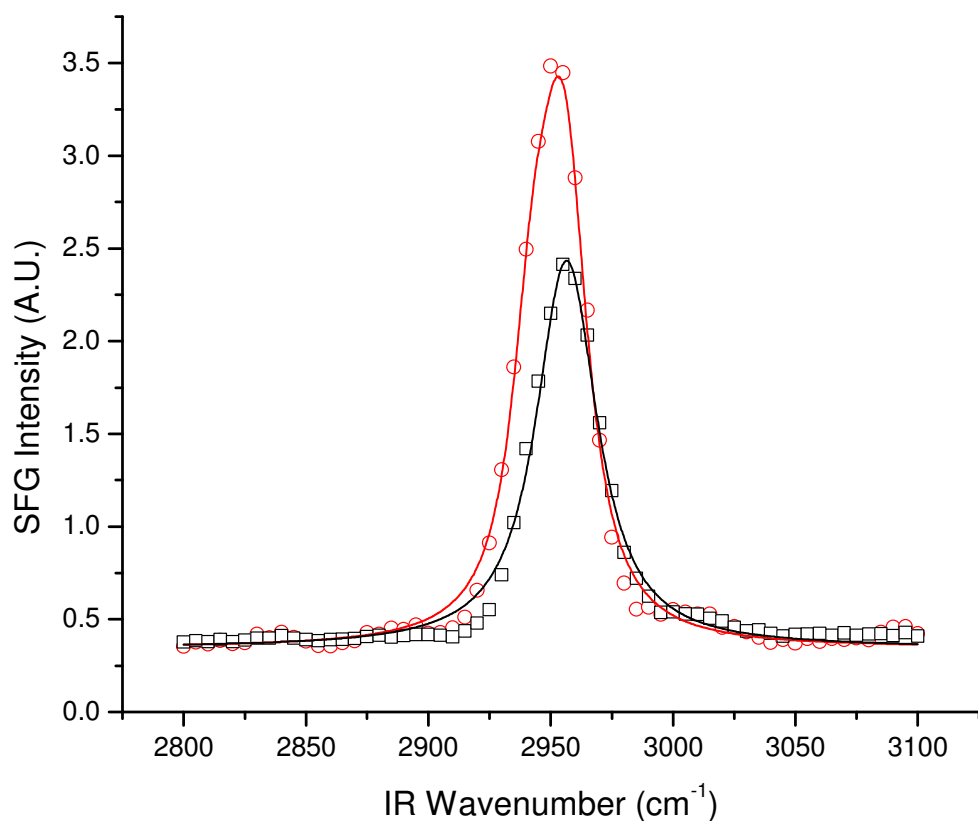
**Figure 3-5:** SFG spectra of deformed (□) and undeformed (○) PMMA/sapphire interfaces for *ssp* polarization combination.

The SFG spectra of d3-PMMA/sapphire interfaces shown in Fig. 3-6 provide a means of distinguishing contributions from the □-methyl group. In general, the peak at 2930 cm$^{-1}$ is attributed to symmetric $CH_3(s)$ stretches and the peaks at 2958 and 3000 cm$^{-1}$ to asymmetric $CH_3(a)$ stretches of the □-methyl, respectively. The results indicate that contact with the sapphire surface promotes ordering of the □-$CH_3$ groups, which explains the changes observed in the spectrum of the deformed PMMA shown in Fig. 3-5.
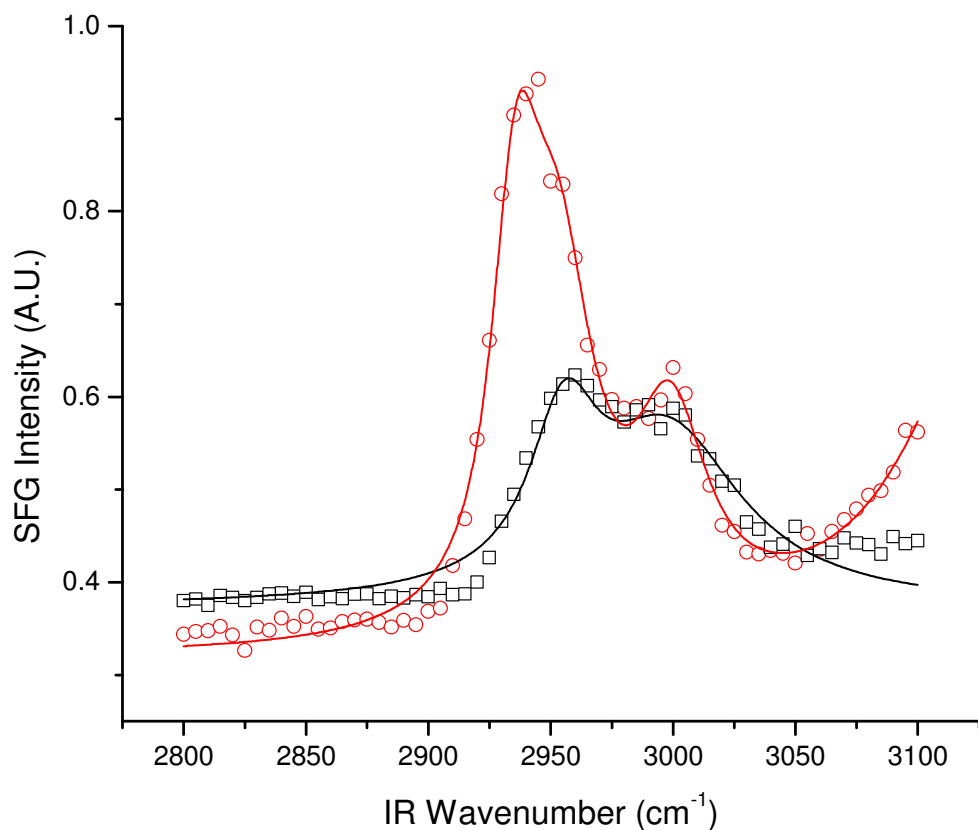
**Figure 3-6:** SFG spectra of deformed (□) and undeformed (○) d3-PMMA/sapphire interfaces for *ssp* polarization combination.

Thus, the molecular structure at the PMMA/sapphire interface assumes a new conformation chemical equilibrium due to the effect of the sapphire surface. The intensity of the ester methyl at 2955 cm$^{-1}$ [CH$_3$(s)] in the spectrum of the deformed polymer is less than what is expected. This is probably due to disordering of the ester methyl group since the interaction of the electron deficient acyl carbon would cause tilting of the methyl group to interact with the oxide surface.[26] The fact that the CH$_3$(s) stretch in the *ssp* spectra of PMMA shown in Fig. 3-6 is significantly more dominant than the CH$_3$(a)

stretch suggests that the ester methyl units contributing to the SFG signal are to some extent oriented perpendicular to the surface.

The SFG spectrum of the undeformed PBMA/sapphire interface (i.e., PBMA spin cast directly onto sapphire) was found to be identical to the spectrum of the deformed PBMA/sapphire interface (i.e., PBMA spin cast on fused quartz). In addition, SFG results (not shown here for brevity) did not reveal any discernible structural changes at the undeformed PBMA/sapphire interface (i.e., for PBMA in conformation chemical equilibrium at the sapphire surface) relative to the deformed PBMA/sapphire interface. This implies that the conformation chemical equilibrium at the PBMA surface was not affected by the mechanical work dissipated due to compression.

The possibility of chemical reactions at the sapphire surface during annealing cannot be precluded. The formation of a side-chain carboxylate ion that bonded with the sapphire surface is plausible. Hydrolytic cleavage of the ester methyl produces favorable interactions with the oxide surface.[27] A peak at ~1670 cm$^{-1}$ has been identified in the IR spectrum of the undeformed PMMA/sapphire interface, and has been associated with an aluminum oxide-stabilized carbonate (the peak corresponding to the ester carbonyl is usually found at ~1740 cm$^{-1}$).[28] A similar shift was observed in the SFG experiments of this study, and work is in progress to determine the orientation of these proposed carboxylate structures.

**Sensitivity and peak assignment in SFG spectra of polymer/sapphire interfaces**. The relatively strong SFG signal obtained with each polymer is mainly due to the visible-beam Fresnel factor enhancement at the buried interface. The results demonstrate significant molecular reordering at polymer/sapphire interfaces. The

differences in the SFG spectral features and intensities of the various polymer/sapphire interfaces can be attributed to differences in molecular orientation. The SFG signal from the interface was enhanced by careful selection of the incident angle and refractive index of the substrate. Since the refractive index of most methacrylate polymers is close to that of fused quartz and less than that of sapphire (i.e., 1.46-1.49 for polymers and fused quartz and ~1.77 for sapphire at 532 nm), sensitivity inherent to different geometries and substrates can be achieved. Regarding the polymer/sapphire interface, Fresnel enhancement due to TIR of the green light and attenuation of the IR through the polymer film thickness produced SFG signals almost exclusively from the buried interface. The identical SFG signals of thick (>1 mm) and thin (<300 nm) polymer films provided conformation for the latter. In reference to the polymer/air interface, a thinner film inhibits attenuation and the Fresnel enhancement by the free surface intensifies the signal from the interface relative to the fused quartz/polymer interface. This was demonstrated by the signal disappearance in the case of very thick films.

To examine the variation of the molecular conformation at the polymer interfaces in terms of the changes in the corresponding SFG spectra, it is essential to recognize the origin of the dominant modes. Although it appears from these spectra that portions of the side chains are ordered at the interface, identification of the overall configuration of $CH_3$ units at the PMMA surface from the SFG spectrum is perplexed by possible mode shifting and assignment errors. In view of the large number of possible modes at ~2950 $cm^{-1}$, closer examination of the assignments in the vicinity of this wavenumber is necessary. This was accomplished by performing comparative SFG studies with PMA

and d3-PMMA. Physically removing or deuterating the CH content (i.e., PMA and d3-PMMA, respectively) enabled a more detailed SFG analysis to be performed.

Fig. 3-7 shows a comparison of SFG spectra obtained in *ppp* polarization of different undeformed polymer/sapphire interfaces. The *ppp* polarization combination was used because it can reveal more peaks. It is reasonable to assume that the chemical nature of PMA and d3-PMMA is similar to that of PMMA. Both the ester methyl and the □-methyl modes are expected to contribute to the intensity of the feature at ~2990 cm$^{-1}$. Although an additional peak at 3015 cm$^{-1}$ is commonly assigned to the ester methyl asymmetric [CH$_3$(a)] mode, the intensity of this mode should be similar to that of the 2990 cm$^{-1}$ peak, which is small. Therefore, the broad feature in the PMMA spectrum in the vicinity of 2990 cm$^{-1}$ is mainly due to the additional ordering of the □-methyl mode observed in the d3-PMMA spectrum. The deuterated ester methyl stretch was measured in the C-D region to confirm the ability to distinguish the ester methyl and □-methyl group intensities by deuteration. It should also be noted that the curve fit of the SFG data did not neglect hydroxyl peaks. Even though these peaks were found outside the range examined, ignoring them can lead to poor fitting in *ppp* polarization. These hydroxyl peaks are similar to those reported in another study.[29]
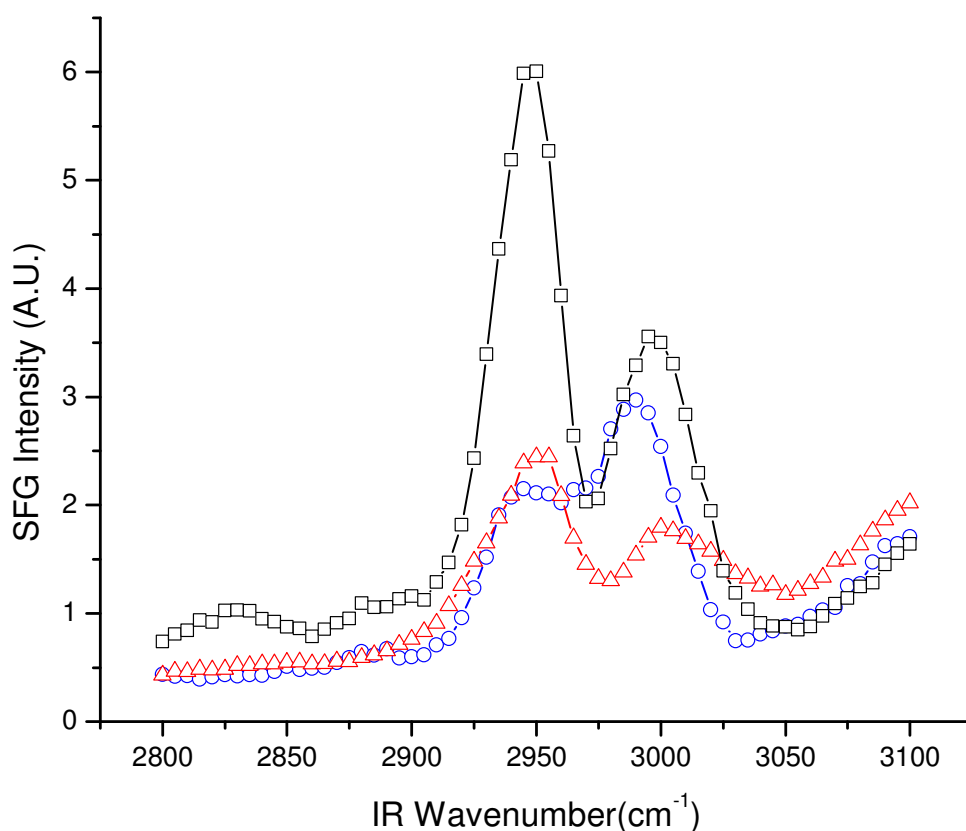
**Figure 3-7:** SFG spectra of undeformed PMMA/sapphire (□), d3-PMMA/sapphire (○), and PMA/sapphire (Δ) interfaces for *ppp* polarization combination.

The main feature in the PMMA spectra shown in Fig. 5 is a convolution of the symmetric □-methyl and ester methyl moieties. Both functional groups also produce an SFG asymmetric mode at 2990 cm$^{-1}$. Therefore, to determine the contributions of the ester methyl and □-methyl modes in the overall spectra, it is necessary to account for the origins of overlapping C-H intensities. The SFG spectra of PMMA, d3-PMMA, and PMA deposited on sapphire using the same spin cast and anneal procedures as for the polymers deposited on fused quartz demonstrate that the intensities from the respective

methyl and *a*-methyl groups can be distinguished by deuterating or eliminating the source of the signal without altering the chemical characteristics. This separation of the SFG intensity sources also enables the observation of the low-intensity CH$_3$(a), *a*-CH$_3$(s), and *a*-CH$_3$(a) modes. Otherwise, the ester methyl symmetric stretch CH$_3$(s) is overshadowed by the $\square$-methyl symmetric stretch $\square$-CH$_3$(s) in the spectrum of the deformed (compressed) PMMA/sapphire interface.

## 3.4 Conclusion

Infrared-visible SFG vibrational spectroscopy studies were performed to examine in situ the changes in the surface molecular structures of PBMA and PMMA deposited on fused quartz substrates due to compression by a smooth sapphire prism, using the spectra of the polymer surfaces exposed to ambient air as a reference. Because of the markedly different glass transition temperatures, the deformed PMMA and PBMA surfaces exhibited remarkably different molecular conformations at the interface with the sapphire prism. The SFG results demonstrated a negligible effect of compression on the conformation chemical equilibrium of PMMA at the sapphire surface. However, significant molecular reordering was observed at the surface of the PBMA compressed by the sapphire prism. This structure change is attributed to the relatively unrestricted molecular movement in the low-T$_g$ PBMA, which promoted molecular rearrangement toward a thermodynamically stable molecular confirmation and chemical interactions due to sapphire functionalities. By using PMA and d3-PMMA, the origins of intense vibrational resonances of similar energy were distinguished in the same frequency range, thus enabling the identification of low-intensity contributions from *a*-methyl groups,

which are otherwise overshadowed by the methyl side chains. The results of this study demonstrate that infrared-visible SFG vibrational spectroscopy is an effective technique for examining in situ polymer surface restructuring at buried interfaces due to chemical and mechanical effects.

# References

[1]*Polymer Surfaces and Interfaces II*; Feast, W. J.; Munro, H. S.; Richards, R. W.; Eds., Wiley: New York, **1992**.

[2]Garbassi, F.; Morra, M.; Occhiello, E.; *Polymer Surfaces, From Physics to Technology*; Wiley: New York, **1994**.

[3]Bhushan, B.; Israelachvili, J. N.; Ladman, U.; *Nature* **1995**, *374*, 607.

[4]Salmeron, M.; *Tribol. Lett.* **2001**, *10*, 69.

[5]Opdahl, A.; Hoffer, S.; Mailhot, B.; Somorjai, G. A.; *Chem. Rec.* **2001**, *1*, 101.

[6] Wang, J.; Paszti, Z.; Even, M. A.; Chen, Z.; *J. Am. Chem. Soc.* **2002**, *124*, 7016.

[7]Gautam, K. S.; Dhinojwala, A.; *Phys. Rev. Lett.* **2002**, *88*, 145501.

[8]Schwab, A. D.; Dhinojwala, A.; *Phys. Rev. E* **2003**, *67*, 021802.

[9]Du, Q.; Xiao, X. D.; Charych, D.; Wolf, F.; Frantz, P.; Shen, Y. R.; *Phys. Rev. B* **1995**, *51*, 7456.

[10]Amitay-Sadovsky, E.; Komvopoulos, K.; Ward, R.; Somorjai, G. A.; *J. Phys. Chem. B* **2003**, *107*, 6377.

[11]Hatch, S. R.; Polizzotti, R. S.; Dougal, S.; Rabinowitz, P.; *J. Vac. Sci. Technol. A* **1993**, *11*, 2232.

[12]Conboy, J. C.; Daschbach, J. L.; Richmond, G. L.; *J. Phys. Chem.* **1994,** *98,* 9688.

[13]Gautam, K. S.; Schwab, A. D.; Dhinojwala, A.; Zhang, D.; Dougal, S. M.; Yeganeh, M. S.; *Phys. Rev. Lett*. **2000**, *85*, 3854.

[14] Wang, J.; Chen, C.; Buck, S.M.; Chen*, Z. J. Phys. Chem. B*, **2001**, *105*, 12118.

[15] Zhang, D.; Dougal, S.M.; Yeganeh, M.S. *Langmuir*, **2000**, *16*, 4528.

[16] Gautam, K.S., Schwab, A.D.; Dhinojwala, A.; Zhang, D.; Dougal, S.M.; Yeganeh, M.S. *Phys. Rev. Lett*., **2000**, *85*, 3854.

[17] Briggman, K.A.; Stephenson, J.C.; Wallace, W.E.; Richter, L.J. *J. Phys.Chem. B*, **2001**, *105*, 2785.

[18] Oh-e, M.; Hong, S.C.; Shen, Y.R. *Appl. Phys. Lett*., **2002**, *80*, 784.

[19] Mansfield, K.F.; Theodorou, D.N. *Macromolecules* **1990**, *23*, 4430.

[20]Brown, M. G.; Raymond, E. A.; Allen, H. C.; Scatena, L. F.; Richmond, G. L.; *J. Phys. Chem. A* **2000**, *104*, 10220.

[21]Yeganeh, M. S.; Dougal, S. M.; Pink, H. S.; *Phys. Rev. Lett.* **1999**, *83*, 1179.

[22]Wang, J.; Chen, C. Y.; Buck, S. M.; Chen, Z.; *J. Phys. Chem. B* **2001**, *105*, 12118.

[23]Schneider, B.; Stokr, J.; Schmidt, P.; Mihailov, M.; Dirlikov, S.; Peeva, N.; *Polymer* **1979**, *20*, 705.

[24]Wang, J.; Woodcock, S. E.; Buck, S. M.; Chen, C. Y.; Chen, Z.; *J. Am. Chem. Soc.* **2001**, *123*, 9470.

[25]Chen, C. Y.; Loch, C. L.; Wang, J.; Chen, Z.; *J. Phys. Chem. B* **2003**, *107*, 10440.

[26]Miyamae, T.; Nozoye, H.; *Surf. Sci*. **2003**, *532*, 1045.

[27]Grohens, Y.; Brogly, M.; Labbe, C.; Schultz, J.; *Eur. Poly. J.* **1997**, *33*, 691.

[28]Konstadinidis, K.; Thakkar, B. Chakraborty, A.; Potts, L. W.; *Langmuir* **1992**, *8*, 1307.

[29]Rao, A.; Rangwalla., H; Varshney., V; Dhinojwala, A.; *Langmuir* **2004**, *20*, 7183.

# Chapter 4

# Surface segregation of atactic poly(propylene) and aspecific poly(ethylene-co-propylene) copolymers at air/polymer and polymer/solid interfaces

## 4.1 Introduction

With very few exceptions, surface enrichment or wetting can be predicted based on the surface free energy of individual blend components. Changes in bonding at an interface that are more favorable for one component than another[1,2,3,4,5] due to a corresponding lower surface free energy will be attributed to the enthalpic factor. When the surface energies are similar (i.e., negligible enthalpic factor) other subtle properties may lead to surface segregation. The preferential segregation to the surface of the shorter and less stiff component of a polymer due to its greater flexibility and ability to rearrange is attributed to the entropic factor. The extent that entropy controls the surface configuration is less understood. Theoretical results suggest that conformational entropy, related to the size of the random coil, and packing entropy related to the configuration of

the polymer at the interface play competing roles in mixtures of branched polyolefins at the air interface. Side branches have been found to be a key variable in determining the surface activity of polyolefins. Recent theoretical studies have demonstrated that limitations on the flexibility and free space of the polymer chains approaching the surface are responsible for the loss of entropy.[6] Therefore, the concentration depth profile may depend on the volume determined by the radius of gyration of each polymer component. Deviations from the anticipated behavior based on enthalpic driving forces have sparked experimental studies of model systems, such as isotopic mixtures and architecturally asymmetric blends, i.e., polymers with the same chemical composition but different branching ratios.[2,3]

Experimental results supporting theoretical predictions that miscible polyolefin blend segregation can be measured at both high-energy and low-energy interfaces due to entropically mediated enrichment were obtained in the present study. It is shown that such a system of polymers is a polyolefin blend of atactic polypropylene (*a*PP) and aspecific poly(ethylene-co-propylene) rubber (*a*EPR) in which the entropic factor dominates the surface composition because of the absence of an overriding enthalpic driving force. It was found that annealing provides the driving force for the shorter and more flexible polymer chains to segregate preferentially to the interfaces of the polymer with a solid sapphire surface and the polymer free surface. The polyolefins are saturated hydrocarbon chains of similar surface energies and same molecular weight (~54000), which provide suitable media for investigating subtle mechanisms of surface and bulk thermodynamic interactions. Architecturally asymmetric components are ideal systems

68

for studying these effects because the chemical characteristics of the monomer components, such as density and intermolecular forces, are nearly identical.

The surface and bulk phase behavior of polyolefin copolymers and blends has received considerable attention in recent years in large part because of their continued commercial importance. Polyolefin synthesis also enables the careful control of architectural variables, such as short-chain branching and tacticity, with similar hydrophobic units. This control has lead to the use of polyolefins as model systems for studying the underlying molecular phenomena governing the fundamental properties of polymers including surface segregation and bulk phase behavior. At the molecular level, many polyolefins assume specific conformations at the air interface.[7,8,9] In particular, the aspecific poly(ethylene-co-propylene) copolymers (*a*EPR) were shown to configure in a way that preferentially orients methyl side branches upright at the air/polymer interface.[13] These specific types of molecular interactions at the air/polymer interface may also affect the surface segregation properties for polyolefin blends at the air and buried surfaces.

These model blends mimic the important commercial blend of isotactic PP/EPR, without complications due to crystallinity, through the use of an aspecific polymerization catalyst. SFG and XPS are both surface sensitive techniques and can distinguish between the $CH_3$ unit in propylene and the $CH_2$ unit, which is present in both the ethylene and propylene repeat units.[10] Additionally, SFG and XPS, applied to *a*PP/*a*EPR blends, do not require isotopic labeling, and because SFG is a photon-based technique and XPS is an electron-based technique, each technique is sensitive to a different depth of the surface and gives a different type of chemical information.

SFG is specifically sensitive to the molecular composition and orientation of the surface monolayer. The surface sensitivity of XPS is limited by the mean-free-path of photoelectrons generated in the polymer, typically a few nanometers, and can be controlled to some extent by varying the detection angle with respect to the surface plane. Thus, SFG can be used to determine the composition of the surface monolayer, and XPS can be used to integrate the chemical composition of the top few nanometers of the surface. Since blend segregation can drive enrichment on a length scale close to or smaller than the radius of gyration of the polymer, these measurements are only possible because of the high surface sensitivity of sum frequency generation (SFG) vibrational spectroscopy. Because SFG spectroscopy is a surface specific technique with monolayer sensitivity, it is ideal for studying molecular composition and conformation at both free surfaces and buried interfaces.[11,12,13] Nonlinear optical characterization of the interface provides the necessary resolution to detect enrichment on the order of a monolayer and to quantify the conformational ordering needed to determine the driving forces of segregation. The objectives of this study were to examine the enrichment of free and buried interfaces by a component of a miscible polyolefin blend, explain the phenomena associated with the conformation of a polymer chain backbone at the interface, and provide insight into the entropic factors affecting the surface composition and structure in light of SFG vibrational spectroscopy results.

## 4.2 Experimental Procedures

SFG, XPS, and differential scanning calorimetry (DSC) were used to examine the interface molecular structure, the chemical morphology of the surface region, and the

bulk phase behavior of miscible blends of atactic polypropylene (aPP) with aspecific

poly(ethylene-co-propylene) rubber (aEPR). Each of the blend components has the basic

structure given in Fig. 4-1 and is comprised of similar $CH_2$ and $CH_3$ units. Blend

miscibility was achieved by varying the molecular weight of the components.
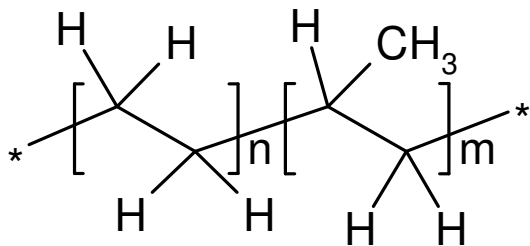


**Figure 4-1:** Structure of aspecific poly(ethylene-co-propylene) rubber (aEPR). The

distribution of block lengths (n,m) is very nearly random and methyl group placement in

the propylene units lack stereospecificity

**Polymers**. The molecular structure and composition of the surfaces of aPP, aEPR

(consisting of 42 mol% ethylene), and aPP/aEPR bulk miscible blend were investigated

by SFG vibrational spectroscopy to identify the molecular chain conformation changes

after annealing. Fig. 4-1 shows the structures of aPP and aEPR, which have a molecular

weight of ~54000. The corresponding copolymer block lengths n and m are nearly

random, and the methyl (CH$_3$) group in the propylene units does not exhibit any

stereospecificity, as shown by nuclear magnetic resonance spectroscopy. Since the

copolymers are random in nature, it was assumed that the blocks did not play an

important role in the segregation behavior. Solutions containing 5 wt% of the polymers

were prepared in deuterated d-14 n-hexane and were allowed to equilibrate for at least 2

71

days. The primary components consisted of *a*PP and *a*EPR. The *a*PP/*a*EPR blend was prepared by mixing 50:50 wt% of these polymers and allowing them to equilibrate for an additional 2 days. The polymer miscibility is reflected by the single glass transition temperature, determined from differential scanning calorimetry measurements, i.e., 0˚C (*a*PP), -46˚C (*a*EPR), and -30˚C (*a*PP/*a*EPR), even for the ~50:50 wt% blend composition that shows the strongest tendency for separation.[14]

**Samples**. Polymer films were prepared by spin-casting solutions onto equilateral sapphire prisms of synthetic single-crystal $Al_2O_3$ (polished to a root-mean-square roughness of 5-10 nm) with the optical ĉ-axis perpendicular to the free surface (Redoptronics, Mountain View, CA). After nitric and sulfuric acid treatment, the prisms were cleaned in UV-initiated ozone for at least 1 h. The sapphire prisms were used immediately after cleaning to minimize airborne contamination. Some of the as-cast specimens were examined with the SFG within 2 h of fabrication, whereas other specimens were annealed at 70˚C for 8 h and allowed to cool in ambient air. Film thickness measurements obtained with an atomic force microscope (Park Scientific Instruments, Sunnyvale, CA) showed that the thickness of the produced films was between 200 and 300 nm. All the SFG measurements were obtained at room temperature using total internal reflection geometry for the buried sapphire/polymer interfaces and external reflection geometry for the air/polymer interfaces.

**Differential Scanning Calorimetry (DSC)**. Baseline subtracted DSC scans were performed from $-110^oC$ to $120^oC$ at $20^oC$/min in a Perkin-Elmer DSC-7 calorimeter with liquid nitrogen cooling and helium purge using 15mg samples. Experiments applied a melt cycle by heating ($20^oC$/min) the films to 200 $^oC$ for 2min, quenching ($320^oC$/min) to

-110$^{\circ}$C for 10min, and reheating (20$^{\circ}$C/min). The films were annealed at various temperatures by sealing the samples in DSC pans and placing the pans in sealed vials and annealing in a thermostatted oil bath for 16 hours at temperatures ranging from 50-150$^{\circ}$C.

**Spectroscopy Analysis.** SFG vibrational spectroscopy is ideal for studying the composition and conformational behavior of interfaces. SFG spectra were obtained with Nd:YAG laser (Leopard, Continuum, Santa Clara, CA). In the present system, the tunable infrared (IR) beam is combined with the 532 nm radiation at the sample interface at corresponding incident angles of 60° and 65° with respect to the surface normal. A significant enhancement of the SFG signal is obtained with Raman and IR active vibrational modes generated when centrosymmetry is broken. SFG spectra were collected using the *ssp* polarization combination, which probes components of the nonlinear susceptibility tensor. In addition, SFG experiments were performed with other polarization combinations to ensure the peak assignments.[15] The *ssp* polarization is more sensitive to symmetric vibrational modes normal to the interfacial plane, and the signal is larger for this procedure. A detailed description of the laser system used in this study can be found elsewhere.[16]

**X-Ray photoelectron Spectroscopy (XPS).** XPS experiments were performed on a Perkin-Elmer PHI 5300 XPS spectrometer with a position sensitive detector and a hemispherical electron energy analyzer. The Mg K$\square$ x-ray emission (1253.6eV) was used as the probe and was generated with 400W (15 kV acceleration voltage) at the Mg cathode. A pass energy of 178eV was used for survey spectra with a 45 degree takeoff angle and a pass energy of 35eV was used for spectra of the valence band region at a 45 degree takeoff angle. The sampling depth of the XPS experiments is based on an

attenuation length of 2.9±0.4nm measured by Roberts et al. for photoelectrons ejected from PMMA having a kinetic energy of 1200eV.[17] Using this value as an approximation for the attenuation length of valence band photoelectrons generated by the K☐ x-ray source (kinetic energy of photoelectrons ~1240eV) leads to a 95% sampling depth of 6.1±0.8nm.[18]

## 4.3 Bulk Phase Behavior of aPP/aEPR Blends (DSC)

Fig. 4-2 shows DSC scans of films of *a*PP, and *a*EPR, and a 50:50 weight percent *a*PP/*a*EPR blend of the two components cast from hexane. Fig. 4-2 demonstrates that the 50:50 blend has a single glass transition temperature ($T_g$) at –30°C, intermediate between the individual *a*PP ($T_g$=0°C ) and *a*EPR ($T_g$=–46°C ) components. The width of the transition region is greater in the blend than the individual components. This behavior is typical of a miscible blend and indicates that blends of *a*PP and *a*EPR are in a single miscible phase. The *a*PP and *a*EPR components will be in a single phase at room temperature for all blend compositions. The 50:50 weight percent blends are very near the critical composition, which will have the strongest tendency for phase separation.
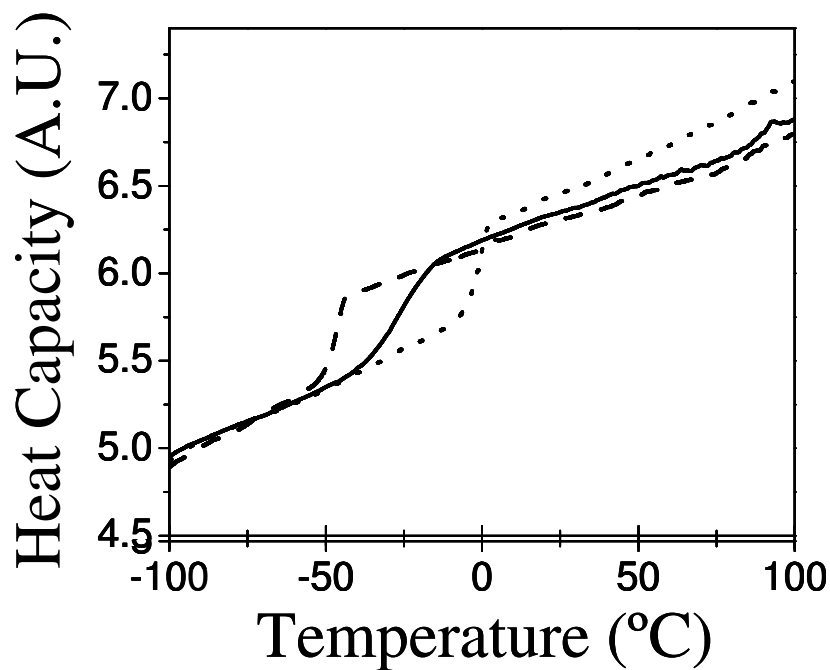
**Figure 4-2:** DSC scans ($20^\circ$C/min) of individual components and blends: (a) *a*PP (dotted); *a*EPR (dashed); and 50:50 wt. percent *a*PP1/*a*EPR blend (solid).

## 4.4 Surface Monolayer Composition of aPP/aEPR Blends (SFG)

The analysis of the SFG vibrational spectra of sapphire/polymer and air/polymer interfaces obtained in *ssp* polarization combination was based on published data. According to the literature,[19,20] the symmetric and two Fermi resonances (FR) of methylene stretches [$CH_2$(s) and two $CH_2$(FR)] resonate at 2855, 2920, and 2955 cm$^{-1}$, respectively, while the symmetric and asymmetric methyl stretches [$CH_3$(s) and $CH_3$(a)] resonate at 2880 and 2955 cm$^{-1}$, respectively. A small feature can also be observed at 2940 cm$^{-1}$, which is associated with the Fermi resonance between the $CH_3$(s) mode and an overtone of the $CH_3$ bending mode [$CH_3$(FR)].

Fig. 4-3 shows a comparison of the sapphire/polymer SFG spectra of the annealed

$a$PP, $a$EPR, and $a$PP/$a$EPR. The spectrum of the sapphire/$a$PP interface contains only the

$CH_2(s)$ and $CH_3(a)$ peaks. The high intensity of the $CH_2(s)$ peak in the *ssp* polarization

spectrum, which originates from the main chain, indicates that the backbone segments of

$a$PP lay flat against the sapphire surface, whereas the high intensity of the $CH_3(a)$ peak

(more than twice the intensity in *ppp* polarization combination) suggests that the methyl

groups of $a$PP exhibit preferential tilting away from the surface normal. This result is in

agreement with the tendency of the $CH_3$ and bulky hydrophobic side chains (extending

outward from the surface into the air) to diminish at the hydrophilic sapphire interface.[21]

The SFG spectrum of the sapphire/$a$EPR interface shows that the intensity of the $CH_2(s)$

signal is significantly less than that observed for $a$PP. This implies relatively less

ordering of the backbone segments of $a$EPR at the solid interface or the existence of

longer-sequence trans oriented backbone segments whose inversion center caused the

SFG intensity to decrease significantly. Thermal annealing for longer time did not

produce additional spectral changes. The similarity of the $a$PP and $a$PP/$a$EPR spectra

suggests that the $a$PP chains dominated the molecular ordering at the interface. Thus,

segregation at the blend/sapphire interface is distinguished by the methyl groups of the

$a$PP component, which are tilting away from the normal to the surface, whereas the

backbone segments of $a$PP lay flat against the sapphire surface, despite the similar

surface energies and molecular weights of $a$PP and $a$EPR.
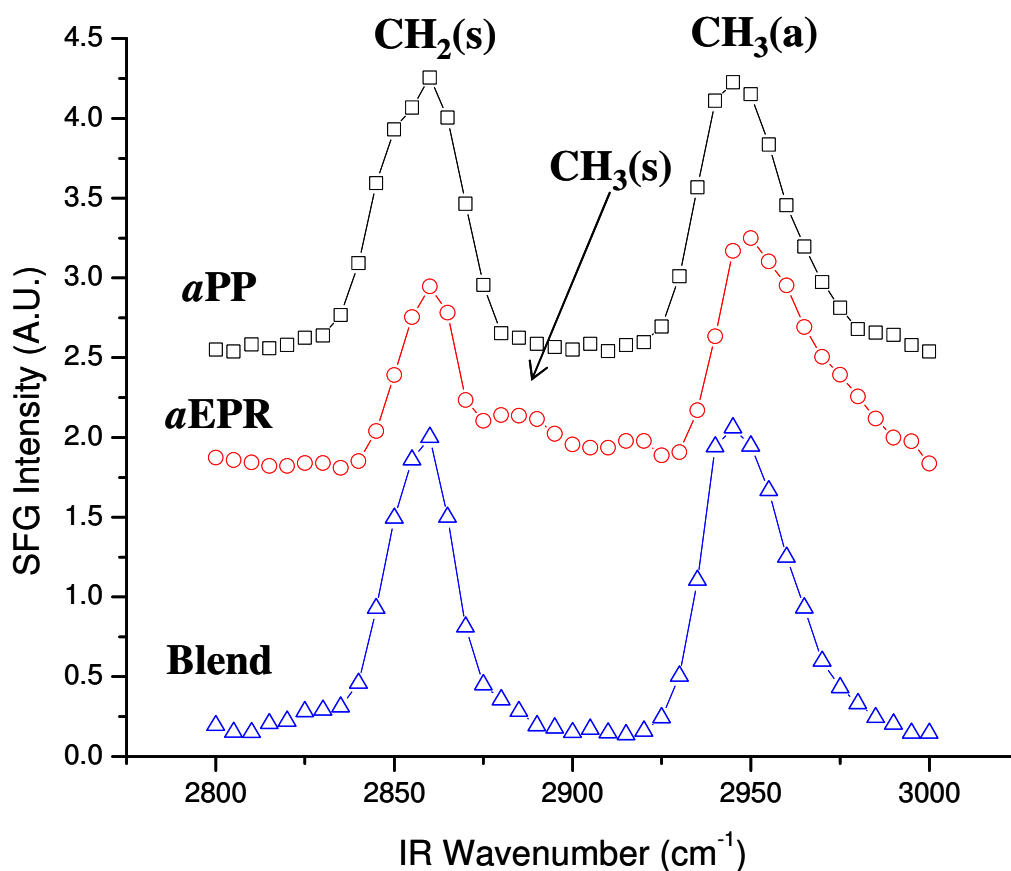
**Figure 4-3:** SFG spectra (collected in *ssp* polarization combination) of sapphire/polymer (annealed) interfaces: *a*PP (□), *a*EPR (○), and (50:50 wt%) *a*PP/*a*EPR (Δ).

Fig. 4-4 shows SFG spectra of the air/polymer interfaces of the annealed *a*PP, *a*EPR, and *a*PP/*a*EPR. A comparison with the spectra of the sapphire/polymer interfaces (Figure 2) shows significant differences in the orientation of the methyl and methylene groups. The dominance of the $CH_3(s)$ peak indicates that both *a*PP and *a*EPR tend to preferentially orient their pendent methyl groups away from the surface. Previous polarization experiments support this claim.[22] The tendency of the hydrophobic side

chains to extend outward into the air has been observed with various polymer surfaces.[23] The close similarity of the *a*PP/*a*EPR and *a*PP spectra suggests that the molecular chains of the *a*PP blend component are dominant in the molecular composition at the blend surface. Conversely to the sapphire interface, all the *ssp* spectra of the polymer surfaces show a strong signal from the $CH_3(FR)$ peak and a small peak at 2955 $cm^{-1}$, which is primarily due to the $CH_3(a)$ peak and may include a small contribution by the $CH_2(FR)$ peak.
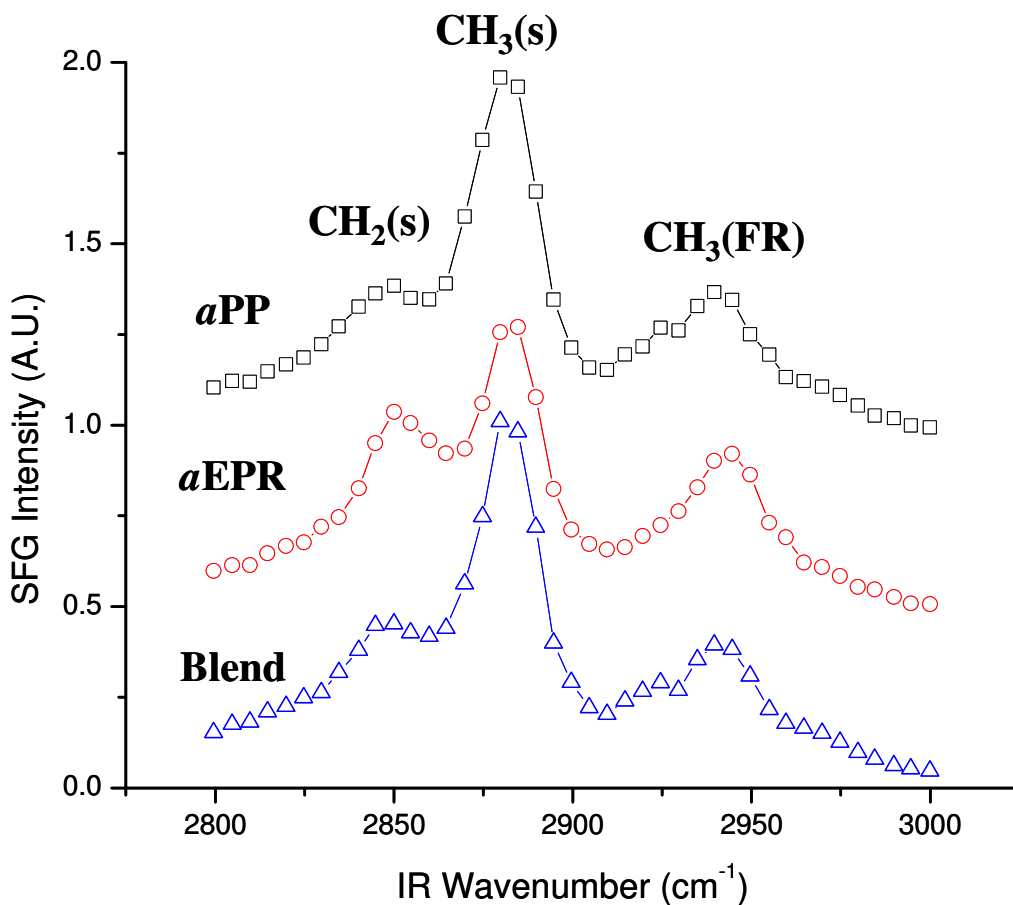


**Figure 4-4:** SFG spectra (collected in *ssp* polarization combination) of air/polymer (annealed) interfaces: *a*PP (□), *a*EPR (○), and (50:50 wt%) *a*PP/*a*EPR (△).

The fact that the intensities of the $CH_2(s)$ and $CH_3(s)$ features in the spectra of the $a$PP/$a$EPR blend are identical to those of the $a$PP component for both the sapphire/polymer and the air/polymer interfaces indicates the preferential segregation of the $a$PP chains to the surface. This result was confirmed by additional experiments performed with other polarization combinations. The $CH_2(s)/CH_3(s)$ mode strength ratio of $a$PP/$a$EPR is indistinguishable (within the experimental uncertainty) from that of $a$PP, illustrative of a large surface excess of the $a$PP chains. These findings suggest that the $a$PP chains segregated both at the air/polymer and the sapphire/polymer interfaces. Since the polymer chain with the higher branching ratio ($a$PP) encounters less favorable interactions in the bulk, it is easier for its backbone to lay flat against the solid surface ($a$PP occupies less surface free volume). Therefore, it may be inferred that chain flexibility was the main reason for the observed preferential surface segregation of $a$PP. These results are in accord with those of segregation studies dealing with diblock copolymers, as evidenced from neutron reflection measurements.[24] The present study is the first to show that the predicted entropy factors mediate the enrichment in miscible blends.

To examine the effect of annealing on the molecular ordering, SFG spectra in *ssp* polarization combination were obtained from buried interfaces of sapphire and as-cast polymers. Fig.4-5 shows that the SFG spectra of the as-cast $a$PP and $a$EPR exhibit an overall intensity that is ~20-30% of the annealed polymer spectra (Figure 2) due to less ordering. The data contain similar features (with a small contribution from other $CH_2(a)$ groups at ~2900 cm$^{-1}$); however, significant differences exist in the peak intensities. It

has been found that the $CH_2/CH_3$ ratio of the fitted mode amplitudes varies linearly with the $CH_2/CH_3$ content ratio in the bulk.[4] Fig. 4-5 shows that the ratio of the fitted mode strengths $[CH_2(FR)/CH_3(a)]$ reflects the ethylene/propylene content ratio in the as-cast polymer bulk compositions. Therefore, it can be concluded that spin casting did not result in any specific ordering or segregation of the components in the blend.
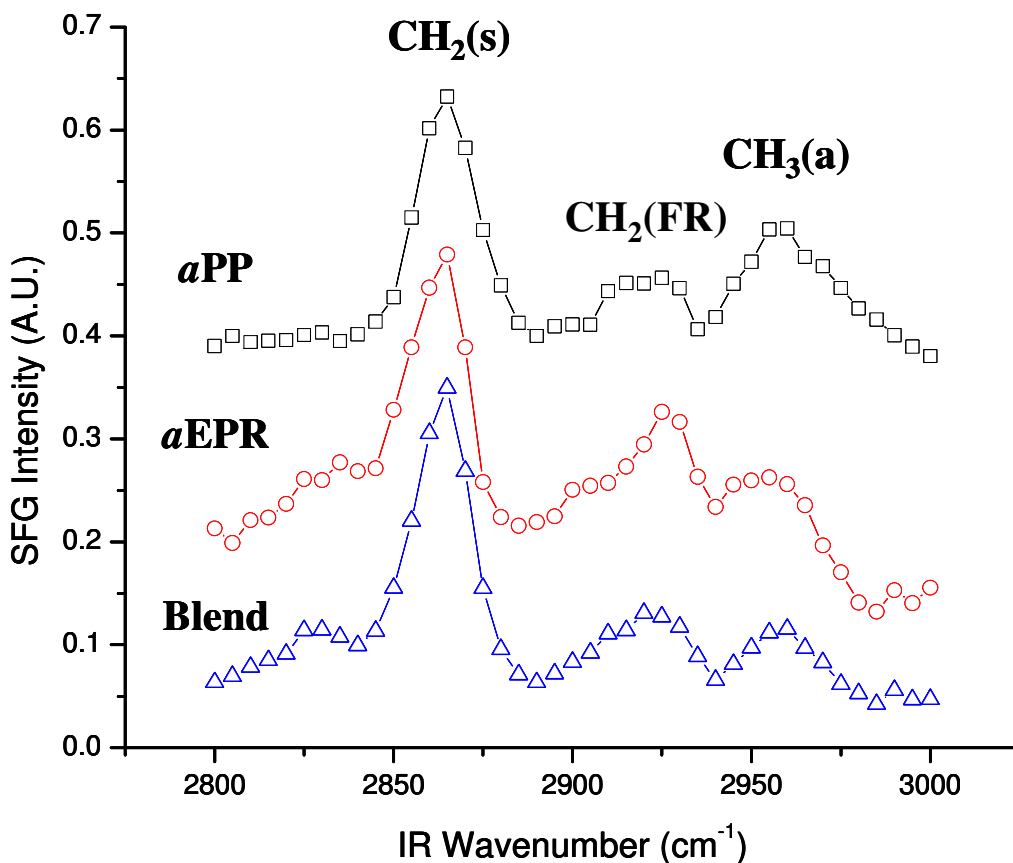


**Figure 4-5:** SFG spectra collected in *ssp* polarization of sapphire/(as-cast) polymer interfaces: *a*PP (□), *a*EPR (○), and (50:50 wt%) *a*PP/*a*EPR (Δ).

While small spectral changes were observed at the air/polymer interface after annealing, marked changes were measured for $a$PP and $a$EPR at the sapphire interface. Since the glass transition temperatures of $a$PP ($0ºC$) and $a$EPR ($-46ºC$) are well below the room temperature, the chains were sufficiently energetic to reach equilibrium conformation. Even though the chain movement should have been unconstrained, segregation did not occur without thermal annealing. This implies that the differences observed with the annealed polymers resulted from chain movement at a critical temperature much higher than the glass transition temperature.

It is important to note the differences in the molecular chain conformation at the air/polymer and sapphire/polymer interfaces demonstrated by the corresponding SFG spectra in Figs. 4-3 and 4-4, respectively. At the air/polymer interface, the methyl groups oriented outward, as evidenced from the dominance of the $CH_3(s)$ peak in *ssp* polarization combination. Since the principal features in Figure 5 are the $CH_2(s)$ stretches, it follows that the methylene groups were well ordered toward the solid interface while the methyl groups were more disordered. The SFG results of this study demonstrate the occurrence of preferential segregation of $a$PP (compared to $a$EPR) molecular chains to the free surface and the interface of the solid sapphire. Hence, it may be argued that surface organizational (entropic) interactions provided the necessary driving force for the enrichment. Moreover, the SFG spectra indicate that the number densities of the ordered methyl side chains (normal to the surface in air and tilted toward the surface at the buried interface) and backbone methylene groups of $a$PP are greater than those of $a$EPR, possibly enhancing the surface activity.

A central finding of the present study is that, in addition to the air/polymer interface, the more branched polymer (*a*PP) in the blend segregates to the buried sapphire/polymer interface. It is believed that the interface enrichment with *a*PP chains is driven by conformational entropy. The structure, density, and flexibility of the molecular chains affect entropy. Because the shorter and more branched component is generally more flexible, it is characterized by a smaller conformational parameter, e.g., statistical segment length $\beta^2 = R_g^2/V$, where $R_g$ is the unperturbed coil radius of gyration and $V$ is the chain volume. Differences in the statistical segment length affect the surface enrichment because the more flexible chains occupy a smaller volume at the surface. The enthalpic cohesive energy is another driving force that affects the interface enrichment. It has been reported that the more branched components of polyolefins exhibit lower cohesive energy.[25] This can be understood by considering that a flexible chain interacts mainly with itself rather than with neighboring chains. Therefore, surface segregation of the more flexible chains is favored thermodynamically. Consequently, it may be interpreted that entropic factors are responsible for the enrichment because van der Waals force interactions between the polymer chains and the solid sapphire surface weaken the driving force for *a*PP chain segregation at the buried interface. The SFG results suggest that surface segregation occurred because of entropic reasons, in agreement with theoretical predictions.[1]

## 4.5 Surface Composition of the Top 6-8 nm of aPP/aEPR Blends (XPS)

XPS was used to study the composition of the top $6.1 \pm 0.8$ nm of the films. XPS spectra of the carbon 1s core peak at 285 eV for *a*PP and *a*EPR were found to be virtually identical. The valence band spectra, however, showed significant differences. Both polymers exhibited peaks at 15 eV and at 21 eV that are assigned to the 2s bonding and antibonding orbitals from the -$CH_2$- backbone units of the polymers.[10] Both polymers showed an additional feature at 18 eV that is 2 overlapping peaks, assigned to the 2s bonding and antibonding orbitals of the pendant $CH_3$ group.

The XPS results indicated that the *a*PP enrichment, which is observable by SFG for this sample, is not detectable at the level of resolution of XPS. Since the depth that the XPS is integrating over is estimated at $6.1 \pm 0.8$ nm, this indicates that the *a*PP enrichment layer is very thin – the top 5-7 nm contains significant quantities of each of the two components. Considering the sampling depth and the signal-to-noise ratio effect on the measurement, it is likely that the highest levels of *a*PP in the surface enrichment layer were restricted to the top 2-3nm of the film. Fig. 4-6 shows schematically the envisioned enrichment at of the polymer film at the high-energy sapphire and low-energy air interfaces. Since SFG can detect such localized enrichment, as opposed to other less surface sensitive techniques such as X-ray photoelectron spectroscopy,[7] the figure depicts segregation less than 5 nm from the surface. Depth profiling experiments are necessary to confirm this view.
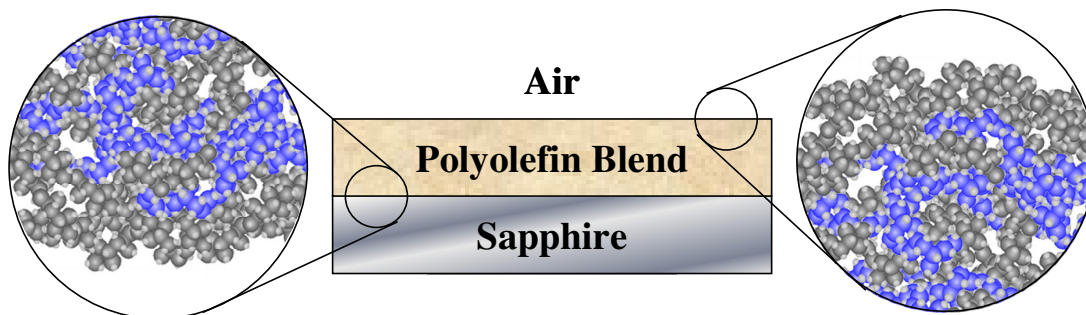
**Figure 4-6:** SFG spectra collected in *ssp* polarization of sapphire/(as-cast) polymer interfaces: *a*PP (□), *a*EPR (○), and (50:50 wt%) *a*PP/*a*EPR (Δ).

## 4.6 Conclusion

Segregation phenomena at buried (sapphire) interfaces and free (air) surfaces of miscible polyolefins (*a*PP, *a*EPR, and 50:50 wt% *a*PP/*a*EPR) were investigated by SFG vibrational spectroscopy in *ssp* polarization combination. Enrichment by the shorter and more flexible branched component (*a*PP) was found at the sapphire/polymer interface of the *a*PP/*a*EPR blend. In the absence of a significant chemical affinity for the sapphire interface, the enthalpic driving force for segregation of a miscible blend based on the minimization of the interfacial energy is small. Despite the insignificant differences in the surface energies of the *a*PP and *a*EPR components with respect to air and sapphire, preferential segregation of the *a*PP chains occurred as a result of chain conformation. The more branched polymer (*a*PP) produced a stronger overall SFG signal, indicating a greater chain ordering. SFG spectra revealed a preferred ordering and interface enrichment of the more flexible *a*PP chains possessing a smaller statistical segment length. Since the $CH_2/CH_3$ peak area ratio (XPS) for the blend sample fits nearly identically to the bulk peak area ratio, the *a*PP enrichment layer observable by SFG for

this sample is not detectable at the level of resolution of XPS, it is expected that the enrichment layer is very thin.

## References

[1] Donley, J. P.; Wu, D. T.; Fredrickson, G. H. *Macromolecules* **1997**, *30*, 2167.

[2] Jones, R. A.; Kramer, E. J.; Rafailovich, M. H.; Sokolov, J.; Schwarz, S. A. *Phys. Rev. Lett*. **1989**, *62*, 280.

[3] Tretinnikov, O. N. *Macromol. Symp*. **2000**, *149*, 269.

[4] Wei, X.; Hong, S. C.; Zhuang, X.; Goto, T.; Shen, Y. R. *Phys. Rev. E* **2000**, *62*, 5160.

[5] Rao, A.; Rangwalla, H.; Varshney, V.; Dhinojwala, A. *Langmuir* **2004**, *20*, 7183.

[6] Donley, J.P.; Wu, D.T.; Fredrickson, G.H.;  *Macromolecules* **1997**, 30, 2167.

[7] Zhang, D; Shen, Y.R.; Somorjai, G.A. *Chem. Phys. Lett.*  **1997**, *281*, 394.

[8] Gracias, D.H.; Zhang D.; Lianos, L.; Ibach, W.; Shen, Y.R.; Somorjai, G.A. *Chem. Phys.*  **1999**, *245*, 277.

[9] Opdahl, A.; Phillips, R.A.; Somorjai, G.A. *J. Phys. Chem B*  **2002,** *106* 5212**.**

[10] Galuska, A.A.; Halverson, D.E. *Surface and Interface Analysis*  **1998**, *26*, 425.

[11] Wei, X.; Hong, S.C.; Zhuang, X.; Goto, T.; Shen, Y.R.; *Phys. Rev. E* **2000**, *62*, 5160.

[12] Rao, A.; Rangwalla, H.; Varshney, V.; Dhinojwala, A. *Langmuir* **2004**, *20*, 7183.

[13] Zhang, D.; Gracias, D.H.; Ward, R.; Gauckler, M.; Tian, Y.; Shen, Y.R.; Somorjai, G.A.; *J. Phys. Chem. B* **1998**, *102*, 6225.

[14] Opdahl, A.; Phillips, R.A.; Somorjai, G.A.; *Macromolecules* **2002**, *35*, 4387.

[15] Lu, R.; Gan, W.; Wu, B.; Zhang, Z.; Guo, Y.; Wang, H.; *J. Phys. Chem. B* **2005**, 109, 14118.

[16] Du, Q.; Superfine, R.; Freysz, E.; Shen, Y.R.; *Phys. Rev. Lett*. **1993**, 70, 2313.

[17] Roberts, R.F.; Allara, D.L., Pryde, C.A., Buchanan, D.N.E.; Hobbins, N.D. *Surf. Interface. Anal.* **1980**, *2*, 5.

[18] Briggs, D. <u>Surface Analysis of Polymers by XPS and Static SIMS</u>, Cambridge University Press, **1998**, Chapter 2.2, pages 27-46.

[19] Opdahl, A.; Phillips, R.A.; Somorjai, G.A.; *J. Phys. Chem. B* **2002**, 106, 5212.

[20] Lu, R.; Gan, W.; Wu, B.; Chen, H.; Wang, H.; *J. Phys. Chem. B* **2004**, 108, 7297.

[21] Gautam, K.S.; Schwab, A.D.; Dhinojwala, A.; Zhang, D.; Dougal, S.M.; Yeganeh, M.S.; *Phys. Rev. Lett*. **2000**, 85, 3854.

[22] Opdahl, A.; Phillips, R.; Somorjai, G. A.; *J. Phys. Chem. B* **2002**, 106, 5212.

[23] Briggman, K.A.; Stephenson, J.C.; Wallace, W.E.; Richter, L.J.; *J. Phys. Chem. B* **2001**, 105, 2785.

[24] Sikka, M.; Singh, N.; Karim, A.; Bates, F.S.; Satija, S.K.; Majkrzak, C.F.; *Phys. Rev. Lett.* **1993**, 70, 307.

[25] Krishnamoorti, R.; Graessley, W.W.; Balsara, N.P.; Lohse, D.J.; *Macromolecules* **1994**, 27, 3073.

# Chapter 5

# Cooperation of water and temperature induced properties of acrylamide films

## 5.1 Introduction

Poly($N$-isopropylacrylamide) (pNIPAM) was studied extensively for decades for its reversible phase transition behavior: the swollen polymer matrix in an aqueous solution collapses as the temperature is increased above the lower critical solution temperature (LCST). This transition around physiological temperature has recently found wide applications[1] including drug release,[2,3] chromatography for bioseparation,[4,5,6,7] biosensors,[8,9] catalytic reaction control,[10,11] gene delivery,[12,13] protein folding[14] and microactuators.[15,16] When immobilized onto a flat substrate, the LCST behavior of pNIPAM leads to a temperature controlled wettability change on the surface and has been used for control of protein adsorption[17,18] and cell adhesion.[19,20,21,22] The recent work by

Okano and colleagues to recover cell sheets from pNIPAM-grafted surfaces[23,24] brings exciting applications of the grafted polymer to 2-D and 3-D tissue engineering.

In spite of the great interest in thermoresponsive polymer coatings based on pNIPAM, characterizations of pNIPAM properties such as chemical,[25,26] thermal,[27,28] structural,[29,30,31] mechanical,[3233] and optical properties[34,35,36] have mostly been performed with bulk polymer in an aqueous solution. A direct study of grafted thin pNIPAM film is thus necessary and relevant for its surface applications.

In this chapter, pNIPAM-grafted surface is studied with multiple complementary surface analytical techniques. The pNIPAM thin film is produced specifically using plasma polymerization (ppNIPAM),[37] which is a one-step, solvent free, vapor-phase technique to produce conformal, sterile, tightly adhering and ultrathin coatings. Previously, ppNIPAM stimulation of different cell responses depending on the surface temperature and its application for proteomic and cellomic chips we demonstrated.[3839] Here, the mechanical and chemical properties of the thin film are characterized to better understand the behavior of the polymer itself. The temperature induced wettability change of the polymer coating was studied by contact angle measurements. To correlate the surface wettability with the polymer mechanical property, atomic force microscopy (AFM) was applied to study the topography and modulus of the thin film under ambient conditions in water.[40,41] Finally sum frequency generation (SFG) vibrational microscopy is used to probe the species of the surface functional groups. The study demonstrates that temperature affects the wettability, mechanical properties and conformation of the surface thin film. These observations are consistent with those previous reported for bulk pNIPAM in solution.

## 5.2 Experimental Procedures

**Substrate Preparation.** Silicon wafers were obtained from Silicon Valley Microelectronics (San Jose, CA) and diced into 1cm × 1cm squares. Calcium fluoride ($CaF_2$) crystals were purchased from International Scientific Products (Irvington, NY). The wafers and $CaF_2$ samples were cleaned by sonication in methylene chloride (Fisher Scientific, Fairlawn, NJ), acetone (Fisher Scientific, Fairlawn, NJ), methanol (Fisher Scientific, Fairlawn, NJ) and 18 mΩ de-ionized (DI) water (Millipore, Billerica, MA) twice each for 10 minutes. The surfaces were then subjected to a 30 minutes UV/ozone oxidation treatment to remove trace organic contaminants before further usage.

**Plasma Polymerization.** Plasma polymerization of NIPAM was carried out in a custom-built reactor using the protocol described earlier.[37] In brief, the powered electrode is connected to a 13.56 MHz radio frequency power source and a manual impedance matching network. The deposition process included an 80W methane plasma deposition, followed by NIPAM plasma deposition with stepwise decreasing powers from 80W to 1W with a processing pressure of 140 mTorr. The ppNIPAM-grafted surfaces were rinsed three times with cold deionized water to remove uncrosslinked molecules before use.

**Mask Preparation and Removal.** To measure ppNIPAM film thickness, a mask was applied on the center of a silicon chip to block deposition in a certain region on the substrate. The mask solution was prepared by dissolving poly(lactic acid) (PLA) (Fisher Scientific, Fairlawn, NJ) in acetone to make a 10% (w/v) solution. Five microliter of this solution was pipetted onto silicon samples and air dried for a minimum of 5 minutes

immediately preceding plasma deposition. After plasma deposition, the PLA mask was removed carefully using tweezers.

**Preparation of pNIPAM by Free Radical Polymerization.** The control bulk pNIPAM (Fig. 5-1) was synthesized by free radical polymerization using protocols adapted from previous publication by Schild *et al.*.[42] The reaction was carried out in benzene using azobisisobutyronitrile (AIBN, $C_8H_{12}N_4$) as the free radical initiator to obtain the polymer. One gram polymer was dissolved in 6 mL deionized water at room temperature to make a pNIPAM solution. Twenty microliter solution was pipetted on a piece of silicon (8 x 8mm) and spin cast at 4000 rpm for 20 seconds to form the control surface for ToF-SIMS study.
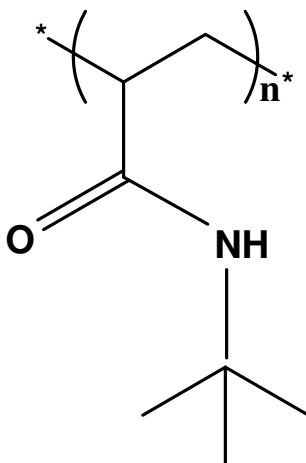


**Figure 5-1:** Molecular structure of conventional pNIPAM synthesized by free radical polymerization.

**Contact Angle Measurement.** Surface wettability was evaluated by a captive air bubble method. This was done by measuring static contact angles generated by an air bubble in contact with the sample submerged in pure water using a contact angle

goniometer (Ramé-hart, Mountain Lakes, NJ). The samples were allowed to equilibrate for at least an hour in the water bath at the appropriate temperature before any measurements were taken.

**AFM Measurements.** All AFM measurements were performed using ppNIPAM deposited silicon chips on a PicoScan$^{TM}$ microscope (Molecular Imaging, Phoenix, AZ). Samples were hydrated in DI-water for an hour and then quickly transferred to a Teflon cell containing deionized water for measurement. The cell was mounted on a MI thermal stage controlled by a temperature controller (Model 321, Lake Shore Cryotronics, Westerville, OH) and data were collected in the range of 25°C to 37°C. The samples were allowed to equilibrate for at least half an hour at each temperature before the measurements were taken.

Topography images were obtained in the acoustic AC mode using rectangular silicon cantilevers with integrated sharp tips, having resonance frequencies in the range of 260 –410 kHz (PPP-NCH type, Nanosensors, Neuchatel, Switzerland). The boundary between the plasma polymer coated and uncoated regions were aligned directly below the AFM tip using an add-on CCD camera. The images were analyzed using Image J software (http://rsb.info.nih.gov/ij/) to get height histogram, average step height and roughness information.

The force displacement curves were taken with standard V-shaped silicon nitride cantilevers (Nanoprobe$^{TM}$ AFM tips, Type NP-S, Digital Instruments, Santa Barbara, CA). The tip spring constant was 0.06 N/m according to the manufacturer's specifications. The tip radius was measured to be 50 – 60 nm by scanning an Ultrasharp calibration grating that contains an array of sharp tips (TGT01 model, Silicon-MDT,

Moscow, Russia). These blunt tip cantilevers were selected to satisfy conditions for elastic mechanical contact.[43] Five to ten force displacement curves were acquired at randomly selected regions at each temperature using an approach-retract frequency of 0.5Hz.

To calibrate the detector signal (in volts), portions of the force displacement curve were taken on a reference surface, which is assumed to have infinitely high stiffness and no deformation from pressing. In our study, a piece of clean silicon wafer was used as the reference surface, whose modulus is 160GPa and several orders of magnitude higher than the polymer.

The measured force-displacement curves were converted to plots relating indentation depth vs. loading force according to previously described methods.[44] The indentation of the cantilever under a given load was fit to the Hertz model for indentation of a sphere on an elastic solid and used to calculate the elastic modulus of the surface thin film.[45] The indentation depth was controlled around or below 20% of the film thickness to minimize the influence of the solid support.[46][47] To exclude the possibility of polymer plastic deformation, multiple curves on the same location were recorded and identical curves were obtained, indicating full recovery of surfaces for each indentation cycle.

**SFG Measurements.** Surface vibrational spectra were obtained by sum frequency generation (SFG) vibrational spectroscopy in order to understand the functional groups at the outermost surface interface with submonolayer sensitivity. Details of the technique can be found in some recent papers.[48,49,50] The specific laser system used for our study was described by Kim *et al.*[51] Briefly, surface vibrational spectra of ppNIPAM deposited on $CaF_2$ crystals were collected by overlapping visible and tunable infrared laser pulses

on the polymer surface and measuring the induced sum-frequency signal. In this study, the spectra was collected using a $s_{sum}s_{vis}p_{IR}$ polarization combination. The SFG spectra in air were taken by aligning the polymer face of the sample toward the light source with the angle of incident light set at 45° with respect to the surface normal. For studies in water, the polymer film was immersed in pure water and the incident light was projected from the side opposite the polymer film. Light reflected from the solid-liquid interface was collected after traveling twice through the crystal. The incident light angle and polarization were the same as those used for the air spectra. The spectra collected cover the CH-stretch region from 2800-3050 cm$^{-1}$ in 5cm$^{-1}$ increments. For a given condition, SFG measurements were repeated on at least three different samples with 1-3 spots probed on each sample. For each sample spot 4-5 scans were performed with 100 shots/data point to increase the signal-to-noise ratio. The collected data were averaged to produce the final spectra presented here.

## 5.3 Results and Discussion

**Change in Surface Wettability by Contact Angles.** To directly evaluate the wettability of the ppNIPAM film, a captive air bubble contact angle of the ppNIPAM film surface was measured in water. The contact angles on ppNIPAM change from 34 ± 1.0° at 20°C to 40 ± 0.5° at 45°C (n ≥ 11), which are comparable with measurements by Akiyama *et al.* using a silane grafted pNIPAM thin film.[52] Similar measurements taken on untreated bare silicon show no statistical change in the surface contact angles over the same temperature range (41 ± 0.6° at 20°C to 40 ± 0.6° at 45°C). The significantly lower contact angle at room temperature on ppNIPAM indicates that the plasma film becomes

more hydrated when the temperature is below the LCST. Thus, the surface wettability change with temperature confirms the thermoresponsive property of ppNIPAM film.

**Surface Topography by AFM.** Bulk pNIPAM polymer demonstrates a transition in volume and modulus through its LCST.[32,33] To test whether this is also the case with plasma deposited thermoresponsive film, the surface topographic and mechanical property of ppNIPAM were studied using AFM. Fig. 5-2 shows the surface topography of a ppNIPAM film imaged in water by AFM at 25°C and 37°C. The surface is fairly smooth at 37°C with a root-mean-square (RMS) roughness of 3.5 ± 0.5 nm over a 5 μm × 5 μm scan area. When the same size image is taken at 25°C, the RMS roughness increases to 5.3 ± 1.1 nm. It has been previously observed that when ppNIPAM hydrates at room temperature, it creates nano-cavities on the surface, which probably accounts for the slight increase in surface roughness observed in the swollen state.
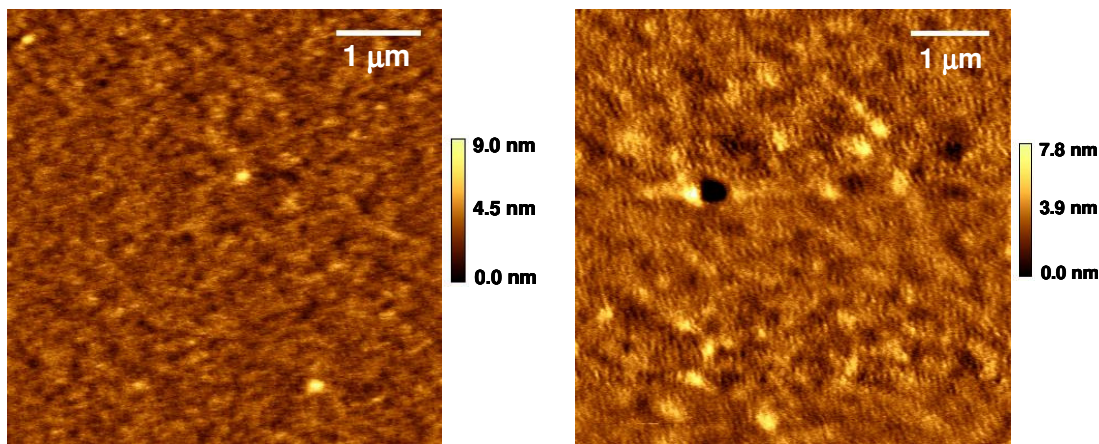


**Figure 5-2:** AFM images of ppNIPAM in water at 25°C (left) and 37°C (right) .

To determine the film thickness in water at different temperatures, ppNIPAM steps are created by plasma deposition over a partly masked sample and removing the mask afterwards. Two characteristic AFM images of the same area across a ppNIPAM

94

step with the height histograms and section analysis are shown in Fig. 5-3. The height histograms obtained for each image give two characteristic peaks corresponding to the substrate and coating heights, and the film thickness is obtained. A Gaussian model is used to fit each peak in the histograms The distances between the two peaks are 73.7 nm and 63.7 nm at 25°C and 37°C respectively, indicating a 10 nm decrease in film thickness above the LCST compared to below the LCST. Identical histogram analyses were performed on 4 samples of different deposition batches and 3 spots on each sample. A small batch-to-batch variation of the film thickness at the same temperature may arise from variation in the plasma polymerization process.
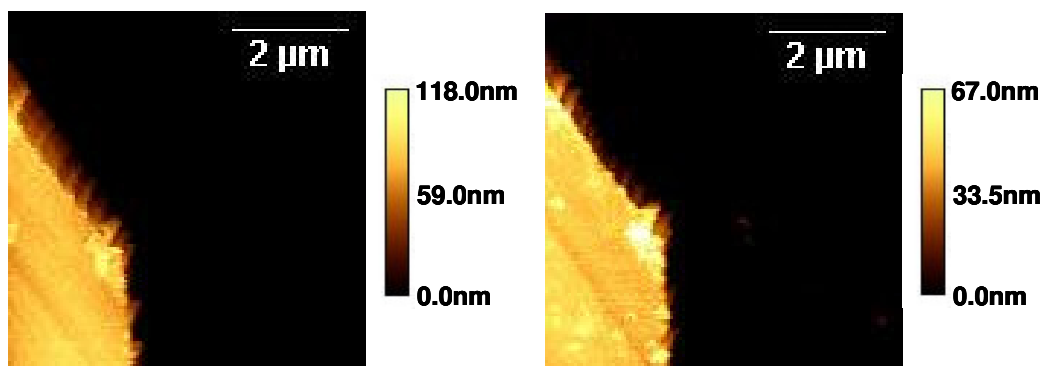


**Figure 5-3:** AFM images of a ppNIPAM step on a silicon surface at 25°C (a) and 37°C (d).

**Mechanical Property by Force Displacement Curves.** Since the ppNIPAM film thickness/volume changes with temperature, it is expected that the polymer mechanical properties also vary.[32] Scanning force microscopy has been shown as a unique tool to probe the micromechanical properties of thin film coatings.[53545556] Fig.5-4 shows a sample AFM force vs. distance curves obtained on bare silicon at room temperature and on ppNIPAM surface at 25°C and 37°C in pure water. In this figure, the cantilever

95

deflection is presented as a function of the $z$-piezo displacement. It is clearly seen that the cantilever deflects less for the same z-piezo movement at 25°C than at 37°C, indicating the polymer is softer and swollen at 25°C.

To quantitatively compare the thin film mechanical property, the force displacement data are converted to plots relating the indentation depth as a function of the loading force. The elastic moduli are obtained from best fitting to the indentation vs. load data using the Hertz model. The parameters used are R= 53 nm and $\nu$= 0.5 assuming elastic deformation. The spring constant, taken from the manufacturer's specifications, is 0.06 N/m. As the Hertz model assumes that the two contacting surfaces have homogeneous elastic properties in the z direction, this deviation is likely due to the substrate effect that the simple Hertz model cannot model as reported by Domke and Radmacher.[50] Using the optimal fitting parameters, the elastic moduli are calculated to be 185.2 kPa at 25°C and 1.592 MPa at 37°C for the two curves shown in Fig. 5-4. Thus, the local stiffness of ppNIPAM is more than 8 times higher in the collapsed state at 37°C than the swollen state at 25°C.
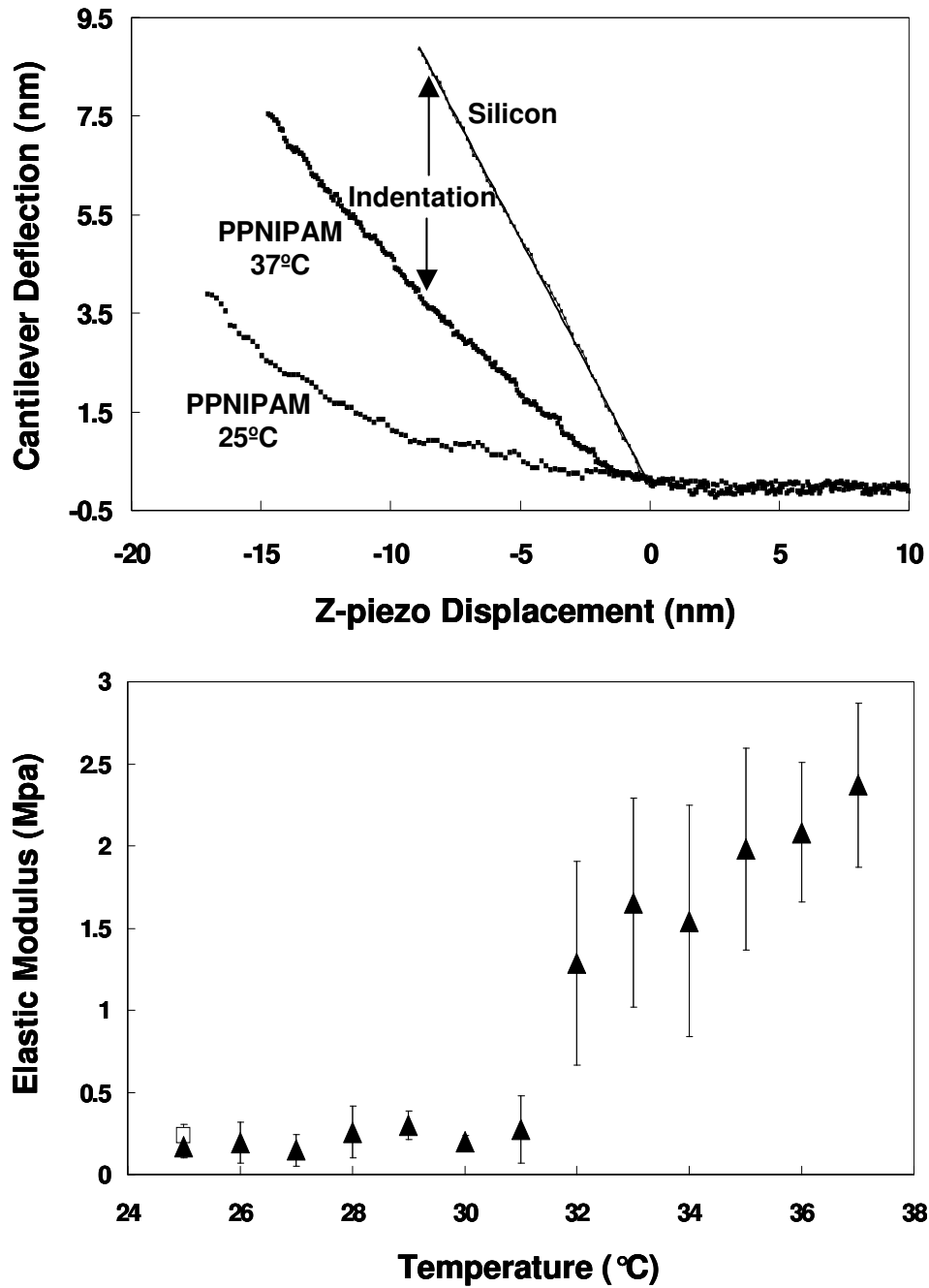
**Figure 5-4:** Force displacement curves (top) by AFM on ppNIPAM coatings in pure water at 25°C (bottom line) and 37°C (middle line) and on silicon (top line). Young's modulus of ppNIPAM are calculated from force displacement curves acquired at 25°C to 37°C with 1°C temperature increments (▲) and the reverse (□) (bottom).

In an aqueous environment, bulk polymer chains of pNIPAM are believed to adopt a random coil configuration below the LCST, and a more compact globular configuration above the LCST. This conformational transition accounts for changes in both polymer volume and mechanical properties.[33] The AFM study demonstrates that the ppNIPAM thin film is still able to transition between the collapsed or swollen state depending on the temperature. However, when comparing the mechanical characteristics of ppNIPAM thin film produced with those of pNIPAM gel synthesized by free radical polymerization in the bulk state, some obvious differences are noticed. Matzelle *et al*. recently reported a swelling ratio of eight and elastic moduli of 2.8 kPa and 183 kPa at 25°C and 35°C respectively for a lightly crosslinked pNIPAM gel (100:1 monomer to crosslinker molar ratio) cast on mica.[60] The surface immobilized ppNIPAM however, has a higher moduli (185kPa and 1.592MPa) and lower swelling ratio (< 1). This would seem to support tim of flight-secondary ion mass spectroscopy (ToF-SIMS) data that the ppNIPAM film is more extensively cross-linked, as dense crosslinks have been shown to greatly restrict the magnitude of the swelling ratio and reinforce the polymer mechanical property.[32,33,5758] Nevertheless, the moduli below and above the LCST obtained still falls in the soft hydrogel range.[59]

To determine at which temperature the transition in surface stiffness happens, force-distance curve measurements were taken at 1°C increments from 24°C to 37°C. Five to ten randomly selected spots were probed at each temperature with the average elastic moduli summarized in Fig. 5-4 (bottom). The surface stiffness increases significantly around 31°C -32°C, close to the transition temperature measured by Pan *et al*. using an AFM modulation measurement.[37] To confirm that the stiffness transition

behavior is reversible, the surface is cooled down to 25°C again and the measured modulus is shown as an open squares. It is clearly observed that the film rehydrates and swells after cooling to below its LCST.

**Surface Group Rearrangement by SFG.** To determine whether the surface chemistry of ppNIPAM films changes *in situ* at different temperatures the ppNIPAM film is analyzed with SFG vibrational spectroscopy. SFG selection rules allow the detection of chemical species that are oriented and lack inversion symmetry, thus allowing the top few atomic layers of the polymer surface to be probed directly.[51-53,60] Fig. 5-5 demonstrates the complete reconstruction of the surface upon submersion in pure water at room temperature. Fig. 5-6 shows characteristic SFG spectra for the carbon region taken in water at room temperature and 37°C. For comparison, the spectrum of ppNIPAM in air at room temperature is plotted in the same figure. As water adsorption tends to attenuate the signal, the spectra in water are multiplied by a factor of four. Fig. 5-6(a) shows the spectrum of fully dehydrated ppNIPAM film in air where two peaks are predominant centering at 2875 and 2940 cm$^{-1}$. These two peaks are assigned as the $CH_3$ (s) stretch and Fermi resonance between $CH_3$ stretch and a bending mode . There are also three shoulder peaks measured at approximately 2855 cm$^{-1}$, 2925 cm$^{-1}$ and 2960 cm$^{-1}$, which are assigned as the $CH_2$ (s), $CH_2$ (a) and $CH_3$ (a) stretches. The strong $CH_3$ stretch peak indicates exposure of hydrophobic isopropyl groups from the polymer side chain to air in the dehydrated state. The $CH_2$ stretch in the spectrum may arise from the backbone, or from random crosslinking induced by the plasma deposition process. This is expected given that SFG spectra provides the averaged chemical information over a 1mm$^2$ spot size. When the spectrum is acquired in water at 37°C, a broad peak is observed between

2900 and 2980 cm$^{-1}$, which is associated with the CH$_2$ (a) stretch, CH$_3$ Fermi resonance and CH$_3$ (a) stretch peaks. This suggests extension of the hydrophobic isopropyl side chain to the aqueous environment above the LCST. In contrast, we find no evidence of these peaks at room temperature. This strongly indicates disordering of the hydrophobic isopropyl groups to the interior of the polymer, away from the surface which is being probed. It has been hypothesized that below the LCST, the amide groups will extend into the aqueous environment to participate in hydrogen bonding, although we are not able to directly observe this as the characteristic peaks are not detected in this region.
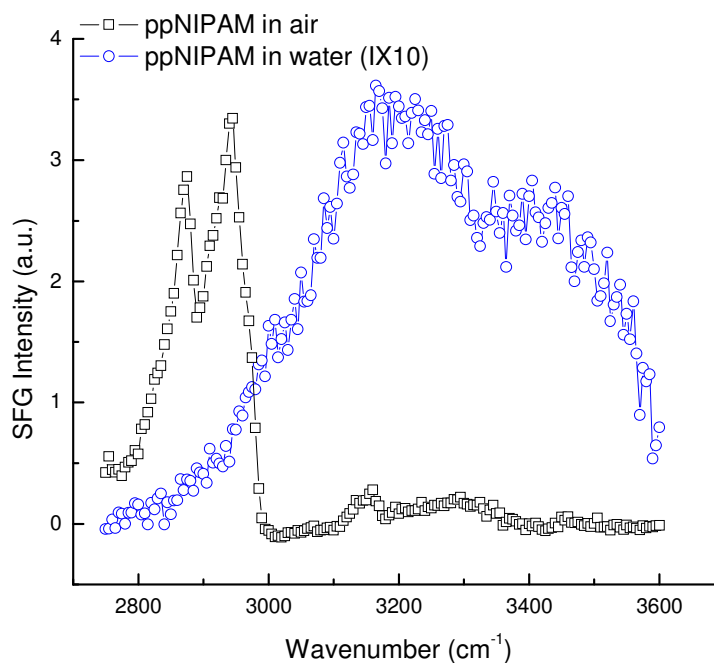


**Figure 5-5:** SFG spectra of ppNIPAM in air at room temperature (□), and in pure water at room temperature (○).
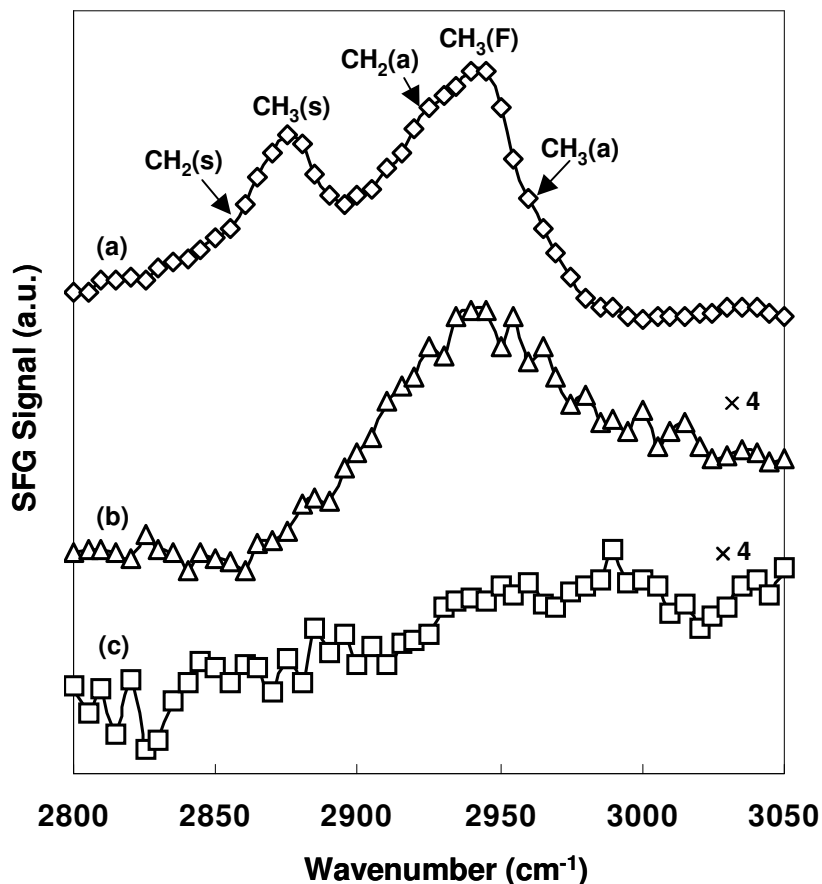
**Figure 5-6:** SFG spectra of the CH region ppNIPAM in (a) air at room temperature, (b) pure water at 37°C and (c) pure water at room temperature (25$^{o}$C)..

The results from our SFG characterization of ppNIPAM films in situ above and below the LCST seem to support the hypothesis that ppNIPAM films retain the behavior characteristic of their conventionally formed counterparts. The structural rearrangement of the ppNIPAM polymer side chain provides evidence to support the currently proposed mechanism of LCST behavior of thermoresponsive polymers.[61] It has been proposed that, below the LCST, well-hydrated pNIPAM chains take a random coil configuration in aqueous environment with amide groups forming hydrogen bonds with water, but a more compact globular configuration and an increased hydrophobic interaction by a sudden

dehydration above its LCST. Associated with the polymer conformation change, we directly observe the re-orientation of the surface chemical functionalities using SFG. In the dehydrated state, the polymer surface orients the hydrophobic group outwards to maximize hydrogen bonding underneath the surface.[62] In the aqueous environment at room temperature, on the other hand, the hydrophobic isopropyl groups appear to bend inwards to allow hydrogen bonding of the polar amide groups with water to lower surface energy. While above the LCST in water, the surface rearranges to resemble the one in air due to an entropy-driven process to free the bound water molecules and re-form intramolecular hydrogen bonds under the surface.[63] This exposure of surface chemical functionalities of different polarities also explains the change of surface contact angles as a function of temperature.

## 5.4 Conclusion

This chapter delves into the characterization of a plasma deposited NIPAM thin film using multiple complementary techniques. The ppNIPAM is found to resemble the conventional bulk polymer in surface wettability, structural and elasticity transition through the LCST at around 31-32°C. The surface wettability as well as polymer thickness decreases while the film elastic modulus increases when water temperature goes from 25 to 35°C. However, the magnitude of moduli and swelling ratio differs between ppNIPAM and pNIPAM. This may arise from crosslinking in the plasma polymer. Associated with wettability and mechanical property transition, re-orientation of the side-chain groups is directly probed by SFG measurements. That the features

attributed to methyl groups disappear at room temperature suggests different hydrogen bond levels and water structure on the surfaces.

# References

[1] Roy, I.; Gupta, M. N. *Chem. Biol.* **2003**, *10*, 1161.

[2] Coughlan, D. C.; Quilty, F. P.; Corrigan, O. I. *J. Control. Release* **2004**, *98*, 97.

[3] Kost, J.; Langer, R. *Adv. Drug Deliv. Rev.* **2001**, *46*, 125.

[4] Kikuchi, A.; Okano, T. *Macromol. Symp.* **2004**, *207*, 217.

[5] Kobayashi, J.; Kikuchi, A.; Sakai, K.; Okano, T. *Anal. Chem.* **2003**, *75*, 3244.

[6] Kobayashi, J.; Kikuchi, A.; Sakai, K.; Okano, T. *Anal. Chem.* **2001**, *73*, 2027.

[7] Fong, R. B.; Ding, Z. L.; Hoffman, A. S.; Stayton, P. S. *Biotechnol. Bioeng.* **2002**, *79*, 271.

[8] Malmstadt, N.; Yager, P.; Hoffman, A. S.; Stayton, P. S. *Anal. Chem.* **2003**, *75*, 2943.

[9] Zhu, Q. Z.; Yang, H. H.; Li, D. H.; Chen, Q. Y.; Xu, J. G. *Analyst* **2000**, *125*, 2260.

[10] Nagayama, H.; Maeda, Y.; Shimasaki, C.; Kitano, H. *Macromol. Chem. Phys.* **1995**, *196*, 611.

[11] Stayton, P. S.; Shimboji, T.; Long, C.; Chilkoti, A.; Chen, G.; Harris, J. M.; Hoffman, A. S. *Nature* **1995**, *378*, 472.

[12] Twaites, B. R.; Alarcon, C. D.; Cunliffe, D.; Lavigne, M.; Pennadam, S.; Smith, J. R.; Gorecki, D. C.; Alexander, C. *J. Control. Release* **2004**, *97*, 551.

[13] Kurisawa, M.; Yokoyama, M.; Okano, T. *J. Control. Release* **2000**, *68*, 1-8.

[14] Chen, Y. J.; Huang, L. W.; Chiu, H. C.; Lin, S. C. *Enzyme Microb. Technol.* **2003**, *32*, 120.

[15] Luo, Q. Z.; Mutlu, S.; Gianchandani, Y. B.; Svec, F.; Frechet, J. M. J. *Electrophoresis* **2003**, *24*, 3694.

[16] Harmon, M. E.; Tang, M.; Frank, C. W. *Polymer* **2003**, *44*, 4547.

[17] Huber, D. L.; Manginell, R. P.; Samara, M. A.; Kim, B. I.; Bunker, B. C. *Science* **2003**, *301*, 352.

[18] Grabstain, V.; Bianco-Peled, H. *Biotechnol. Prog.* **2003**, *19*, 1728.

[19] Ista, L. K.; Mendez, S.; Perez-Luna, V. H.; Lopez, G. P. *Langmuir* **2001**, *17*, 2552.

[20] Ratner, B. D.; Cheng, X. H.; Wang, Y. B.; Hanein, Y.; Bohringer, K. *Abstr. Pap. Am. Chem. Soc.* **2003**, *225*, U582.

[21] Liu, H. C.; Ito, Y. *J. Biomed. Mater. Res. Part A* **2003**, *67A*, 1424.

[22] Canavan, H. E.; Cheng, X.; Graham, D. J.; Ratner, B. D.; Castner, D. G. *Langmuir* **2004,** 1949 .

[23] Tsuda, Y.; Kikuchi, A.; Yamato, M.; Sakurai, Y.; Umezu, M.; Okano, T. *J. Biomed. Mater. Res. Part A* **2004**, *69A*, 70.

[24] Shimizu, T.; Yamato, M.; Isoi, Y.; Akutsu, T.; Setomaru, T.; Abe, K.; Kikuchi, A.; Umezu, M.; Okano, T. *Circ.Res.* **2002**, *90*, E40.

[25] Maeda, Y.; Higuchi, T.; Ikeda, I. *Langmuir* **2001**, *17*, 7535-.

[26] Katsumoto, Y.; Tanaka, T.; Sato, H.; Ozaki, Y. *J. Phys. Chem. A* **2002**, *106*, 3429.

[27] Boutris, C.; Chatzi, E. G.; Kiparissides, C. *Polymer* **1997**, *38*, 2567.

[28] Cai, W. S.; Gan, L. H.; Tam, K. C. *Colloid Polym. Sci.* **2001**, *279*, 793.

[29] Reichelt, R.; Schmidt, T.; Kuckling, D.; Arndt, K. F. *Macromol. Symp.* **2004**, *210*, 501.

[30] Chern, J. M.; Lee, W. F.; Hsieh, M. Y. *J. Appl. Polym. Sci.* **2004**, *92*, 3651.

[31] Tam, K. C.; Wu, X. Y.; Pelton, R. H. *Polymer* **1992**, *33*, 436.

[32] Hirotsu, S. *J. Chem. Phys.* **1991**, *94*, 3949.

[33] Shibayama, M.; Morimoto, M.; Nomura, S. *Macromolecules* **1994**, *27*, 5060.

[34] Suzuki, Y.; Nozaki, K.; Yamamoto, T.; Itoh, K.; Nishio, I. *J. Chem. Phys.* **1992**, *97*, 3808.

[35] Takeoka, Y.; Watanabe, M. *Adv. Mater.* **2003**, *15*, 199.

[36] Reese, C. E.; Mikhonin, A. V.; Kamenjicki, M.; Tikhonov, A.; Asher, S. A. *J. Am. Chem. Soc.* **2004**, *126*, 1493.

[37] Pan, Y. V.; Wesley, R. A.; Luginbuhl, R.; Denton, D. D.; Ratner, B. D. *Biomacromolecules* **2001**, *2*, 32.

[38] Wang, Y. B.; Cheng, X. C.; Hanein, Y.; Shastry, A.; Denton, D. D.; Ratner, B. D.; Bohringer, K. F. *Proceedings of the 12th International Conference on Solid-State Sensors and Actuators (Transducers'03)*; Boston, MA, **2003**.

[39] Cheng, X. H.; Wang, Y. B.; Hanein, Y.; Bohringer, K. F.; Ratner, B. D. *J. Biomed. Mater. Res. Part A* **2004**, *70A*, 159.

[40] Sheiko, S. S. New Developments in Polymer Analytics Ii **2000**, 151, 61.

[41] Reich, Z.; Kapon, R.; Nevo, R.; Pilpel, Y.; Zmora, S.; Scolnik, Y. *Biotechnol. Adv.* **2001**, *19*, 451.

[42] Schild, H. G.; Tirrell, D. A. *Langmuir* **1991**, *7*, 665.

[43] Tsukruk, V. V.; Sidorenko, A.; Gorbunov, V. V.; Chizhik, S. A. *Langmuir* **2001**, *17*, 6715.

[44] Chizhik, S. A.; Huang, Z.; Gorbunov, V. V.; Myshkin, N. K.; Tsukruk, V. V. *Langmuir* **1998**, *14*, 2606.

[45] Tsukruk, V. V.; Huang, Z.; Chizhik, S. A.; Gorbunov, V. V. *J. Mater. Sci.* **1998**, *33*, 4905.

[46] Harmon, M. E.; Kuckling, D.; Pareek, P.; Frank, C. W. *Langmuir* **2003**, *19*, 10947.

[47] Domke, J.; Radmacher, M. *Langmuir* **1998**, *14*, 3320.

[48] Chen, Z.; Shen, Y. R.; Somorjai, G. A. *Annu. Rev. Phys. Chem.* **2002**, *53*, 437.

[49] Miranda, P. B.; Shen, Y. R. *J. Phys. Chem. B* **1999**, *103*, 3292.

[50] Opdahl, A.; Hoffer, S.; Mailhot, B.; Somorjai, G. *Chem. Rec.* **2001**, *1*, 101.

[51] Kim, J.; Koffas, T. S.; Lawrence, C. C.; Somorjai, G. A. *Langmuir* **2004**, *20*, 4640.

[52] Akiyama, Y.; Kikuchi, A.; Yamato, M.; Okano, T. *Langmuir* **2004**, *20*, 5506.

[53] Munz, M.; Cappella, B.; Sturm, H.; Geuss, M.; Schulz, E. *Filler-Reinforced Elastomers Scanning Force Microscopy* **2003**, *164*, 87-210.

[54] Janicijevic, A.; Ristic, D.; Wyman, C. *J. Microsc.-Oxf.* **2003**, *212*, 264.

[55] Jandt, K. D. *Mater. Sci. Eng. R-Rep.* **1998**, *21*, 221.

[56] Baker, S. P. *Thin Solid Films* **1997**, *308*, 289.

[57] Senff, H.; Richtering, W. *Colloid Polym. Sci.* **2000**, *278*, 830.

[58] Takahashi, K.; Takigawa, T.; Masuda, T. *J. Chem. Phys.* **2004**, *120*, 2972.

[59] Kim, S. H.; Opdahl, A.; Marmo, C.; Somorjai, G. A. *Biomaterials* **2002**, *23*, 1657.

[60] Chen, Z.; Ward, R.; Tian, Y.; Eppler, A. S.; Shen, Y. R.; Somorjai, G. A. *J. Phys. Chem. B* **1999**, *103*, 2935.

[61] Lin, S. Y.; Chen, K. S.; Liang, R. C. *Polymer* **1999**, *40*, 2619.

[62] Chen, Q.; Zhang, D.; Somorjai, G.; Bertozzi, C. R. *J. Am. Chem. Soc.* **1999**, *121*, 446.

[63] Bruscolini, P.; Casetti, L. *Phys. Rev. E* **2001**, *6405*, art. no.-051805.

# Chapter 6

# Ordered interfaces formed between poly(2-hydroxyethyl methacrylate) (PHEMA) free and buried interfaces with liquids

## 6.1 Introduction

This chapter investigates the method by which solvents disrupt ordering at polymer interfaces, and uses SFG vibrational spectroscopy to characterize the structure of well-defined interfaces formed between poly(2-hydroxyethyl methacrylate) (PHEMA) film and various liquids. PHEMA is an amphiphilic hydrogel and polar liquids that are miscible with the polymer. Detailed knowledge of the variables that influence the molecular structure of buried polymer/liquid and saturated polymer/solid interfaces is important for understanding interface specific processes including adhesion, wetting, and adsorption. One example is the commonly observed 'contact angle hysteresis' between the advancing and retreating angles of a liquid droplet on a solid surface. Many factors are thought to contribute to contact angle hysteresis including surface roughness, surface

chemical heterogeneity, glas transition temperature depression, mechanical properties, and miscibility of the two contacting materials.[1,2,3] For polymers, it is also generally believed that molecular restructuring events between the polymer/air and polymer/liquid interfaces play a role in this phenomenon. In order to determine the degree to which restructuring influences a phenomenon like contact angle hysteresis, it is necessary to have experimental measurements of the structures of polymers at both air, liquid, and solid interfaces. Many experimental techniques exist for studying buried polymer interfaces - few are capable of providing direct molecular level information of the interaction between the polymer and liquid phases. Sum frequency generation (SFG) vibrational spectroscopy is an experimental technique capable of providing molecular structure information of both open and buried polymer interfaces.[4]

For many polymers, SFG vibrational spectroscopy has been shown to be highly sensitive to ordering of polymer side branches at an interface.[5,6,7,8,9,10] At open air interfaces (i.e. free surfaces), studies have shown that bulky hydrophobic side branches are generally ordered and oriented away from the polymer bulk - in agreement with theoretical predictions.[11,12] Efforts have been made to study the behavior of polymers at solid and liquid interfaces using SFG vibrational spectroscopy.[13,14] Wilson[14] et al. have shown that polystyrene adapts different configurations upon contact with hydrophobic and with hydrophilic solids. Polymer mobility has been shown to be an important parameter when considering how quickly a polymer surface responds as soon as it is placed in contact with a liquid. Wang et al.[15] have shown that when placed in contact with water, the surfaces of rubbery methacrylate polymers restructure within a short time period, as opposed to the surfaces of glassy methacrylate polymers that remain stable.

Thus, similar to the conclusions in chapter 3, the surface glass transition temperature affects the polymer's ability to restructure.

Hydrogels have attracted significant attention mainly due to their biological compatibility and unique dynamic behavior. Because of their chemical and thermal stability, gels are suitable for a wide range of biomedical and pharmaceutical applications. Long-term biocompatibility and functionality strongly depend on the gel's absorption and interaction with the surrounding fluid. Swelling and diffusion through the network of hydrogel films have been studied with various techniques, including infrared (IR) spectroscopy, nuclear magnetic resonance, cavity ringdown spectroscopy, dielectric spectroscopy, and neutron diffraction.[15,16,17,18] However, relatively less research has been carried out to elucidate polymer-nonsolvent interactions in the bulk and interfaces of gel films.[19,20,21]

SFG spectra of vapor and liquid methanol (non-solvent for atactic polypropylene (aPP)) are shown in Fig. 6-1. Fig. 6-1 a and b show spectra of aPP/air and neat methanol/air respectively. $CH_3$ moieties dominate the surface, and both the polymer and liquid exhibit a low surface tension. aPP films were exposed to a vapor pressure of methanol (~150 torr) at room temperature. For the spectrum of aPP exposed to methanol vapor (Fig. 6-1c), the best fit is obtained using a combination of the peak assignments from aPP and from methanol. Although there is some interference between the Fermi resonances of the methanol and aPP (confirmed by exposing polymer to deuterated vapor), no visible restructuring of the aPP is visible. SFG spectrum collected from aPP in direct contact with methanol liquid is qualitatively similar and is shown in Fig. 6-1d. In this spectrum, the contribution from methanol is larger, relative to the aPP/methanol

vapor spectrum in Fig. 6-1c. This confirms that at the aPP/methanol liquid interface, the CH$_3$ groups from methanol are oriented towards the CH$_3$ side branches from $a$PP, indicating that the configuration of $a$PP at the interface does not measurably change under exposure to methanol vapor and liquid.
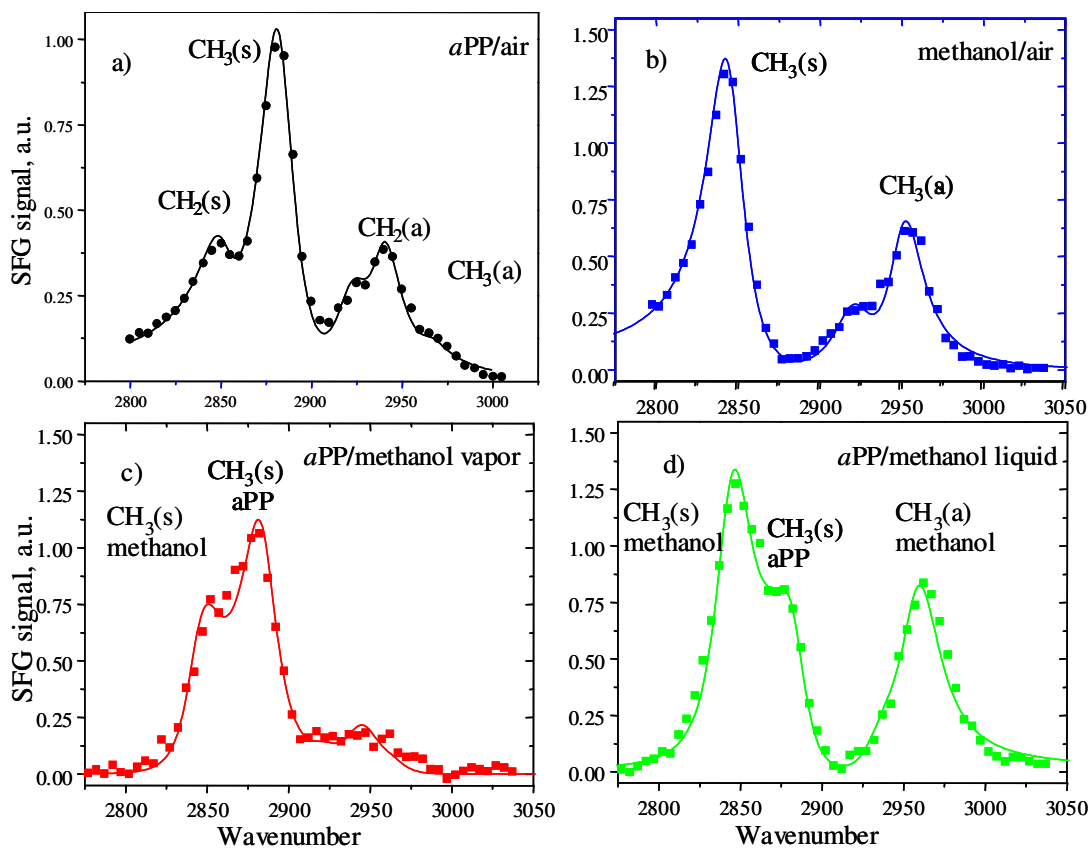


**Figure 6-1:** SFG spectra of (a) $a$PP/air interface (b) methanol liquid/vapor interface (c) $a$PP/methanol vapor interface (d) $a$PP/methanol liquid interface. All spectra were collected using the *ssp* polarization combination.

Although it is known that solvent incorporation in hydrogel films alters the bulk properties, the polymer physics at the interface require further in-depth study. Fourier transform IR spectroscopy studies of hydrogen bonding in the vicinity of the surface of

poly(2-hydroxyethyl methacrylate) (PHEMA) revealed differences between surface and bulk chemical structures.[16] However, insight into polymer conformation and restructuring at buried interfaces and free surfaces can only be accomplished with techniques exhibiting molecular resolution, such as infrared-visible sum frequency generation (SFG) vibrational spectroscopy.

The objective of this chapter was to explore conformational changes at the free surface and sapphire interface of PHEMA due to submersion into deuterated water ($D_2O$) and acetonitrile ($d_3ACN$). The polymer behavior and changes of the molecular structure were studied by SFG vibrational spectroscopy. This nonlinear optical technique was used to probe the interface response of PHEMA upon full saturation in the former two liquids. SFG results provided insight into conformational changes at the solid interface and the effects of the liquid surface tension and interface surface energy on the restructuring of the PHEMA films.

## 6.2 Experimental procedures

**Polymer films** Specimens were fabricated from pellets of PHEMA (Aldrich, St. Louis, MO) with molecular weight equal to 300000, glass transition temperature of ~55 ºC, and chemical structure shown schematically in Fig. 6-2. The PHEMA films were spin cast at 3000 rpm directly onto sapphire substrates from a d5-pyradine solution and annealed at 70 °C for 12 h. The film thickness was kept below 300 nm. The PHEMA films were fully saturated with $D_2O$ and $d_3ACN$ solvents of surface tension equal to 73.1 and 29.3 dyn/cm, respectively.
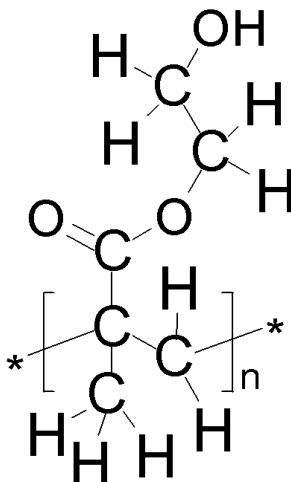
**Figure 6-2:** Molecular structure of poly(2-hydoxyethyl methacrylate) (PHEMA).

The sapphire prisms consisted of synthetic single-crystal sapphire ($\alpha$-Al$_2$O$_3$) with a root-mean-square roughness of 5-10 nm (Red Optronics, Mountain View, CA) and optical ĉ-axis perpendicular to the free surface. Calcium fluoride prisms (Altos Inc., Trabuco Canyon, CA) were used to obtain SFG spectra of the liquid-saturated PHEMA surfaces. The flatness and chemical composition of the sapphire and calcium fluoride prism surfaces were examined, respectively, with an atomic force microscope (AFM) fitted with an M5 head (Park Scientific Instruments, Sunnyvale, CA) and X-ray photoelectron spectroscope (XPS) system (PHI 5300, Perkin-Elmer, Boston, MA). AFM imaging confirmed the flatness of the prism surfaces, while XPS spectra (in addition to providing information about the prism composition) verified the absence of any surface contaminants. The sapphire prisms were cleaned in aqua regia (a mixture of hydrochloric and nitric acid), rinsed thoroughly in high-purity water, and, finally, exposed to UV-initiated ozone for >1 h, whereas the calcium fluoride prisms were rinsed profusely in

methanol and acetone. The prisms were used immediately after cleaning to minimize contamination from the atmosphere.

**SFG vibrational spectroscopy** A tuned IR beam was overlapped with a visible beam in a second-order nonlinear optical process. These two input beams were spatially and temporally superimposed to produce an output beam of frequency equal to the sum of the IR and visible beam frequencies, which satisfied momentum and energy conservation. The occurrence of both Raman and IR active vibrational modes wherever symmetry is broken (e.g., surfaces and interfaces) enhances the SFG signal significantly. SFG spectra were collected with a mode-locked Nd:YAG laser (Leopard, Continuum, Santa Clara, CA) using a combination of *s*-polarized SFG and visible beams and *p*-polarized IR beam (*ssp* polarization), which is sensitive to upright symmetric vibrational modes and suitable for studying changes in the molecular orientations at the free surface and buried interface of the PHEMA films. SFG spectra for *ppp* and *sps* polarizations were also obtained but are not presented here for brevity. Data for each scan was obtained at 5 cm$^{-1}$ increments in the range of 2600-3200 cm$^{-1}$ using 100 shots per data point. The IR and visible intensities were used to normalize the SFG data. Details about the experimental set-up can be found elsewhere.[22]

Total internal reflection (TIR) geometry was used to obtain SFG spectra of the buried interface and free surface of the PHEMA films (Fig. 6-3). Because of the SFG dependence on the local electric field, the signal from the interface was enhanced by proper selection of the incident angle and refractive index of the prism material. Since the refractive index of most methacrylate polymers is close to that of calcium fluoride and less than that of sapphire (i.e., ~1.5 for polymers and calcium fluoride and ~1.8 for

sapphire at 532 nm), sensitivity inherent to different geometries and prism material was achieved in the SFG experiments. In view of the Fresnel enhancement due to the TIR of the green light and the attenuation of the IR through the PHEMA film, SFG signals were almost exclusively produced from the buried PHEMA/sapphire interface. This was confirmed by the identical SFG signals obtained with thick (>10 μm) and thin (<300 nm) PHEMA films. Regarding the PHEMA/air interface, a thinner film inhibits attenuation, while the Fresnel enhancement by the free surface in TIR/SFG spectroscopy intensifies the signal from the interface relative to the PHEMA/calcium fluoride interface. This was demonstrated by the disappearance of the SFG signal in the case of thick films.
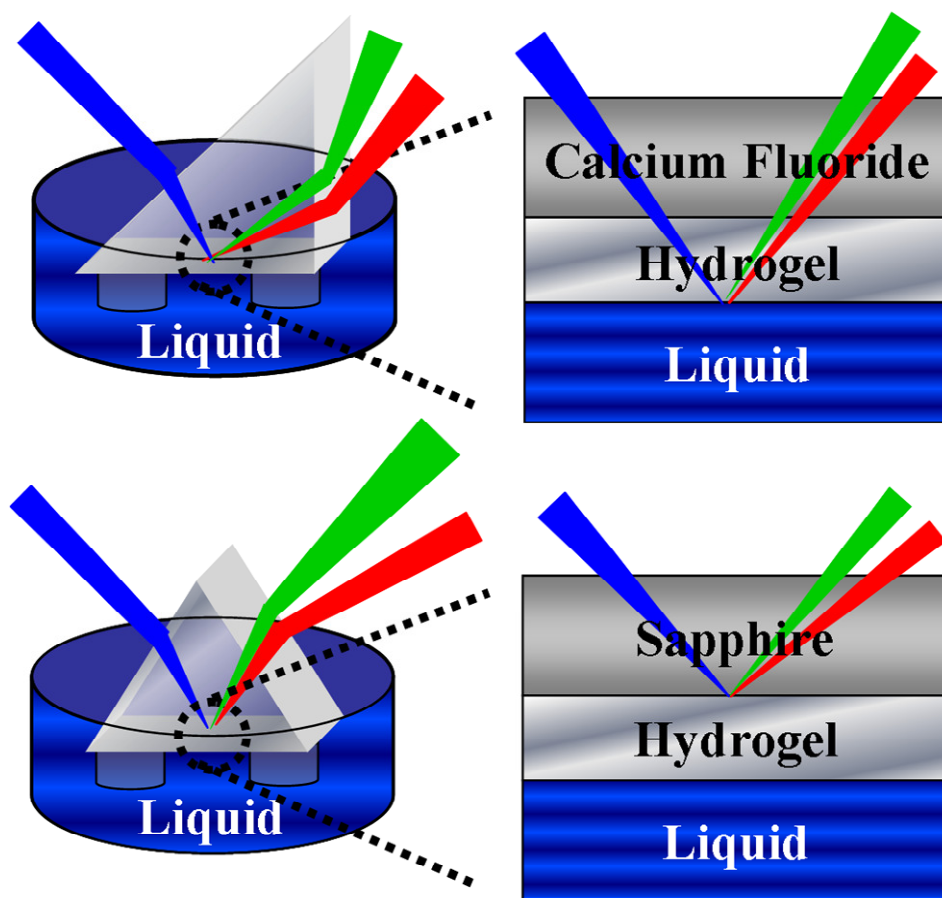


**Figure 6-3:** Schematic illustration of in situ SFG spectroscopy of PHEMA/liquid and PHEMA/sapphire interfaces.

The assignment of the vibrational modes was based on studies of the vibrational spectra of corresponding bulk polymers, selective deuteration of the functional groups, and *ab initio* calculations.[23,24,25,26] Although the peak positions are in accord with available resources, a cluster of four modes that produce SFG from 2935 cm$^{-1}$ to 2960 cm$^{-1}$ obscured the peak positions and shapes. Because the origins of the C–H stretches in the range of 2800–3000 cm$^{-1}$ are not obvious, the analysis of this region is cumbersome. Since the objective of this investigation was to study polymer conformational changes, deuterated solvents had to be used to remove the contributions of the OH peak interference from the water signal and the CH peak interference from the acetonitrile signal.

## 6.3 Results and Discussion

**Free PHEMA/air and PHEMA/liquid interfaces.** Figure 6-4 shows that the SFG spectrum of the dry PHEMA/air interface exhibits strong features associated with the C–H stretches of the ester ethyl side chain, α-methyl side chain, and backbone methylene. Methylene groups of the ester ethyl side chain have vibrational modes for the symmetric stretch [HOCH$_2$(s)] at 2880 cm$^{-1}$ and the Fermi resonance at 2935 cm$^{-1}$. Due to the proximity of these groups to both the ester and the hydroxide functionalities, they are associated with the hydrophilic side chain. The α-methyl moiety is the hydrophobic side chain, and the symmetric and two asymmetric stretches of the α-methyl group [CH$_3$(s) and two CH$_3$(a)] are visible at 2935, 2960, and 3000 cm$^{-1}$, respectively.[9] The backbone methylene exhibits vibrational modes for the symmetric stretch [CH$_2$(s)] at 2855 cm$^{-1}$ and

the Fermi resonance at 2915 cm$^{-1}$.[27] The SFG spectrum of the dry PHEMA/air interface reveals the presence of ordered CH groups at the surface, possibly due to surface energy (minimization of interfacial tension or enthalpic driving factors through rearrangement of hydrophobic and hydrophilic groups) and/or steric (chain-chain interactions) effects. The difference between hydrophobic group orientation at air and water interfaces is large. The hydrophobic α-methyl CH$_3$(s) and backbone CH$_2$(s) peaks dominate the dry PHEMA surface and the C$_3$ and C$_2$ rotation axes are mainly normal to the surface plane. Similar to previous results, the dominance of the backbone CH$_2$(s) peak indicates that the polymer chains lay mostly flat on the dry PHEMA surface, and at ambient conditions (~30% relative humidity) the hydrophilic glycol-like side chain is fairly ordered in addition to the backbone and α-methyl moieties.
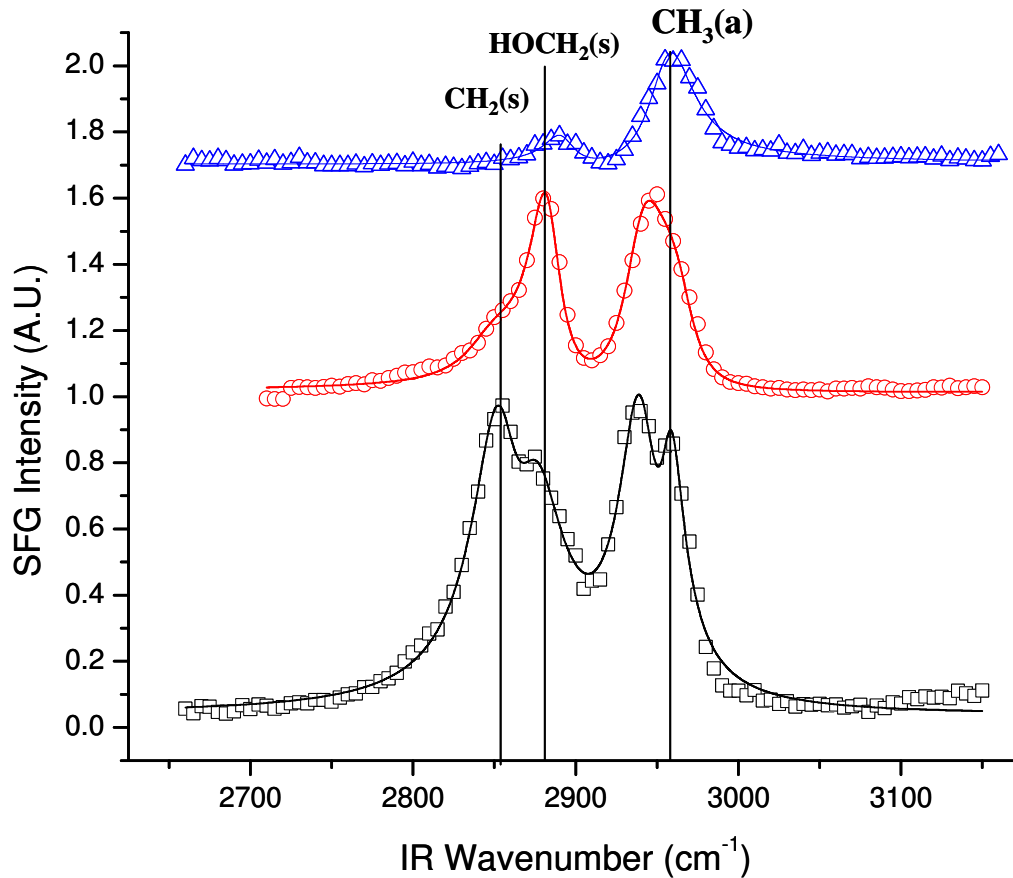
**Figure 6-4:** SFG spectra of the PHEMA/air interface obtained in *ssp* polarization combination: (□) dry and saturated with (○) $d_3$ACN and (Δ) $D_2O$. The spectra were offset for clarity.

Significant reconstruction of the free PHEMA surface occurred upon saturation with $D_2O$ and $d_3$ACN. Although the polymer must be in the rubbery state to change conformation upon contact with water and various solid surfaces,[28,29,30] chain mobility in a glassy polystyrene film in contact with a solvent vapor can occur as a result of the expanded chain conformation due to the solvent effect, which enables the polymer to

change orientation.[31] Since the SFG measurements were collected at room temperature, i.e., well below the glass transition temperature of PHEMA, they provide evidence that the surface plasticizing effects of $D_2O$ and $d_3ACN$ promoted chain mobility, leading to polymer restructuring at the surface. It is possible that surface roughening (net ordering decreases) and molecular reorientation to optimize favorable interactions affected the signal intensity from the liquid-saturated PHEMA surface. It has been shown that restructuring at a polystyrene surface depends strongly on the hydrophilicity (or hydrophobicity) of the contacting liquid or solid.[15] It was also found that liquids of high surface energy (e.g., >60 mN/m) reduced the overall SFG intensity from the polystyrene surface as a result of liquid-induced morphology changes and hydrogen bond interactions.

The $CH_2(s)$ intensities associated with the backbone and the glycol-like side chain decreased significantly for $d_3ACN$ and altogether disappeared for $D_2O$ (Fig. 6-4). While only a small $OHCH_2(s)$ peak from the hydrophilic side chain was discernible in the spectrum of the PHEMA saturated with $D_2O$, the PHEMA surface soaked into $d_3ACN$ demonstrated relatively less reconstruction of this hydrophilic group. A small peak at ~2935 cm$^{-1}$ assigned to the α-methyl $CH_3(s)$ was measured for PHEMA submerged in $d_3ACN$, while the absence of a peak in the case of $D_2O$ saturation indicated less ordering. This suggests that the amphiphilic nature of $d_3ACN$ prompted less restructuring of the hydrophobic backbone and α-methyl side chain. The hydrogen-bonding network, including both the hydroxide and the carbonyl, is expected to differ for each liquid. Similar to previous results that showed less polystyrene surface perturbation upon contact with alcohols,[15] it is believed that $d_3ACN$ oriented with its hydrophobic $CH_3$ group

toward the polymer, thus causing less reorientation of the hydrophobic PHEMA groups. The results of this study maintain this premise since the large $CH_3(s)$ peak of $d_3ACN$ dominates the SFG spectra of the $d_3ACN$-saturated PHEMA surface when the per-protonated analog is used (not shown for brevity). In addition, interactions between the PHEMA hydrophilic groups and the liquid might have caused tilting of proximal CH moieties to enhance the formation of hydrogen bonds. Interestingly, it appears that PHEMA accommodated $d_3ACN$ more easily without causing as many groups to disorder upon restructuring.

**Buried dry and saturated PHEMA/solid interface**. The PHEMA/sapphire and PHEMA/liquid interfaces are unique in that the polymer flexibility is hindered by a rigid barrier at the buried sapphire interface. This system was also chosen to enable the simultaneous study of liquid incorporation into a gel at both hydrophobic (PHEMA/air) and hydrophilic (PHEMA/sapphire) interfaces. Both $d_3ACN$ and $D_2O$ signals could be measured at the buried interface, while the PHEMA signal did not disappear and the films remained adhered to the sapphire surface. Although the hydrophilic sapphire surface promotes moisture accumulation that intensifies the signal from the buried interface, SFG is sensitive to ordering within the electric field penetration depth and, hence, the polymer signal could be obtained even in the presence of a thin liquid layer at the PHEMA/sapphire interface. In the case of $D_2O$ solvent, this ordered liquid film, whether co-adsorbed to the oxide with the polymer or incorporated into sapphire functionalities (i.e., AlOH groups), provides a nonresonant background that interferes with the CH signal. The resulting fit yielded a phase difference of $\sim\pi/2$, consistent with previous results.[32]

119
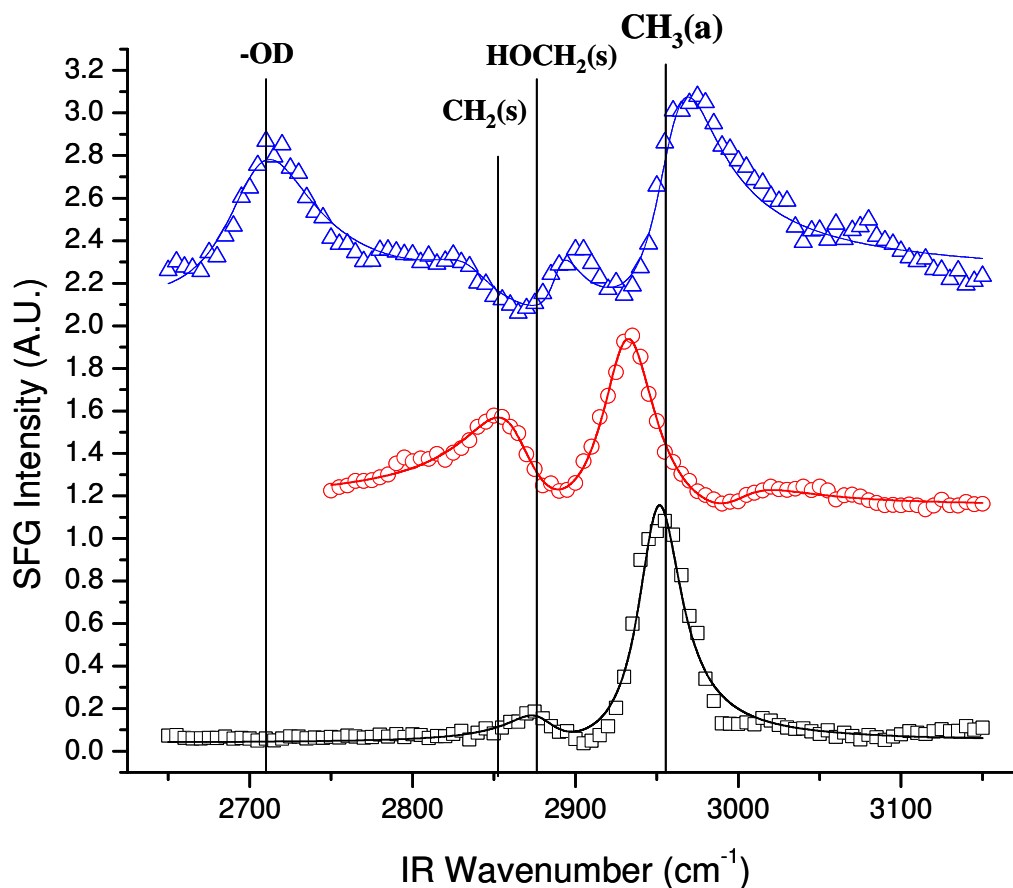
**Figure 6-5:** SFG spectra of the PHEMA/sapphire interface obtained in *ssp* polarization combination: (□) dry and saturated with (○) d₃ACN and (Δ) D₂O. The spectra were offset for clarity.

Fig. 6-5 shows SFG spectra of the PHEMA/sapphire buried interface. The spectrum of the dry PHEMA/sapphire interface is nearly identical to that of the PHEMA surface saturated with D₂O (Fig. 6-4). The former spectrum indicates that the α-methyl side chains are tilted and that a small OHCH₂(s) peak occurs at 2880 cm⁻¹, which is attributed to the glycol-like side chain. In accord with previous data for hydrophilic

120

buried interfaces,[33] the equilibrium conformation is influenced by the surface energy of the solid surface or the liquid, and the polymer adapts a chain configuration to interact favorably.

Diffusion of $d_3$ACN and $D_2O$ through the ~300-nm-thick PHEMA films occurred within <1 s, and the spectra did not change during the SFG experiments (<1 h). The solvent was ordered at the buried interface, and large signature peaks were measured, such as $CD_3$ stretch of $d_3$ACN (not shown) and OD stretch of $D_2O$ or surface OH species. Extensive reconstruction occurred at the buried interface upon submersion in $d_3$ACN. Both the $HOCH_2$(s) from the glycol-like side chain and the $CH_3$(a) from the α-methyl side chain disappeared upon the emergence of the $CH_2$(s) peak from the backbone and the $CH_3$(s) peak from the α-methyl side. This implies that even in contact with a hydrophilic surface like sapphire, the amphiphilic nature of $d_3$ACN promoted ordering of the hydrophobic side chain and backbone of the polymer. It has been observed that $d_3$ACN orders against zirconia and alumina surfaces with the CN group oriented toward the solid surface.[34] This would necessitate that the opposed $CH_3$ groups of the PHEMA orient away from the hydrophilic solid surface, essentially creating a passivating layer. The glycol-like moiety appears completely disordered, as evidenced by the absence of any measurable intensity. Since $D_2O$ possesses higher surface tension and lacks the amphiphilic nature of $d_3$ACN, the PHEMA conformation did not change at the buried sapphire interface upon saturation of the film with the $D_2O$ solvent.

## 6.4 Conclusion

Well-defined and ordered interfaces are formed between immiscible polymer-liquid(vapor) pairs, and both the polymer and the liquid/vapor components can exhibit ordering. This chapter focused on miscible swelling gels, and an exploration of the molecular changes occurring at the PHEMA free surface and buried interface with sapphire under conditions of dry air and saturation by different liquids. The conformational changes resulting from the submersion of PHEMA in $d_3$ACN and $D_2O$ were affected by the surface tension and hydrogen bonding of each solvent. Each liquid was incorporated into the PHEMA film and an ordered layer formed at the sapphire interface. While PHEMA reconstruction upon saturation with $D_2O$ was not observed at the buried interface, the amphiphilic nature of $d_3$ACN promoted reorientation of the polymer hydrophobic groups toward the hydrophilic sapphire surface. The findings of this study demonstrate that infrared-visible SFG vibrational spectroscopy is an effective technique for examining in situ polymer surface restructuring at both buried and free interfaces due to chemical and environmental effects.

## References

[1] Israelachvili, J. *Intermolecular and Surface Forces, 2nd Edition*, Academic Press Inc., **1992**.

[2] Fadeev, A.Y.; McCarthy, T.J. *Langmuir*, **1999**, *15*, 3759.

[3] Lam, C.N.C.; Wu, R.; Li, D.; Hair, M.L.; Neumann, A.W. *Adv. Coll. & Int. Sci.,* **2002***, 96,* 169.

[4] Chen, Z.; Shen, Y.R.; Somorjai, G.A. *Ann. Rev. of Phys. Chem.*, **2002**, *53*, 437.

[5] Opdahl, A.; Phillips, R.A.; Somorjai, G.A. *J. Phys. Chem B*, **2002**, *106***,** 5212.

[6] Wang, J.; Chen, C.; Buck, S.M.; Chen, Z. *J. Phys. Chem. B*, **2001**, *105*, 12118.

[7] Zhang, D.; Dougal, S.M.; Yeganeh, M.S. *Langmuir*, **2000**, *16*, 4528.

[8] Gautam, K.S.; Schwab, A.D.; Dhinojwala, A.; Zhang, D.; Dougal, S.M.; Yeganeh, M.S. *Phys. Rev. Lett.*, **2000**, *85*, 3854.

[9] Briggman, K.A.; Stephenson, J.C.; Wallace, W.E.; Richter, L.J. *J. Phys.Chem. B*, **2001**, *105*, 2785.

[10] Oh-e, M.; Hong, S.C.; Shen, Y.R. *Appl. Phys. Lett*., **2002**, *80*, 784.

[11] Mansfield, K.F.; Theodorou, D.N. *Macromolecules*, **1991**, *24*, 6283.

[12] Clancy, T.C.; Hwan Jang, J.; Dhinojwala, A.; Mattice, W.L. *J. Phys. Chem. B,* **2001**, *105*, 11493.

[13] Harp, G.P.; Gautam, K.S.; Dhinojwala, A. *J. Amer. Chem. Soc.*, **2002**, *124*, 7908.

[14] Wilson, P.T.; Richter, L.J.; Wallace, W.E.; Briggman, K.A.; Stephenson, J.C. *Chem. Phys. Lett.*, **2002**, *363*, 161.

[15] Ide, M., Mori, T., Ichikawa, K., Kitano, H., Tanaka, M., Mochizuki, A., Oshiyama, H., and Mizuno, W. *Langmuir* **2003,** *19*, 429.

[16] Kee, H. B., Jhon, M. S., and Andrade, J. D., *J. Col. And Int. Sci.* **1975**, *51*, 225.

[17] Hannon, T. E., Chah, S., and Zare, R. N. *J. Phys. Chem.* B **2005,** *109*, 7435.

[18] Bieze, T. W., Barnes, N., Huige, A. C., Enderby, C. J. M., Leyte, J. C. *J. Phys. Chem.* **1994**, *98*, 6568.

[19] Chen, Q., Zhang, D., Somorjai, G. A., and Bertozzi, C. R. *J. Am. Chem. Soc*. **1999**, *121*, 446.

[20] Sassi, A. P., Lee, S. H., Yong, H. W., Blanch, H. W., and Prausnitz, J. M. *J. Appl. Poly. Sci*. **1996**, *60*, 225.

[21] Vogt, B. D., Prabhu, V. M., Soles, C. L., Satija, S. K., Lin, E. K., and W. Wu, *Langmuir* **2005**, *20*, 2460.

[22] Kweskin, S. J., Komvopoulos, K., and Somorjai, G. A., *J. Phys. Chem. B* **2005**, 109, 23415.

[23] Schneider, B., Stokr, J., Schmidt, P., Mihailov, M., Dirlikov, S., and Peeva, N. *Polymer* **1979**, 20, 705.

[24] Faria, M. D. G., Teixeira-Dias, J. J. C., and Fausto, R. *Vibr. Spect.* **1991**, *2*, 43.

[25] Ferreira, L., Vidal, M. M., and Gil, M.H., Int. J. *Pharmaceutics* **2000**, *194*, 169.

[26] Wang, J., Chen, C., Buck, S. M., and Chen, Z. *J. Phys. Chem. B* **2001**, *105*, 12118.

[27] Lu, R., Gan, W., Wu, B., Zhang, Z., Guo, Y., and Wang, H. J. *Phys. Chem. B* **2005**, *109*, 14118.

[28] Yang, C. S. C., Wilson, P. T., and Richter, L. J., *Macromolecules* **2004**, *38*, 7742.

[29] Wang, J., Woodcock, S. E., Buck, S. M., Chen, C., and Chen, Z. *J. Am. Chem. Soc.* **2001**, *123*, 9470.

[30] Kweskin, S. J., Komvopoulos, K., and Somorjai, G. A., *Langmuir* **2005**, *21*, 3647.

[31] Opdahl A., and Somorjai, G. A. *Langmuir* **2002**, *18*, 9409.

[32] Becraft, K. A., Moore, F. G., and Richmond, G. L., *J. Phys. Chem. B* **2003**, *107*, 3675.

[33] Gautam, K. S., Schwab, A. D., Dhinojwala, A., Zhang, D., Dougal, S. M., and Yeganeh, M. S. *Phys. Rev. Lett.* **2000**, *85*, 3854.

[34] Hatch, S. R., Polizzotti, R. S., Dougal, S., and Rabinowitz, P., *J. Vac. Sci. Techol.* A **1993**, 11, 2232.

# Chapter 7

# Dynamic state of moisture at acrylate hydrogels interfaces and bulk hydration effects

## 7.1 Introduction

This chapter investigates the presence of ordered hydroxyl groups at a hydrogel interface and a hydrophilic surface boundary. The dramatic effect of bulk water content is explored at the edge of a gel. By varying the strength of the polymer-polymer interactions (chain entanglement, hydrogen bonding and van der Waals interactions), the structured water at the oxide/polymer interface is measured by sum frequency generation (SFG) vibrational spectroscopy. This nonlinear optical technique is used to probe the interfacial response of edge water to changes in the bulk water content (modification of hydrophobicity of the hydrogel and urea interaction). Finally, as evidence of the SFG sensitivity, the drying of the film is presented. A central finding of this study is that the ordered-water signal from the interface of a hydrated gel and sapphire is influenced by the bulk water content. Additionally, diffusion across an interface or "edge effects" during drying of the polymer exhibits a linear rate corroborating Fickian-like dynamics.

This chapter provides insight on how the water content of a hydrophilic interface with a gel surface can be measured and correlated to the bulk properties.

Hydrogel soft (gas permeable) contact lenses have been used for over 30 years. In spite of the many advances that have been made to improve the comfort and biocompatibility of contact lenses, the interfacial properties of contact lenses are not well understood. An example is the hydration state of the surface region of a contact lens.[1] It is commonly observed that the bulk water content affects both the oxygen permeability and the mechanical properties of the lens. Consequently, the overall comfort of the lens is affected.[2] It is believed that high water content at the contact lens surface and surface hydrophilicity are desirable properties for enhancing the wettability of tear films.[3] Many strategies have been developed to increase the surface hydrophilicity;[2] however, measurements of the water content of the surface region have not been made and the significance of the water concentration at the surface, relative to the bulk water content, has not been understood thoroughly. Furthermore, there exists no metric for actual comfort. It seems that the engineering of contact lenses has been largely based on trial and error approaches.

Recent advances indicate that a thin film or surface treatment applied to a contact lens may increase comfort. The surface water content is particularly important to the comfort of contact lenses, where oxygen permeability increases with the bulk water content.[2] These types of lenses tend to dehydrate when the tear film breaks up on the eye,[4] and relationship between the air humidity and bulk water content can lead to surface dehydration causing discomfort. The water content of the near-surface region also affects the surface mechanical properties including the viscoelastic and friction properties of

poly(2-hydroxyethyl methacrylate) (PHEMA), which is a rigid and glassy polymer in its dry state but soft and flexible in its fully hydrated state. Fig. 7-1 shows the AFM-derived stiffness for the approach and the retract rate for a PHEMA film exposed to various humidities. The loading curve slope contains contributions from both elastic and viscous deformation, while the unloading curve slope contains mainly elastic contributions.[5] The loading curve slope of the bulk-hydrated decreases and has a strong dependence on probing rate at high humidity, indicating an increased presence of water in the surface region. The measurement of the viscous component has a strong time dependence associated with it, whereas the contact lens elastic strain and cantilever bending have little or no time dependence.[6] Hydrogels have received much attention primarily due to this dynamic behavior.
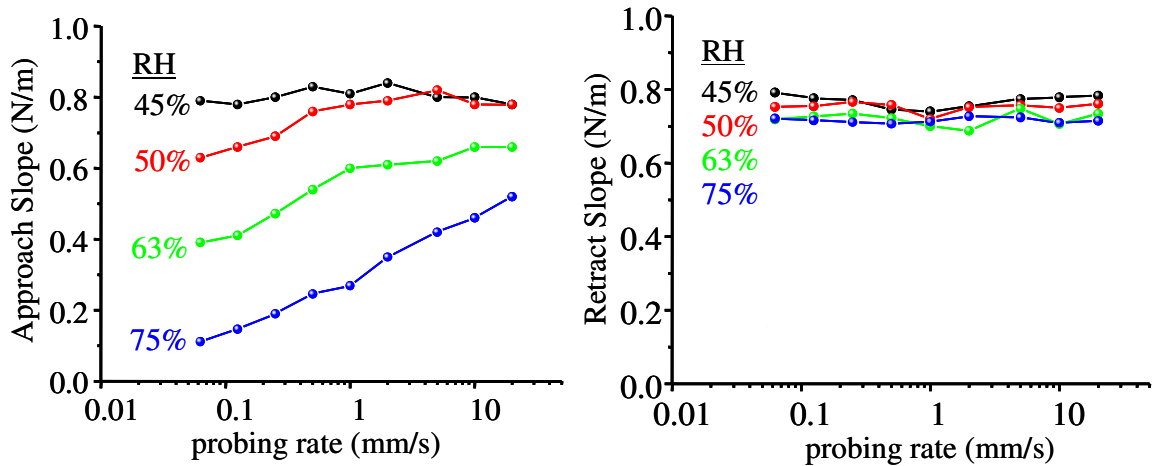


**Figure 7-1:**. Comparison of the loading curve slopes and unloading curve slopes for the bulk-hydrated lens and the bulk dehydrated lens collected at various probing rates and humidity (1N/m cantilever).

Recent FTIR studies by Kitano et. al. [7] on hydrogen bonding near the surface of PHEMA have shown that the surface chemical structure may vary from the bulk. In the

present study, direct molecular-level information was obtained during the interaction between polymer hydrogels and water in contact with a hydrophilic surface. This was accomplished by sum frequency generation (SFG) vibrational spectroscopy, which is an effective experimental technique capable of providing molecular structure information at buried hydrogel interfaces.[8] In this chapter interfacial water of various hydrogels with three different bulk water contents is studied at the buried interface. The behavior of gels and changes in the SFG intensity due to the water are investigated by comparing saturated and dry films. It is demonstrated that SFG can effectively probe the moisture at the buried sapphire/hydrogel interface.

## 7.2 Experimental procedures

**Polymer films.** Specimens were fabricated from pellets of commercially available polymers of given molecular weight $M_w$ and glass transition temperature $T_g$, namely: Poly(2-hydroxyethyl methacrylate) (PHEMA $M_w = 300000$, $T_g \approx$ ℃, Aldrich, St. Louis, MO), Poly(2-hyroxypropyl methacrylate) (PHPMA $M_w = 20000$, $T_g \approx$ ℃, Aldrich, St. Louis, MO). The chemical structure of the polymers is shown in Fig. 7-2. Polymer films were spin cast at 3000 rpm directly onto sapphire substrates from a d5-pyradine solution and annealed at 70 ℃ for 12 hours.
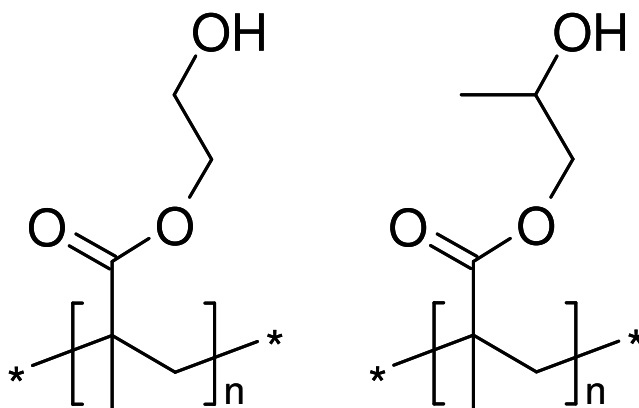
**Figure 7-2:** Molecular structure of poly(2-hydoxyethyl methacrylate) (PHEMA) and poly(2-hydroxypropyl methacrylate) (PHPMA).

The sapphire prisms consisted of synthetic single-crystal sapphire ($\alpha$-Al$_2$O$_3$) possessing a root-mean-square roughness of 5-10 nm (Red Optronics, Mountain View, CA) with optical ĉ-axis perpendicular to the free surface. The flatness of the sapphire and polymer surfaces and the surface composition were examined with an atomic force microscope (AFM) fitted with an M5 head (Park Scientific Instruments, Sunnyvale, CA) and X-ray photoelectron spectroscopy (XPS) spectrometer (PHI 5300, Perkin-Elmer, Boston, MA), respectively. AFM surface mapping confirmed the flatness of the contacting surfaces, while the XPS provided information about the chemical composition and the absence of surface contaminants. The sapphire prisms were cleaned in aqua regia (nitric and hydrochloric acid), rinsed thoroughly in high-purity water, and, finally, exposed to UV-initiated ozone for at least an hour. The substrates were used immediately after cleaning to minimize contamination from the atmosphere.

**SFG vibrational spectroscopy**. In SFG vibrational spectroscopy, a tuned infrared (IR) beam of frequency $\omega_{ir}$ is overlapped with a visible beam of frequency $\omega_{vis}$ in a

second-order nonlinear optical process. These two input beams are spatially and temporally superimposed to produce an output beam of sum frequency $\omega_s = \omega_{ir} + \omega_{vis}$ that satisfies momentum and energy conservation. The occurrence of vibrational modes, which are both Raman and IR active and exist where symmetry is broken, enhances the SFG signal significantly. One polarization combination of input-output laser beams was used to obtain the SFG spectra, i.e., $p_{sfg}p_{vis}p_{ir}$, where $s$ and $p$ denote $s$- and $p$-polarized beams respectively, is presented. SFG spectra for $s_{sfg}s_{vis}p_{ir}$ and $s_{sfg}p_{vis}s_{ir}$ polarization combination were also obtained but are not presented here. The chosen polarization is most sensitive to OD stretches. Hereafter, the above polarization will be referred to as *ppp* for simplicity. This polarization combination provided a larger intensity at the buried polymer interface.  For each scan, data was obtained at increments of 5 cm$^{-1}$ in the range of 2600-3200 cm$^{-1}$ using 100 shots per data point. The SFG data were normalized by the IR and visible intensities.

The experimental setup is shown schematically in Fig. 7-3. Since the SFG intensity depends on the local electric field, the signal from the interface was enhanced by careful selection of the incident angle and refractive index of the substrate. Since the refractive index of most methacrylate polymers is less than that of sapphire (i.e., ~1.5 for polymers and ~1.8 for sapphire at 532 nm), sensitivity at the buried interface inherent to this geometries can be achieved. Regarding the polymer/sapphire interface, Fresnel enhancement due to the TIR of the green light and the attenuation of the IR through the polymer film thickness produced SFG signals almost exclusively from the buried interface. The identical SFG signals of thick (>10 μm) and thin (<300 nm) polymer films provided confirmation for the latter.
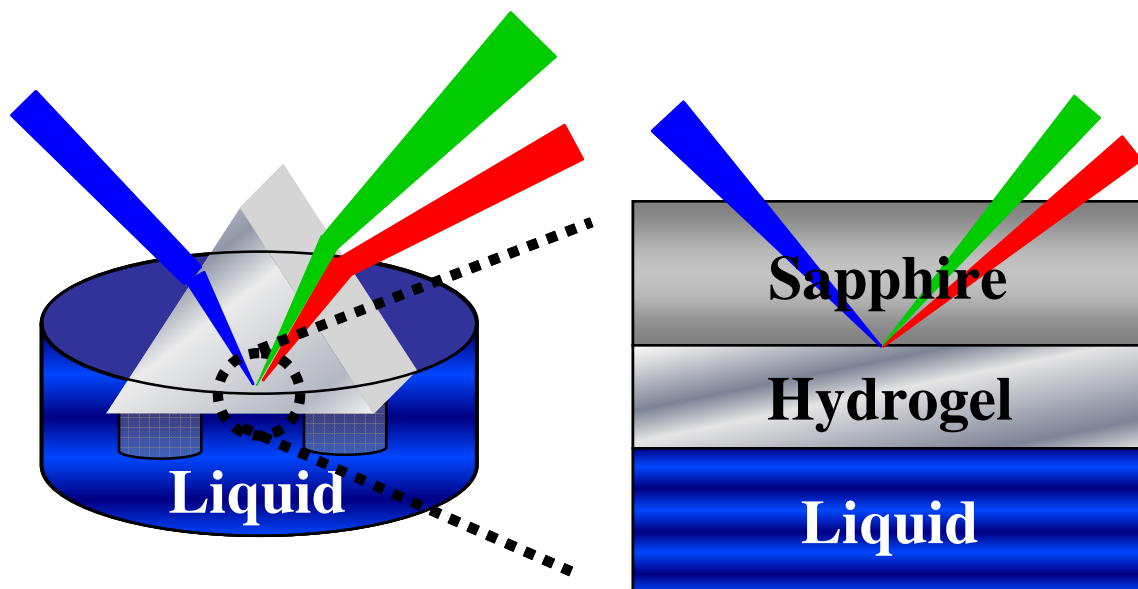
**Figure 7-3:** Schematic illustration of in situ SFG spectroscopy of hydrogel/sapphire interfaces.

## 7.3 Results

**PHEMA/Sapphire dry and in water**. The assignment of the vibrational modes was based on studies of the vibrational spectra of corresponding bulk polymers, selective deuteration of the functional groups, and *ab initio* calculations.[9,10,11,12] Although the peak positions are in accord with published data, a cluster of multiple modes that produce SFG from 2935 cm$^{-1}$ to 2960 cm$^{-1}$ obscured the peak positions and shapes. Briefly, the CH regions of the dry PHEMA/sapphire and PHPMA/sapphire interfaces exhibit strong features associated with C–H stretches of the ester side chain and α-methyl side chain (Fig. 7-4). CH$_2$ and CH$_3$ groups of the ester side chain have vibrational modes between 2880 cm$^{-1}$ and 2960 cm$^{-1}$. The α-methyl moiety is common to both polymer's hydrophobic side chain, and the symmetric and two asymmetric stretches of the α-methyl group [CH$_3$(s) and two CH$_3$(a)] are visible at 2935, 2960, and 3000 cm$^{-1}$, respectively.[9]

Further analysis has been performed for PHEMA in various environments in the previous chapter.[13]

Initially it is important to clarify that water signal can be measured at the buried interface while the polymer signal does not disappear. It is also necessary to report that the film stays intact and adhered to the sapphire throughout the experiments. Although the hydrophilic nature of the alumina surface causes moisture to accumulate, leading to an intense signal at the buried interface, SFG is sensitive to ordering within the electric field penetration depth. Therefore polymer signal can be measured even if there is a thin layer of liquid between the polymer and the sapphire. The ordered water molecules, whether coadsorbed to the sapphire and the polymer or bonded to the sapphire surface (-AlOH groups), provides a background signal in the case of water that interferes with the CH signal. The resulting fit of the saturated spectra reveals approximately $\pi/2$ phase difference, consistent with previous results.[14]
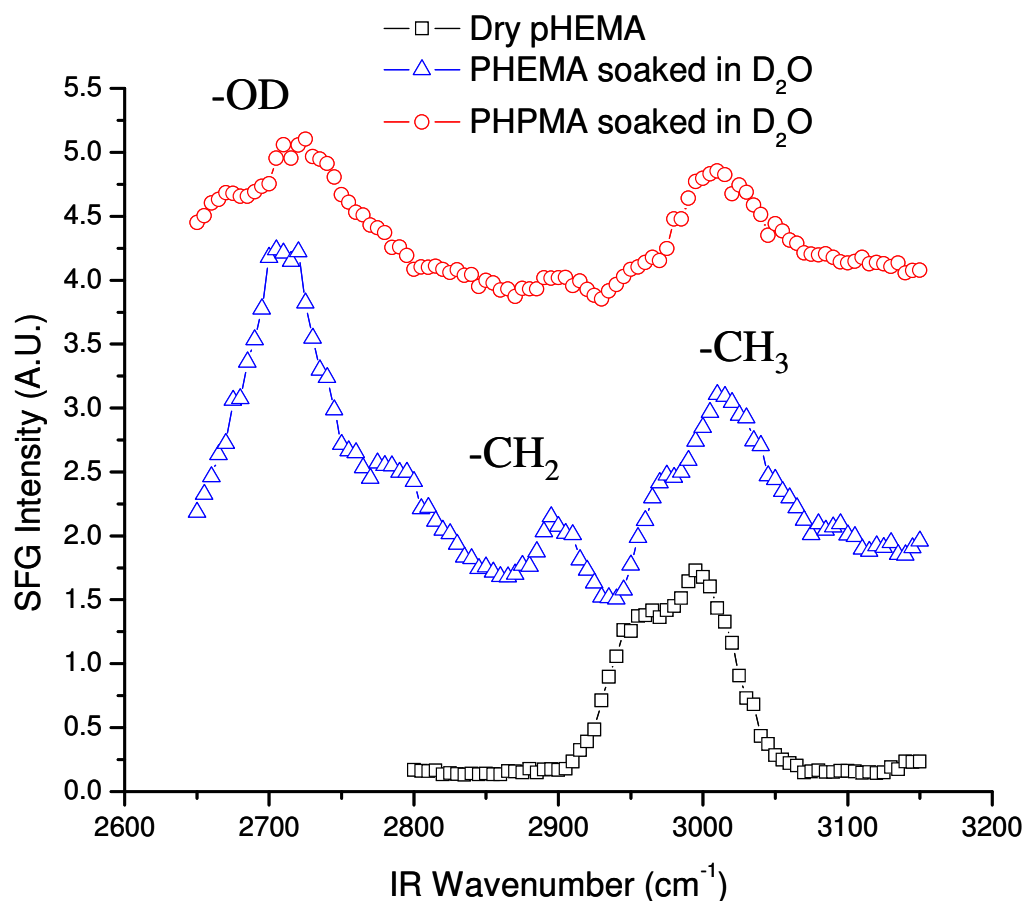
**Figure 7-4:** SFG spectra of the Hydrogel/sapphire interface obtained in *ppp* polarization combination: (□) dry PHEMA/sapphire, and D$_2$O saturated (Δ) PHEMA and (○)PHPMA (offset for clarity).

Identical SFG spectra were collected for the PHEMA/sapphire and PHPMA/sapphire dry interfaces (not shown). Fig. 7-4 shows a typical spectrum of the PHEMA/sapphire interface which includes strong features due to the C-H stretches of the ester ethyl side chain and the α-methyl side chain. Slight reconstruction of the PHEMA and PHPMA surface occurred upon contact with water. There is also a feature at 2880

cm$^{-1}$ that is most likely due to ordering of the ester side chain. The spectra of the dry and saturated PHEMA/sapphire interfaces have identical fit parameters for the features at 2935, and 2990, indicating that the α-methyl side chains do not significantly restructure in the presence of water. In accord with previous data for hydrophilic buried interfaces,[15] the equilibrium conformation is influenced by the surface energy of the solid surface or the liquid, and the polymer adapts a chain configuration to interact favorably with its environment. The polymer/solid is unique in that the flexibility allowed for the polymer to reptate is hindered by a rigid barrier at the buried interface.

A prominent peak emerges upon saturation of PHEMA and PHPMA in Fig. 7-4 due to the nonbonding -OD stretch (predominantly -AlOD species) at 2715 cm$^{-1}$ and some contribution by $D_2O$ at 2740 cm$^{-1}$ ("free OD").[16] Diffusion of $D_2O$ through the ~300-nm-thick hydrogel films occurred within <1 s, and the spectra did not change during the SFG experiments (<1 h). Water ordering at the buried interface is evidenced by the dominant OD stretch. The intensity of this feature dramatically changes due to the local environment at the buried interface. The peak intensity for the more hydrophobic PHPMA polymer is approximately 70% less. Albeit many factors can influence the intensity of this OD stretch, such as differences in interfacial bonding, molecular weight and conformation, the similar properties shared by these hydrogels generates a model system where the efficacy of the SFG technique to probe molecular rearrangement and the presence of trace amounts of water can be demonstrated and small chemical substitutions can be studied. The substitution of a propyl for an ethyl in the hydrogel decreases bulk water incorporation by approximately 90%.

Urea is known to disturb the intermolecular bonding in PHEMA and hence increases the water content. Fig.7-5 demonstrates that for a concentration of 0.01M urea, the characteristic -OD peak increases in intensity by a factor of 2. Again, the bulk concentration of water roughly correlates to the measured surface quantity of water. Variables likely to also influence the OD intensity are the changes in the α-methyl conformation as well as potential alumina surface charging. Even though it is essentially impossible to affect the bulk water content without potentially altering the interface properties as well, this system supports the study above, implicating a correlation between the two features.
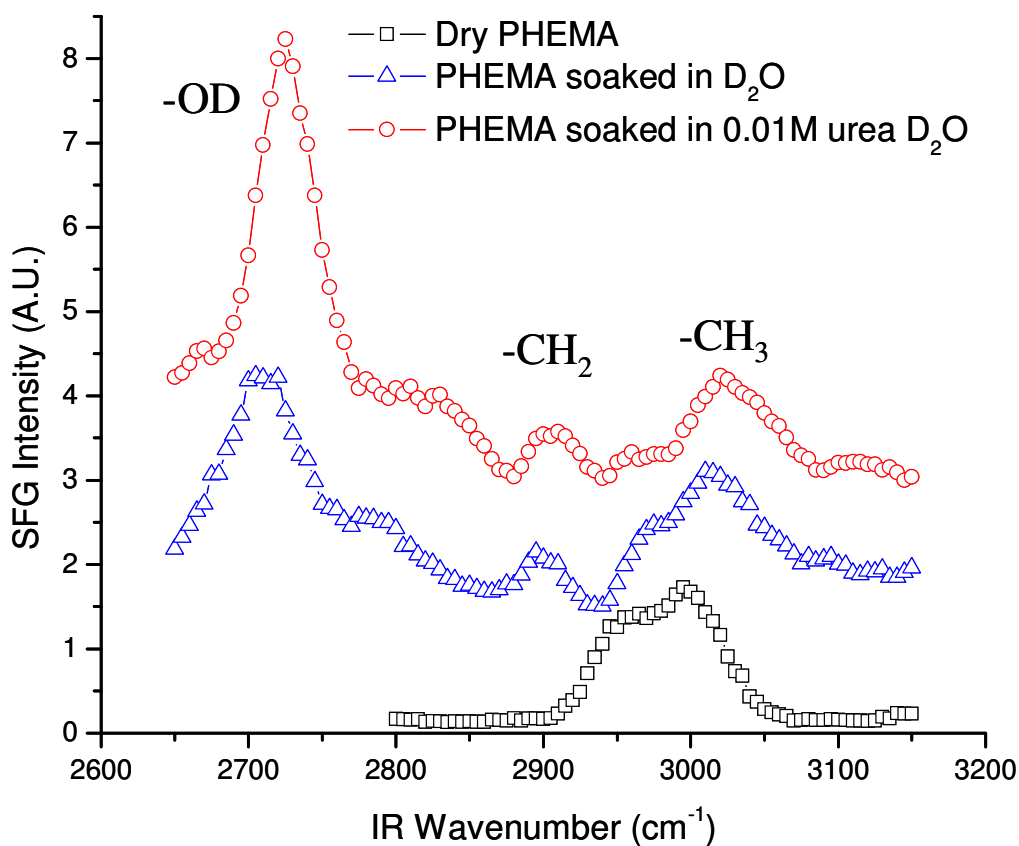
**Figure 7-5:** SFG spectra of the PHEMA/sapphire interface obtained in *ppp* polarization combination: (□) dry, $D_2O$ saturated (Δ) and (○).01M urea $D_2O$ PHEMA (offset for clarity).

SFG spectra were collected in a dynamic experiment by allowing a $D_2O$ saturated PHEMA film to dry in air. Fig. 7-6 shows spectra collected at 20 min intervals during drying. A significant decrease in the intensity of the –OD stretch occurred with the increase of time. The number density of SFG active molecules is proportional to the square root of the intensity. Alternately, instead of scanning across the wavenumber

range, Fig. 7-7 is collected while maintaining the IR probe wavelength at the -OD stretching frequency. Both figures reveal a linear decay of the -OD peak intensity as the film dries. A Fickian diffusion mechanism is expected for the bulk, but not necessarily for the surface. An exponential decay may occur if the competition for the surface associated water and bulk bound water were subject to distinct kinetics in a multistep transport. However, the parallel relationship with the bulk implies that a hydrophilic interface maintains a fixed ratio of surface water to bulk water even under a dynamic situation such as drying.
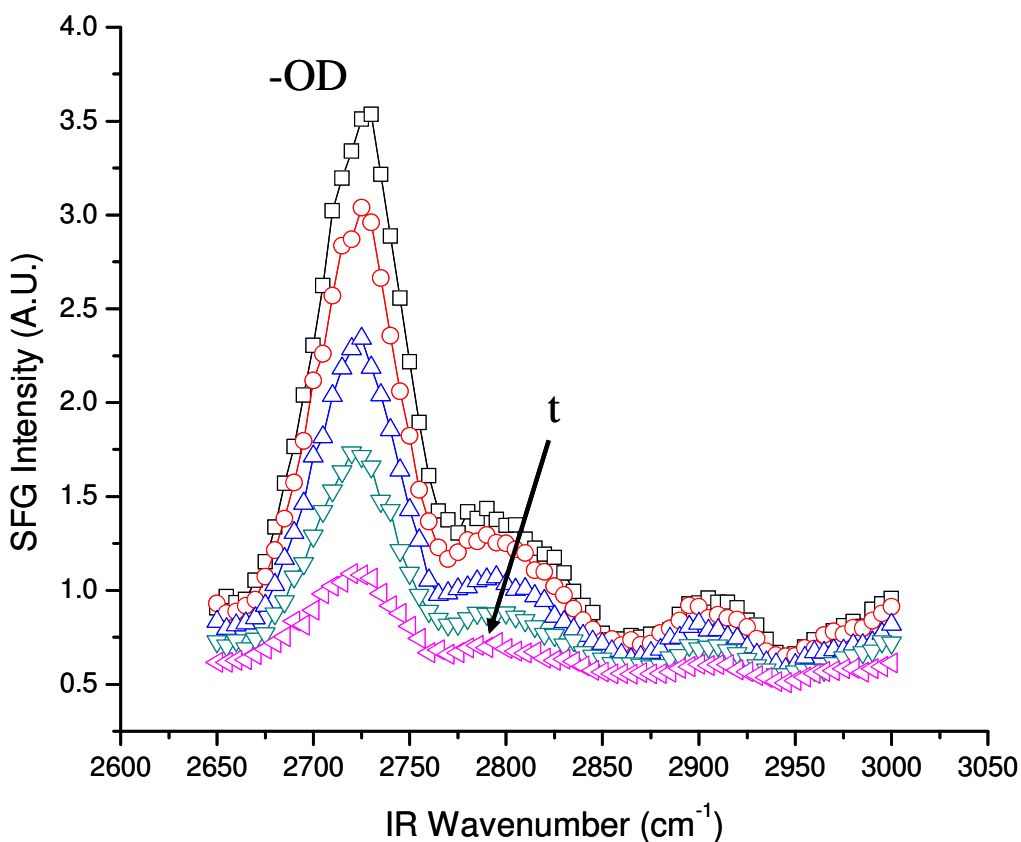


**Figure 7-6:** SFG spectra of the PHEMA/sapphire interface obtained in *ppp* polarization combination during drying of a $D_2O$ saturated film (scans obtained at 20 min. intervals).
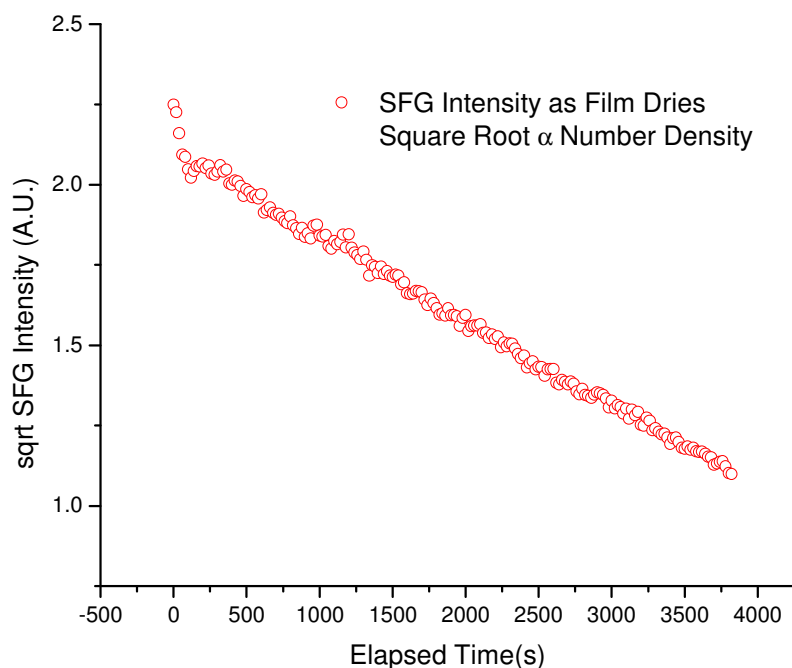
**Figure 7-7:** SFG intensity of the OD stretch at the PHEMA/sapphire interface obtained in *ppp* polarization combination obtained during drying of a D2O saturated film.

## 7.5 Conclusion

This study has revealed the existence of a correlation between the buried surface water quantity and the bulk water concentration. This might be due to the equilibrium between surface adsorbed water and internally hydrogen bonded water. The interactions between the hydrophilic alumina and the hydrophilic polymer groups are most likely competing for bonds. In this manner, removing the water from one reservoir (the bulk film) affects the other in turn. This has implications for the transport of water across polymer films. The surfaces of the polymer occupy a different configuration that might significantly disturb the bulk transport properties. The findings of this study demonstrate

that infrared-visible SFG vibrational spectroscopy is an effective technique for examining in situ polymer surface restructuring at hindered interfaces. This method proves to be a sensitive probe for the accumulation of moisture at the buried polymer/oxide interface and work is ongoing to explore these surface effects in practical applications, such as coatings and interfacial adhesion changes.

## References

[1] McConville, P.; and Pope, J.M. *Polymer*, **2001**, *42*, 3559.

[2] Lai, Y.C.; and Friends, G.D. *J. Biomed Mat Res*, **1997**, *35*, 349.

[3] Lopez-Alemany, A.; Compan, V.; and Refojo, M.F. *J. Biomed Mat Res (Appl Biomater)*, **2002**, *63*, 319.

[4] Pritchard, N.; and Fonn, D. *Opthal. Physiol. Opt.*, **1995**, *15*, 281.

[5] Opdahl A.; and Somorjai, G.A. *J. Polymer Science B-Polymer Physics*, **2001**, *39*, 2263.

[6] Ferry, J.D. *Viscoelastic properties of polymers*, 3rd edition, New York, Wiley, **1980**.

[7] M. Ide, T. Mori, K. Ichikawa, H. Kitano, M. Tanaka, A. Mochizuki, H.Oshiyama, and W. Mizuno, Langmuir **19**, 429 _2003_

[8] Kweskin, S.J., Komvopoulos, K., Somorjai, G.A. *Appl. Phys. Lett.*, **2006**, *88*, 134105.

[9]B. Schneider, J. Stokr, P. Schmidt, M. Mihailov, S. Dirlikov, and N. Peeva, Polymer **20**, 705 (1979).

[10]M. D. G. Faria, J. J. C. Teixeira-Dias, and R. Fausto, Vibr. Spect. **2**, 43 (1991).

[11] L. Ferreira, M. M. Vidal, and M.H. Gil, Int. J. Pharmaceutics **194**, 169 (2000).

[12] J. Wang, C. Chen, S. M. Buck, and Z. Chen, J. Phys. Chem. B **105**, 12118 (2001).

[13] Kweskin, S. J., Komvopoulos, K., and Somorjai, G. A., *Langmuir* **2005**, *21*, 3647.

[14] Becraft, K. A., Moore, F. G., and Richmond, G. L., *J. Phys. Chem. B* **2003**, *107*, 3675.

[15] K. S. Gautam, A. D. Schwab, A. Dhinojwala, D. Zhang, S. M. Dougal, and M. S. Yeganeh, Phys. Rev. Lett. **85**, 3854 (2000).

[16] P. B. Miranda, Lei Xu, Y. R. Shen, and M. Salmeron, Phys. Rev. Lett. **81**, 5876 (1998).

# Chapter 8

# Carbon monoxide oxidation on cubic platinum nanoparticles

## 8.1 Introduction

Extensive high vacuum and low pressure studies have been carried out to reveal the structure of carbon monoxide (CO) on transition metal surfaces and its bonding characteristics. Investigations have been carried out with low energy electron diffraction (LEED) surface crystallography[1,2,3] and both electronic[4,5] and vibrational[6] spectroscopy techniques. Based on numerous studies, a degree of structure sensitivity in reactions involving carbon monoxide (CO) has been observed on platinum.[7]

Pt (100) surfaces, albeit higher energy than (111) facets, have been shown to be highly mobile. When a Pt(100) single crystal is clean, the surface layer will reconstruct to form a psuedo-hexagonal (5x20) structure, closely resembling the Pt(111) surface structure.[8,9,10] If CO is allowed to adsorb on the surface, the Pt(100) surface will reconstruct back to the square (1x1) structure if the CO coverage is greater than 0.5 monolayers (ML).[11,12] The Somorjai group has observed the (5x20) surface

142

reconstruction with LEED. Upon the addition of 4L of CO, the LEED pattern indicates

that the surface becomes (1x1). If an SFG spectrum is taken of this system, a single CO

resonance at 2092 cm$^{-1}$ is observed. Fig. 8-1 (left) shows this resonance, which

corresponds to a (4x2) pattern of atop CO on the unreconstructed Pt(100) surface. If the

room temperature Pt(100) surface is exposed to 40 torr of CO, a single resonance at 2100

cm$^{-1}$ is observed (blue-shifted due to dipole-dipole coupling). This is shown in the

bottom spectrum in Fig. 8-1 (right). As the sample is gradually and sequentially heated

to 450 K, the resonance shifts to 2086 cm$^{-1}$.
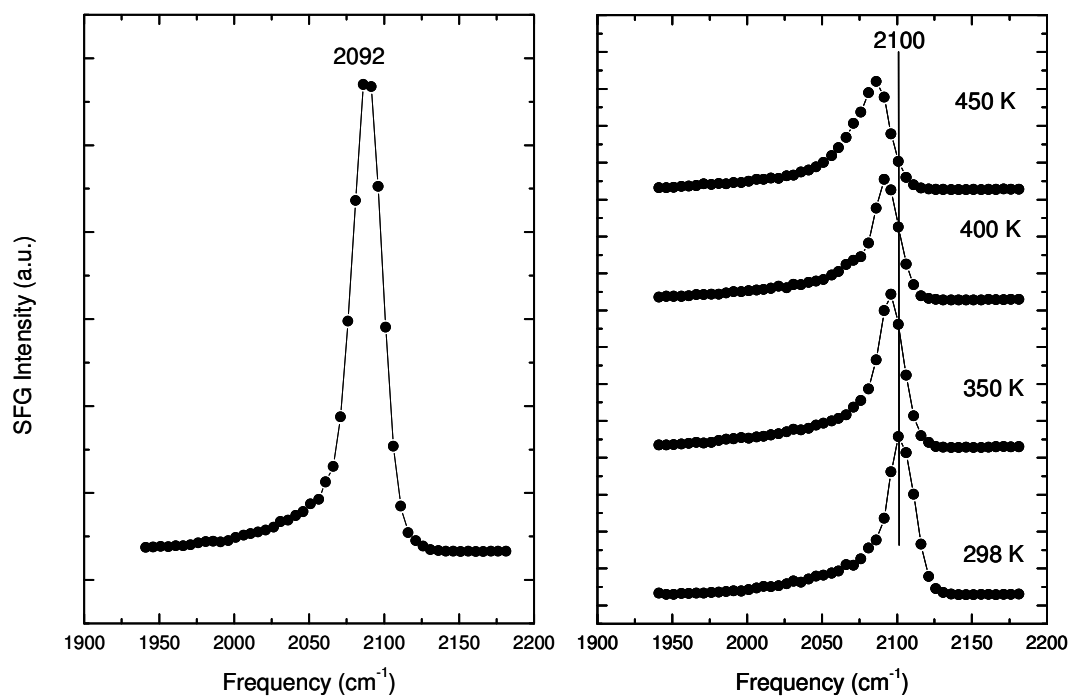


**Figure 8-1:** SFG spectrum collected in *ppp* of Pt(100) exposed to 4 Langmuirs of CO

(left). Pt(100) exposed to 40 torr of CO as the crystal is heated to successively higher

temperatures (right).[13]

In this chapter, we discuss the process of CO oxidation catalyzed by the Pt(100) crystal surface or nanoparticles. In this reaction, the following occurs:

$$CO + \tfrac{1}{2}O_2 \rightarrow CO_2 \qquad\qquad\qquad (8\text{-}1)$$

This reaction is the most studied, data is available in a variety of pressure regimes,[14,15,16,17] and has been the subject of numerous computer simulations.[18,19] The majority of these investigations have used platinum as the catalyst material. Platinum is used in most automobile catalytic converters, where it acts as an oxidation catalyst, converting CO to $CO_2$.

The CO oxidation reaction proceeds through various mechanisms depending on the temperature range. The low temperature regime is separated from the high temperature regime by the ignition point of the reaction. The ignition point depends mainly on the CO partial pressure[20] as well as the platinum surface structure. The reaction rate is generally slow below ignition, proceeding faster in the high temperature regime. In fact, at the ignition temperature, the reaction produces more heat than the system can dissipate, resulting in increasing catalyst temperatures and faster reaction rates.[21]

In the low temperature regime, it is believed that the reaction proceeds through a Langmuir-Hinshelwood mechanism.

$$CO_{(a)} + O_{(a)} \rightarrow CO_{2(g)} \qquad\qquad\qquad (8\text{-}2)$$

It is accepted that the platinum surface is primarily CO covered at low temperatures. The proposed reaction mechanism depends on atomically adsorbed oxygen. In order to make $O_{(a)}$, oxygen needs two sites to dissociatively adsorb on platinum. Therfore, a high CO

coverage will inhibit both the dissociation of oxygen and the subsequent rate of oxidation of CO.[4]

Above the ignition temperature, the surface is known to be primarily oxygen covered. Under these conditions, the reaction becomes mass transport limited, either by the rate of CO approaching the platinum surface from the gas phase or by the rate of $CO_2$ leaving the surface once it has been formed.

$$CO_{(g)} + O_{(a)} \rightarrow CO_{2(g)} \qquad\qquad (8\text{-}3)$$

Although the general behavior of the reaction is the same on all three crystal faces, the ignition temperature is much lower for the Pt(100) crystal face than it is for the Pt(111) and Pt(557) surfaces. Studies have found that the Pt(111) terrace sites are more involved in the CO oxidation reaction than step sites.[15,22,23] Comparing the CO dissociation temperature and the CO oxidation ignition temperature for three the platinum single crystal catalysts, the Pt(100) crystal has the lowest temperature for both processes.

Studies comparing single crystals and nanoparticles have demonstrated differences in the reactivity of terrace atoms and less coordinated surface atoms, such as those at steps and kinks[24,25,26.] Adsorption and reactions at corner and edge atoms, which are prevalent in nanoparticles but mostly absent from high coordination single-crystal surfaces like Pt(100) and Pt(111) can be significantly different from those on terrace atoms. An illustrative example is the faster dissociation of CO on highly stepped Rh(211) than Rh(111) by nine orders of magnitude due to the active sites on the step edges of Rh(211) that do not exist on Rh(111)[24]. Although studies on single crystals have produced valuable information for the surface kinetics, single crystals are not

representative of industrially relevant heterogeneous catalysts, such as small metal crystallites (1-10 nm) dispersed on high surface area oxides.

Recently, the so-called "materials gap" was bridged by using two-dimensional arrays of nanoparticles and nanowires synthesized on oxide surfaces by electron beam lithography[27] and size-reduction lithography.[28] These samples possess metal/oxide interfaces that enhance reactivity[29] and resist poisoning during catalysis.[30] However, catalysts fabricated by lithography are inherently difficult to produce because of the lengthy fabrication process, costly equipment, inability to obtain high-density structures, and the large size of the catalytic structures. To circumvent these limitations, alternative methods such as ultrahigh vacuum metal vapor deposition on oxide surfaces,[31] which generally produces planar nanoparticle catalysts with irregular-shaped particles of a broad size distribution, must be employed. Monolayer films of high density (i.e., $\sim 10^{11}$ cm$^{-2}$) Pt nanoparticles of well-defined shape and narrow size distribution have been produced on various oxide surfaces by the Langmuir-Blodgett method,[32] with the shape and size of the nanoparticles controlling the crystal facets exposed during the synthesis.

Since most commercial catalytic processes occur on nanoparticles under high pressures and elevated temperatures, in-situ techniques for studying the catalyst surface during the reaction process are of significant importance. Sum frequency generation (SFG) vibrational spectroscopy is a surface sensitive technique that has been successfully applied to various metal catalytic surfaces subjected to industrially relevant, high-pressure reaction conditions.[33] Bulk Pt is centrosymmetric and its contribution to the SFG signal is usually negligible. Since isotropic gases do not generate SFG, the SFG signal can only be produced from the metal surface and the adsorbates on that surface, making

SFG spectroscopy ideal for high-pressure conditions. Second-order nonlinear techniques have been primarily applied to flat substrates because of the ease of collection and analysis. However, most recently they have been used in studies of Pd nanoparticles vapor deposited on alumina[34] and solutions of submicrometer particles.[35]

The primary objective of this investigation was to characterize CO adsorption and oxidation on cubic Pt nanoparticles deposited on single-crystal sapphire by SFG in total internal reflection (TIR) geometry. This technique is nondestructive and provides sensitivity and specificity for the nanoparticle surface and adsorbate. Another objective was to determine whether a coherent SFG intensity can be obtained from nanoparticle sizes of less than 10 nm and if the signal would be sufficiently strong to monitor the reaction kinetics. Since the cubic Pt nanoparticles preferentially expose the (100) surface, the results can be directly compared with CO adsorption and oxidation on Pt(100) single crystals.

## 8.2 Experimental

**Synthesis and assembly of platinum nanoparticles.** Cubic Pt nanoparticles (face-to-face = $7.1 \pm 0.6$ nm and vertex-to-vertex = $9.4 \pm 0.6$ nm) were synthesized by a modified polyol process in the presence of poly(vinylpyrrolidone) (PVP) and $Ag^+$ ions. An amount of 2.5 mL of ethylene glycol (EG) was heated at reflux for 5 min, and 0.5 mL of $AgNO_3$ solution ($2 \times 10^{-3}$ M, Ag/Pt = 1.1 mol%) was added to the boiling EG. Subsequently, EG solutions of PVP (93.8 μL, 0.375 M) and $H_2PtCl_6 \cdot 6H_2O$ (46.9 μL, 0.0625 M) were added to the mixture every 30 s over a 16 min period. The resulting solution was heated for an additional 5 min. The products consisting of ~80% cubes and

~10% tetrahedra (9.8 ± 0.7 nm) were purified by repetitive precipitation-centrifugation and finally dispersed in chloroform. Elemental analysis performed by inductively coupled plasma-atomic emission spectroscopy showed that all Ag was incorporated into the Pt nanoparticles during the synthesis.[36] The location and state of the Ag associated with the Pt nanoparticles is currently unknown. However, since no detectable shifts were observed by synchrotron-based X-ray diffraction, the Ag was probably present on the surface as small clusters or isolated atoms. Ethylene hydrogenation rates on these materials suggest that 1 at.% Ag does not have a detrimental effect on olefin hydrogenation catalysis on cubic Pt silica-supported catalysts.[37] Previous studies have shown that pure Pt catalysts are ~50 times more active than a Pt-Ag catalyst with Pt/Ag molar ratio of 0.12,[38] where much of the surface was probably covered by Ag.

The Pt nanoparticles were assembled and deposited onto an equilateral single-crystal sapphire prism by the Langmuir-Blodgett (LB) technique (Fig. 8-2). Colloidal Pt solutions were dispersed onto deionized water (18 MΩ·cm) sub-phase on a LB trough (NIMA Technology, type 611) at room temperature. The surface pressure was monitored with a Wilhelmy plate and adjusted to zero before spreading the particles. The resulting surface layer was compressed by moving a mobile barrier at a rate of 0.3 cm$^2$/min. At a surface pressure of 6 mN/m, the Pt monolayer at the water-air interface was carefully transferred onto the sapphire surface using the Langmuir-Schäffer horizontal liftoff method. Measurements obtained with an atomic force microscope (AFM) (Park Scientific Instruments, Sunnyvale, CA) after scratching the surface with glass revealed a film thickness in the range of 10-11 nm. The obtained films were observed in a JEOL 200CX

transmission electron microscope (TEM) to determine the shape and size distribution of the Pt nanoparticles.
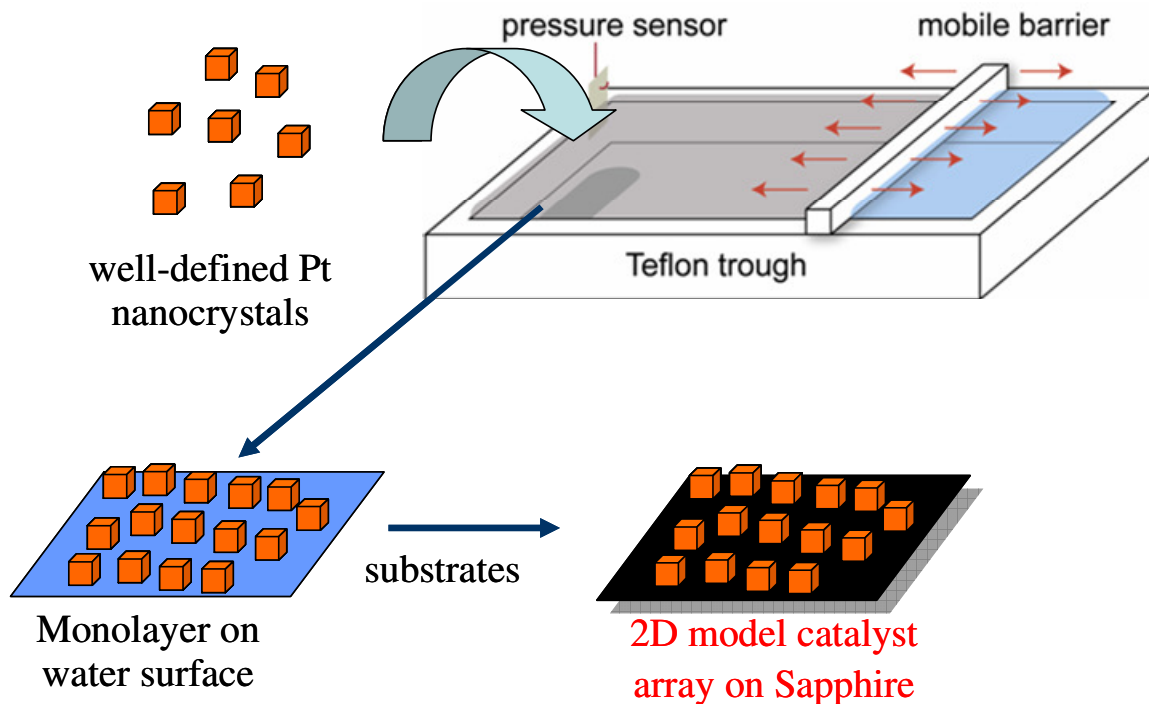


**Figure 8-2:** Schematic of the Langmuir-Schäffer horizontal liftoff method.

**Cell for in-situ monitoring of catalytic reactions.** A special cell was constructed for in-situ SFG spectroscopy in TIR geometry under continuous gas flow conditions (Fig. 8-3). An equilateral sapphire prism (Red Optronics, Mountainview, CA) was held in compression against a rubber O-ring by tightening a Teflon block fitted to the prism apex to the body of the cell by two set screws. The temperature at the prism surface was measured by a thermocouple placed directly on the sample. Heating was applied by two Kapton resistive elements on the sides of the prism (Omega Engineering, Inc., Stamford, CT). The temperature variations across the $20 \times 20$ mm base area of the prism were insignificant. The reaction cell was connected to a stainless steel tubing gas manifold of

diameter equal to 0.3175 cm, which was equipped with mass flow controllers (MFC, Porter Instrument Company) for precise delivery of the reactant gases, i.e., CO (AirGas, CP grade), $H_2$ (Praxair, UHP, 99.999%), He (Praxair, UHP, 99.999%), and 20% $O_2$/He mixture (Praxair, UHP, 99.999%), all used in the as-received condition. A vacuum of <1 mtorr was maintained in the reaction cell by mechanical and sorption pumps.
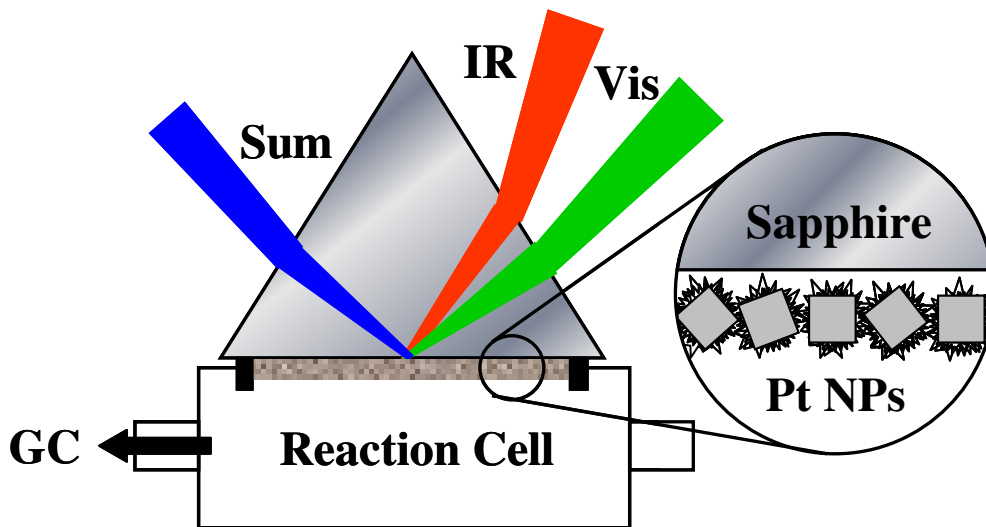


**Figure 8-3:** Schematic of the in-situ SFG reaction cell with a monolayer consisting of PVP-capped Pt nanoparticles. The spectroscopy cell operates as a flow or recirculating batch by flow controllers or a recirculation loop and pump. A gas chromatograph is directly incorporated in the loop to enable periodic sampling of the gas phase composition.

The aforementioned flow reactor was slightly modified for gas chromatography (GC) measurements. The cell was reconfigured as a 0.2 L batch reactor. A recirculation pump and a GC system (Hewlett Packard 5880A) were used to obtain a gas recirculation rate higher than 100 $cm^3$/min. The oxidation of CO was performed under excess oxygen conditions, i.e., 10 torr CO and 100 torr $O_2$. GC studies of the accumulation of $CO_2$ with

time were performed by injecting gas samples into a 20 ft long column (Carboxen 100) with 80/100 packing density. Initial reaction rates were determined from plots of $CO_2$ accumulation versus time. In view of the small total mass of Pt on the sapphire surface ($20 \times 20$ mm), the kinetic data were collected in batch mode. Depending on the reaction conditions, the accumulation of a sufficient amount of $CO_2$ for GC detection required times ranging from hours to days.

**Sum frequency generation vibrational spectroscopy.** SFG vibrational spectroscopy is ideal for studying the composition and conformational behavior at interfaces. SFG spectra were obtained with Nd:YAG laser (Leopard, Continuum, Santa Clara, CA) by combining a tunable infrared (IR) beam with 532 nm radiation at the sample interface at corresponding incident angles of 60° and 65° with respect to the surface normal. The variation of the incident angle produced a negligible effect on the measurements. A loosely focused area, IR energy of <10 µJ, and green energy of <50 µJ were used to minimize surface damage to the nanoparticles. For picosecond pulses, the damage threshold of metals is low. Pulses of incident IR energy above 10 µJ resulted in discoloration and signal degradation over the course of the experiment.

A significant enhancement of the SFG signal can be obtained with Raman and IR active vibrational modes generated where centrosymmetry is broken.[39] Due to the complicated nature of this system (e.g., dispersion and complex dielectric properties of the metal and nanoparticles) all data were collected at incident angles greater than the critical TIR angle by >15°. SFG results only for *ssp* polarization combination will be presented for brevity. Different polarization experiments were performed that mainly reflected the dielectric properties of the monolayer. For this system, the *ssp* polarization

combination signal provided the highest signal-to-noise ratio. A detailed description of the laser system used in this study can be found elsewhere.[40] Fig. 8-4 shows a photgraph of the optical setup for in-situ SFG characterization of well-ordered nanoparticle monolayers.
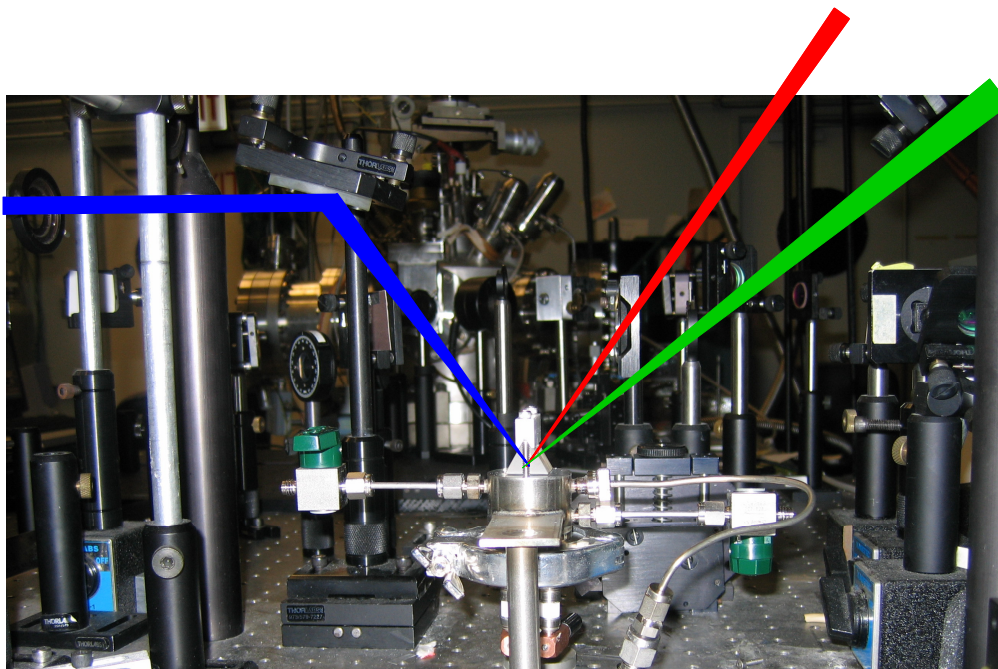


**Figure 8-4:** Photograph of the in-situ SFG reaction cell with a monolayer consisting of PVP-capped Pt nanoparticles.

Depending on the wavelength of the incident light, the scattering effect can be significant with rough surfaces. Rayleigh scattering and destructive interference for particle sizes less than the light wavelength complicates the detection of the SFG signal. Additionally, the orientation freedom of the cubic nanoparticles suggests that they are not necessarily isotropic at the sample surface. This also implies that the ensemble average for the system might show a disordered adsorbate structure. These obstacles were overcome by using an internal reflection element (i.e., sapphire prism). Sapphire shows

good transmission properties and good reflectivity from the interface of interest. Light scattering was not observed under the present experimental conditions. The TIR mode enhances the local fields and provides the additional benefit of signal intensification for centrosymmetric media. Since CO can adsorb on all the sides of the cubic nanoparticles, the inversion center would dramatically decrease the SFG intensity. It has been proposed that the exponential decay of the incident fields minimizes incoherent scattering and destructive interference.[41] Second harmonic Rayleigh scattering is unlikely because the SFG signal is collected in the direction of momentum conservation.

**Quartz crystal microbalance.** Experiments with a quartz crystal microbalance (QCM) were conducted under identical gas flow conditions using a QCM-D (Q-Sense) instrument (Fig. 8-5). By monitoring the change in the resonance frequency as a function of time, the mass change during gas flow was related to the adsorbed quantity. Samples of nanoparticles deposited on silica QCM discs, PVP spin-cast onto silica QCM discs, and Pt film vapor deposited onto a QCM disc were exposed to CO and the amount of irreversibly adsorbed CO was determined after purging with He gas.
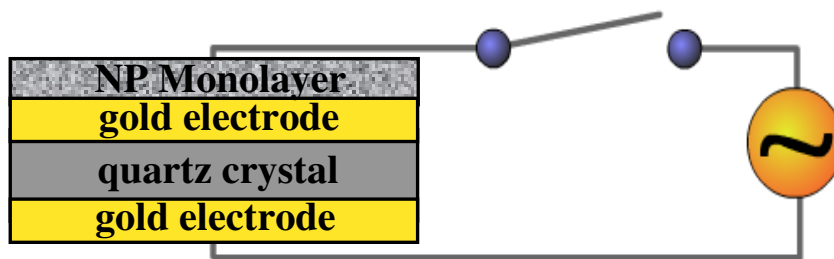


**Figure 8-5:** Schematic of the in-situ QCM reaction cell with a monolayer consisting of PVP-capped Pt nanoparticles.

## 8.3 Results and Discussion

**Synthesis and characterization of nanoparticle films.** The assembly of the same 7.1 nm cubic nanoparticles by LB methods has been reported previously.[31] Upon the deposition of a chloroform solution with cubic Pt nanoparticles on the water surface, the surface pressure increased due to the weakly bound PVP polymer. After lift-off at a surface tension of 6 mN/m, the surface coverage was determined to be 40%, which corresponds to a nanoparticle density of $\sim 7 \times 10^{11}$ $cm^{-2}$. The TEM and AFM images of the nanoparticles deposited on a TEM grid shown in Fig. 8-6 reveals uniform particle size and distribution. AFM imaging of a scratched film demonstrated the formation of a smooth film with the expected thickness. The nanoparticle size and film thickness respectively determined from the TEM and AFM measurements were used to estimate the thickness of the capping polymer. The film thickness measured with the AFM corresponds well with a 1-2 nm thick polymer coating on the 7.1 nm cubic nanoparticles. The evaporation of the chloroform did not affect the integrity of the monolayer. In fact, changes in the monolayer and nanoparticle shape could not be detected even after heating at 373 K in an oxygen atmosphere for 3 h. It has been reported that faceted Pt nanoparticles of comparable size begin to melt and their corners to round off upon heating at 623 K under vacuum conditions.[42]
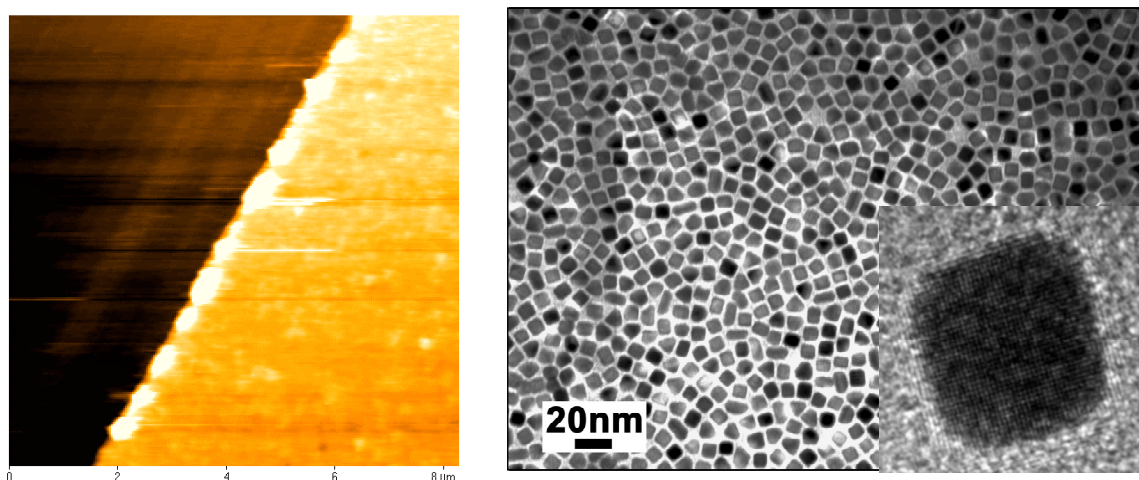
**Figure 8-6:** AFM (left) and TEM (right) images of a Langmuir-Schäffer monolayer consisting of PVP-capped Pt nanoparticles. The image shows that ~80% of the nanoparticles are cubes (high resolution inset on right) of 9.4 nm average size and ~10% tetrahedra of 9.8 nm average size.

**CO adsorption on polymer-covered and oxidized-reduced platinum nanoparticles.** The analysis of the SFG vibrational spectra of the sapphire/nanoparticle interface obtained in *ssp* polarization combination was based on published data. According to the literature, the linearly bound (atop) CO peak on Pt is between 2060 and 2100 cm$^{-1}$, depending on the cleanliness of the metal substrate,[43] surface coverage,[44] and coordination number of the Pt atoms.[45] Atop CO molecules bound to step edges are usually attributed to peaks between 2070 and 2080 cm$^{-1}$.[46] The effect of the residual PVP coating on the monolayer surface was investigated by SFG. After purging the spectroscopy cell with He gas to remove the oxygen and water vapor, SFG spectra of the as-deposited sapphire/nanoparticle sample were obtained at room temperature in the presence of flowing CO. Fig.8-7 shows a comparison between SFG spectra of CO

155

adsorbed on the surface of an as-deposited monolayer and a monolayer pretreated by heating at 373 K for 3 h in the presence of flowing $O_2$. A significant intensification of the atop CO peak and a shift toward higher frequencies resulted from the water removal and the decomposition of the PVP capping coating. Thermal gravimetric analysis has shown that oxidation at 373 K leads to the removal of a small fraction of PVP and all the hydrogen-bonded water and that the residual PVP can be completely decomposed by calcination in oxygen at temperatures above 623 K. Although the decomposition kinetics is slow, Pt catalyzes the oxidative decomposition of PVP.[47] In the present study, the samples were heated at a temperature well below 473 K because this is the temperature that PVP undergoes densification by crosslinking.[48] Hydrogen chemisorption measurements obtained at room temperature have shown that ~50% of the surface of PVP-stabilized Pt colloids in 1-butanol is free of PVP and capable of adsorbing CO.[49]

A comparison of the spectra shown in Figure 8-7 shows that the removal of water and/or PVP enhanced the CO peak intensity, most likely due to the increased availability of adsorption sites. The position of the absorption band also changed after oxidation, which may be due to less coupling of water and CO or more dipole-dipole coupling between neighboring CO molecules. Alternatively, a blue-shift of the atop CO peak has been reported for the adsorption of CO onto a metal surface covered by oxygen atoms relative to CO adsorption onto a clean surface of the same metal.[50,51] In addition, oxidation enhanced the nonresonant background and altered the dielectric properties of the particles, possibly altering the local field intensities.[52] This pretreatment procedure (i.e., oxidation at 373 K for 3h) was followed with every new sample before initiating the kinetic experiments.
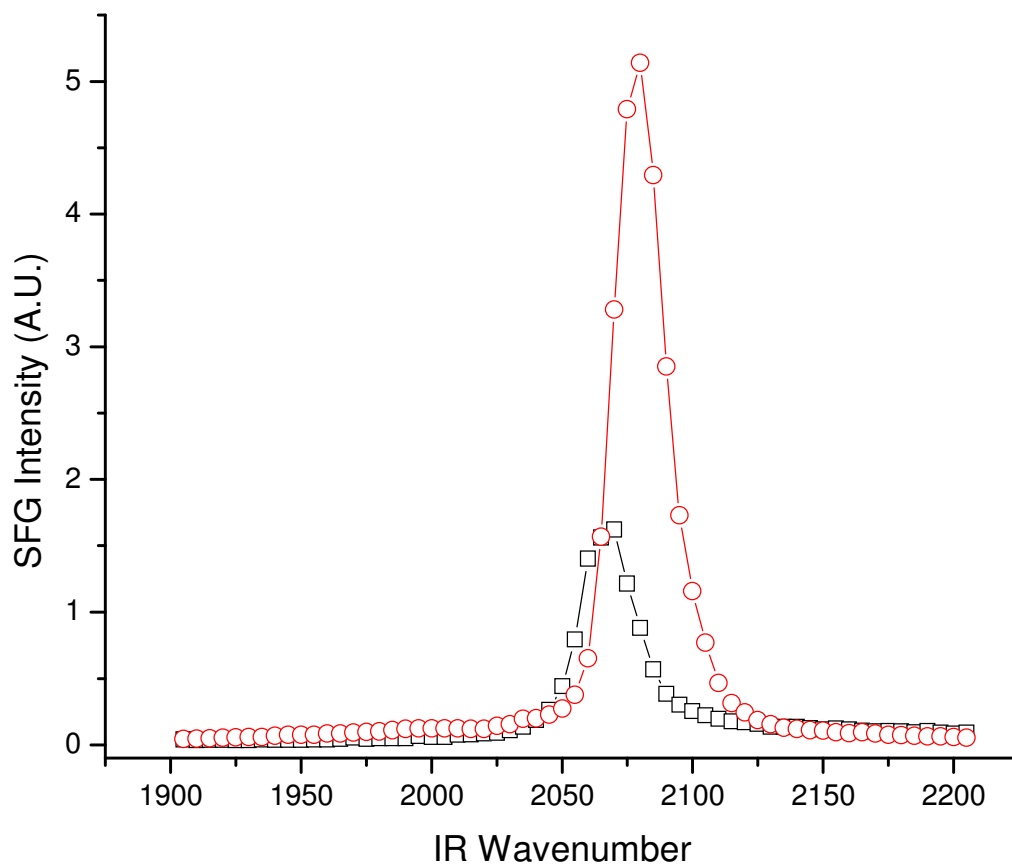
**Figure 8-7:** SFG spectra (*ssp* polarization) of an as-deposited monolayer consisting of PVP-capped Pt nanoparticles under conditions of (□) CO flow at 295 K and (○) after oxidation due to $O_2$ flow at 373 K for 3 h followed by CO flow at 295 K. The 3 h oxidation resulted in the removal of a significant fraction of the capping polymer by combustion. Both the position and the intensity of the CO peak were affected by the presence of the PVP capping agent.

In another series of oxygen pretreatments performed at room temperature, SFG spectra were collected after the successive exposure of the nanoparticle monolayer to flowing CO at 35 torr, after 5 min of purging with He, and after 3 h under a vacuum of <1 mtorr. Figure 8-8 shows typical SFG spectra from these experiments. The strong peak reveals that CO was chemisorbed onto the nanoparticle surfaces. The surfaces of fcc nanoparticles are terminated by atoms in the (100) orientation. CO binds strongly to the (100) facets, edges, and corner sites of the nanoparticle surfaces and the less coordinated step and kink sites. The peak at 2070 cm$^{-1}$ is assigned to atop bound CO, and is red-shifted significantly relative to the CO peak for single-crystal Pt(100) (~2100 cm$^{-1}$). The 30 cm$^{-1}$ shift is attributed to the co-adsorption of water and the presence of the PVP capping agent. As expected, at 35 torr there is sufficient CO to occupy all the available atop sites. The spectrum did not show any discernible changes even after one day or further exposure to CO. The fact that a change in the SFG spectrum could not be detected after the exposure to flowing He for 5 min illustrates the strength of the CO adsorption. Chemisorbed species are stable under a vacuum of <1 mtorr, yielding marginal changes in the spectrum even after 3 h. The small decrease in the intensity is likely due to a small amount of desorbed CO or oxidation resulting from the prolonged exposure to the vacuum conditions.
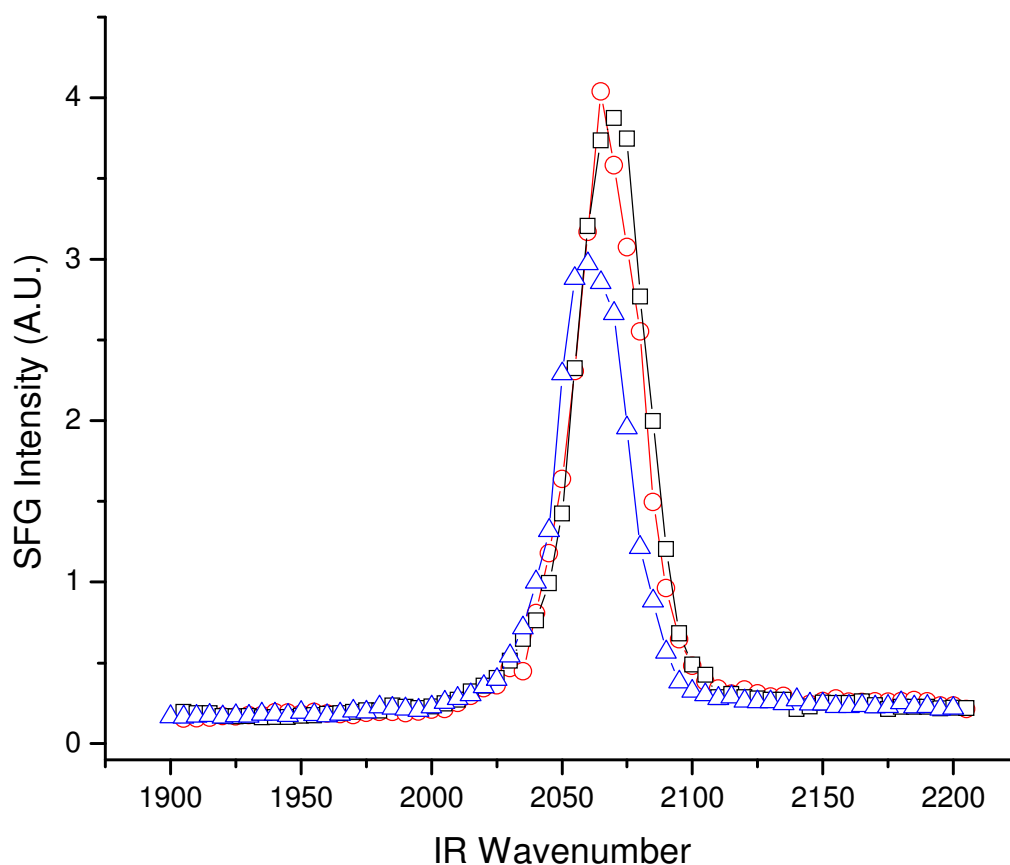
**Figure 8-8:** SFG spectra (*ssp* polarization) of an as-deposited monolayer consisting of PVP-capped Pt nanoparticles after the successive exposure to (□) CO flow at 35 torr, (○) after a 5 min purge with He, and (Δ) after 3 h in a vacuum of <1 mtorr. A very small change in the CO peak occurred after purging with He. It appears that reversibly bound CO was removed under vacuum conditions. The red-shift of the CO frequency can be related to the water desorption and the intensification of dipole-dipole coupling between neighboring CO molecules.

Since the QCM technique provides quantitative data in a nondestructive manner and is sensitive to coverage changes on small samples, it was used under identical gas flow conditions to quantify the CO adsorption and to estimate the availability of active Pt sites on the nanoparticle monolayer. First, a baseline was established by flowing He while collecting the SFG signal. Mass differences were recorded upon the introduction of CO for LB deposited nanoparticle film, 100 nm thick spin-cast PVP layer, and 10 nm thick vapor-deposited Pt film. The CO interaction was transient, and much of the loosely bound CO was removed by the subsequent He purge. Although the samples with the PVP and Pt films exhibited similar mass change, a noticeable difference was observed after flushing the cell with He. The PVP-coated sample recovered its original mass, whereas the Pt film exhibited a mass gain of approximately 20-30 ng/cm$^2$. The LB nanoparticle sample showed a different behavior. In addition to a larger amount of transiently adsorbed CO, a longer period was required for the adsorption and desorption kinetics to reach equilibrium. This might be due to a roughness difference or a tighter sieve-like conformation of the PVP capping agent around the nanoparticles. The CO that was not removed by flowing He was permanently adsorbed onto the nanoparticle and vapor-deposited Pt films. A comparison of the residual CO content with the intensity of the SFG signal demonstrated the sensitivity of SFG spectroscopy to a very small surface coverage. The insensitivity of the SFG signal to CO interacting with the PVD capping agent or transiently bound CO was shown by the negligible changes in the SFG spectrum during He flow. QCM measurements of the nanoparticle monolayer showed a mass gain of ~30 ng/cm$^2$ (normalized by the total area of the QCM disc) upon CO adsorption and subsequent flushing with He gas. For a Pt:CO ratio equal to 1:1, this mass gain represents

160

a number density of active Pt sites of $7 \times 10^{14}$ cm$^{-2}$. For densely-packed cubic nanoparticles with only one face exposed, the previous estimate implies that ~70% of the potential sites were free of water and/or organic adsorbates.

**In-situ oxidation of CO on clean surfaces of platinum nanoparticles.** After heating the samples at 373 K in oxygen to remove the water, they were exposed to flowing CO for 5 min. Adsorption was immediate and was subsequently followed by a 10 min treatment with flowing He gas to remove any residual CO from the reaction cell. SFG spectra were obtained during the flow of $O_2$ ($O_2$/He:10/90 by volume) at 338 K at 1 min intervals, acquiring 50 shots for each data point at increments of 5 cm$^{-1}$ in the range of 2060-2110 cm$^{-1}$. Fig. 8-9 shows Lorentzian curves that were fitted to SFG spectra collected every 20 s in *ssp* polarization during oxidation by flowing $O_2$. Similar to previous SFG results, the CO peak exhibited a red-shift during oxidation.[53] The intensity of the CO peak decayed with the increase of time and could not be detected after 40 min. Since the He flow did not affect the CO peak intensity over the same time period, it may be concluded that the primary reaction was oxidation, while desorption was secondary.
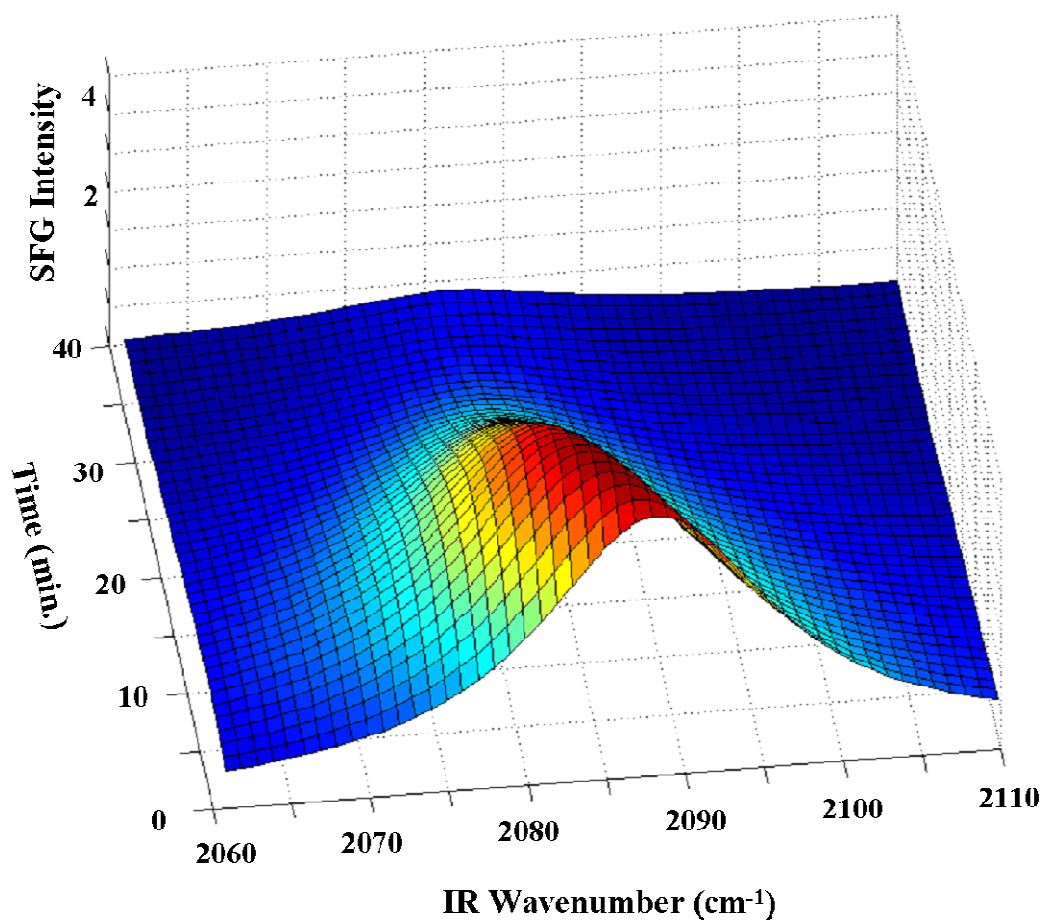
**Figure 8-9:** Lorentzian curve fits to SFG spectra (*ssp* polarization) for a He-purged and CO-saturated monolayer consisting of PVP-capped Pt nanoparticles obtained every 20 s under conditions of $O_2$ flow at 295 K. A red-shift of the CO atop peak emerges as the reaction proceeds and CO is removed from the surface by oxidation to $CO_2$.

After an identical preparation procedure, CO was introduced at 373 K for 5 min and the system was flushed with He for more than 10 min prior to initiating oxidation by flowing $O_2$/He (10/90 by volume). Each data set was repeated three times. The signal-to-noise ratio was sufficiently high to obtain kinetic measurements within a narrow frequency range including the maximum of the atop CO peak. The intensity was

162

monitored in the 2080-2085 $cm^{-1}$ range at ~8 s intervals, collecting 50 shots for each data point at temperatures above 338 K. Fig. 8-10 shows representative exponential decay curves of the atop CO peak intensity for different temperatures. The calculated activation energy of ~19.8 kcal/mol is close to the expected value of 13 kcal/mol for Pt(100) below the ignition temperature.[54] It was also reported that the reaction order of CO with the Pt(100) surface vanished below ignition. The uniform change in slope of the decay curves indicates that the surface coverage effect on the reaction rate was insignificant. The activation energy for desorption on the Pt(100) surface is ~30 kcal/mol.[55] This provides further confirmation that oxidation was the dominant mechanism.

Fig. 8-11 shows a comparison between the reaction kinetics determined from SFG and GC data in excess oxygen (i.e., 100 torr of $O_2$ and 10 torr of CO). By applying a line fit to the integrated thermal conductivity detector signal of $CO_2$ versus time, reaction rates were measured as functions of temperature and were then used to obtain Arrhenius plots. The similar activation energies determined by the two methods provide support to the prior assertion that oxidation was the primary reaction pathway, as determined by the atop CO peak in the SFG spectra.
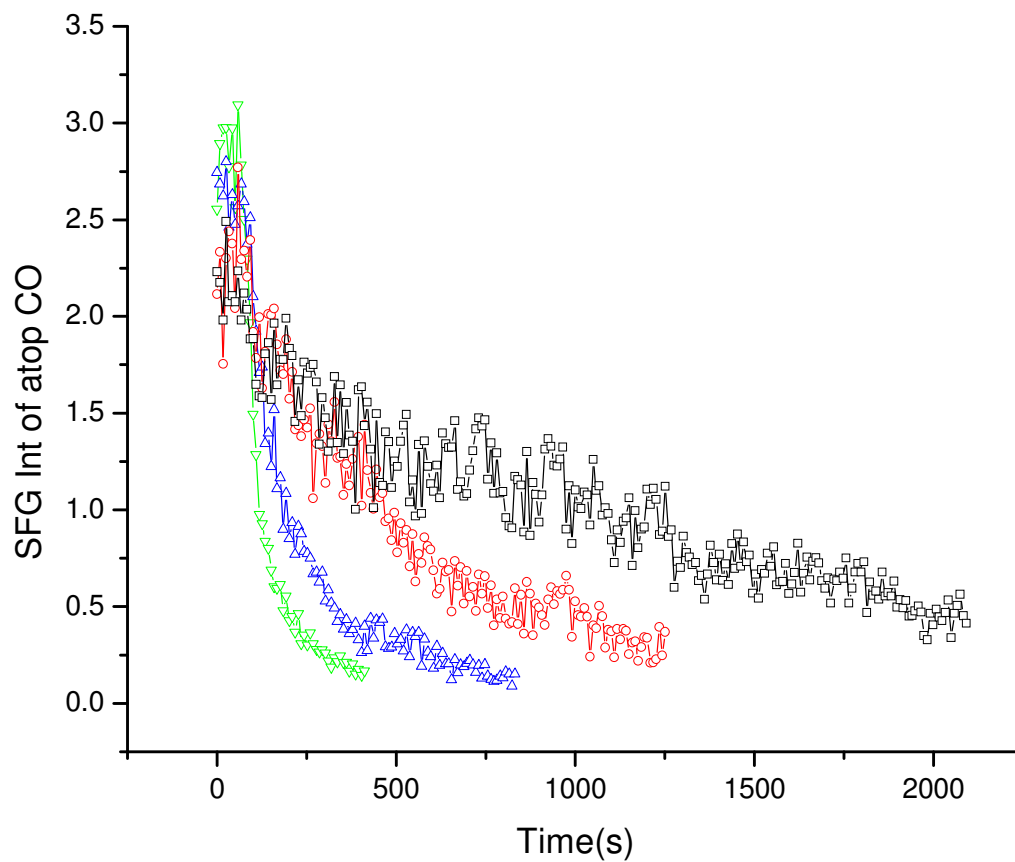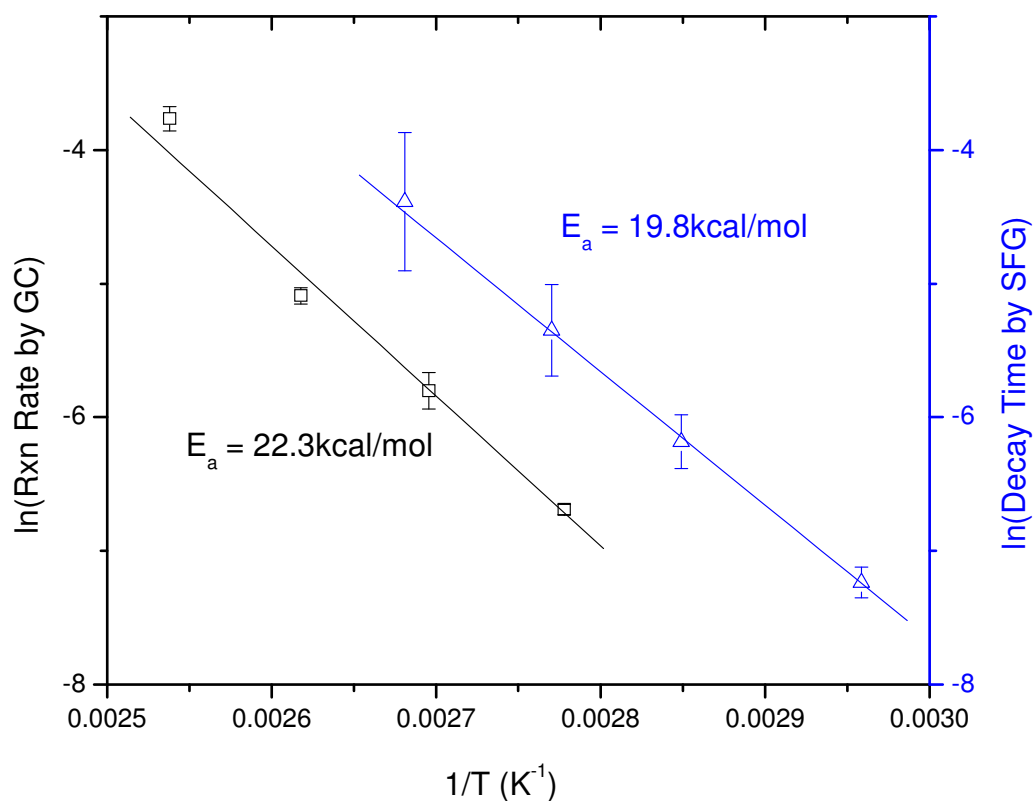
**Figure 8-10:** Square root of the atop CO peak intensity in the SFG spectrum (*ssp* polarization) of a monolayer consisting of PVP-capped Pt nanoparticles versus time for O$_2$ flow at (□) 338 K, (○) 351 K, (△) 361 K, and (▽) 373 K..

**Figure 8-11:** Arrhenius plots of CO oxidation measured by the first-order exponential decay of the SFG intensity of the atop CO peak ($\Delta$) and the accumulation of $CO_2$ in the gas phase determined by gas chromatography ($\square$). The apparent activation energies calculated by the two independent methods are in good agreement with each other and reported values for single-crystal Pt and oxide-supported Pt nanoparticle catalysts.

Even though the origins of the nonlinear susceptibility and the enhancement resulting from local field interactions are complex, monitoring the decay provided quantitative results reflecting the nature of the surface species. Recent SFG studies indicate that nanoparticle sizes important to catalytic reactions do not produce SFG in external reflection when molecules adsorb on both the top and the bottom sides of the

particles.[56] Despite the intricate centrosymmetric system and unclear origin of SFG in TIR, the results illustrate the potential of this technique. Additionally, traditional methods for monitoring the evolution of reactions (including GC) are not practical for two-dimensional nanoparticle arrays due to the very small amount of the reaction products. Although the disappearance of a surface bound species is an indirect measure of a single reaction pathway, the present technique provides new insight into complex reaction phenomena with the added benefits of in-situ monitoring and ease of data collection. For example, a kinetic curve for CO oxidation on such a small active Pt area can be obtained with the present technique in less than 20 min. This is profoundly faster than the several hours or even days needed to monitor initial reaction rates with the GC method at similar temperatures. Additionally, surface interactions between the bound species and the metal surface can be observed in situ.

## 8.5 Conclusion

Sum frequency generation vibrational spectroscopy was successfully applied to a model nanoparticle system. Total internal reflection geometry was used to enhance the signal intensity. A high-pressure reactor system that enables in-situ SFG characterization and reaction studies of nanoparticle monolayers was used in this study. With this system, in-situ coherent SFG measurements are possible without the need for bulk correction or complex dielectric considerations for optically complex systems. CO is a model adsorbate to study because of its inherently large cross section and polarizability that makes it amenable to detection by SFG. A monolayer consisting of cubic Pt nanoparticles of 7.1 nm average size was synthesized by a modified polyol process in the presence of

166

PVP and Ag ions. CO adsorption was studied on as-synthesized Langmuir-Blodgett films and films calcinated in oxygen to remove the residual PVP. The removal of PVP enhanced the CO adsorption significantly because of the increased availability of active sites, resulting in a red-shift of the atop CO peak due to the intensification of dipole-dipole coupling. The CO coverage of the pretreated nanoparticle monolayer was also evaluated by quartz crystal microbalance measurements. The oxidation of a CO monolayer in the presence of flowing oxygen studied by in-situ SFG revealed an additional red-shift of the CO peak with time and the simultaneous decrease in the SFG intensity. Reaction rates and apparent activation energy for CO oxidation were found to be in good agreement with previous similar results for single-crystal Pt films. Results from gas chromatography measurements authenticated the activation energy derived from the SFG measurements.

## References

1 Hagen, D. I., Niewenhuys, B. E., Rovida, G., and G. A. Somorjai, *Surf. Sci.* **1976**, 57, 632.

2 Doyen, G., and G. Ertl, *Surf. Sci.* **1974**, 43, 197.

3 Morgan, A. E., and G. A. Somorjai, *J. Chem. Phys.* **1969**, 51(8), 3309.

4 Akimoto, K., Sakisaka, Y., Nishijima, M., and M. Onchi, *Surf. Sci.* **1979**, 88, 109.

5 Baro, A. M., and H. Ibach*, J. Chem. Phys.* **1979**, 71, 4812.

6 Sheppard, N., and T. T. Nguyen, Adv. *Infrared Raman Spectrosc.* **1978**, 5, 66.

7 Iwasawa, Y., Mason, R., Textor, M., and G. A. Somorjai, *Chem. Phys. Lett*. **1976**, 44, 468.

8 Heilmann, P., Heinz, K., and K. Muller, *Surf. Sci.* **1979**, 83, 487.

9 Morgan, A. E., and G. A. Somorjai, *Surf. Sci.* **1968**, 12, 405.

10 Broden, G., Pirug, G., and H. P. Bonzel, *Surf. Sci.* **1978**, 72, 45.

11 Behm, R. J., Thiel, P. A., Norton, P. R., and G. Ertl, *J. Chem. Phys*. **1983**, 78, 7437.

12 Gardner, P., Martin, R., Tushaus, M., and A. M. Bradshaw, *J. Electron Spec. Relat. Phenom.* **1990**, 54/55, 619.

13 McCrea, K. R.; Parker, J. S.; Chen, P.L., Somorjai, G. A. *Surf. Sci.* **2001**, 494, 238.

14 Hong, S., and H. H. Richardson, *J. Chem. Phys*. **1993**, 97, 1258.

15 Ohno, Y., Sanchez, J. R., Lesar, A., Yamanaka, T., and T. Matsushima, *Surf. Sci.* **1997**, 382, 221.

16 Su, X., Cremer, P. S., Shen, Y. R., and G. A. Somorjai, *J. Am. Chem. Soc.* **1997**, 119, 3994.

17 Imbihl, R., Cox, M. P., and G. Ertl, *J. Chem. Phys*. **1986**, 84, 3519.

18 Hafner, J., and A. Eichler, *Surf. Sci.* **1999**, 433, 58.

19 Imbihl, R., Cox, M. P., and G. Ertl, *J. Chem. Phys*. **1985**, 83, 1578.

20 Rinnemo, M., Kulginov, D., Johansson, S., Wong, K. L., Zhdanov, V. P., and B. Kasemo, *Surf. Sci.* **1997**, 376, 297.

21 Berlowitz, P. J., Peden, H. F., and D. W. Goodman, *J. Chem. Phys*. **1988**, 92, 5213.

22 Szabo, A., Henderson, M. A., and J. T. Yates, Jr., *J. Chem. Phys*. **1992**, 96, 6191.

23 Akiyama, H., Moise, C., Yamanaka, T., Jacobi, K., and T. Matsushima, *Chem. Phys. Lett.* **1997**, 272, 219.

24 Boudart, M. *Adv. Catal.* **1969**, 20, 153.

25 Mavrikakis, M.; Bäumer, M.; Freund, H. J.; Nørskov, J. K. *Catal. Lett.* **2002**, 81, 153.

26 La Mer, V. K.; Dinegar, R. H. *J. Am. Chem. Soc.*. **1950**, 72, 4847.

27 Baldelli, S.; Eppler, A. S.; Anderson, E.; Shen, Y. R.; Somorjai, G. A. *J. Chem. Phys*. **2000**, 113, 5432.

28 Contreras, A. M.; Grunes, J.; Yan, X. M.; Liddle, A.; Somorjai, G. A. *Catal. Lett.* **2005**, 100, 115.

29 Somorjai, G. A.; Rioux, R. M. *Catal. Today* **2005**, 100, 201.

30 Grunes, J., Zhu, J., Yang, M., Somorjai, G. A., *Catal. Lett.* **2003**, 86, 157.

31 Lai, X.; St. Clair, T. P.; Valden, M.; Goodman, D. W. *Prog Surf. Sci.* **1998**, 59, 25.

32 Song, H.; Kim, F.; Connor, S.; Somorjai, G. A.; Yang, P. *J. Phys. Chem. B* **2005**, 109, 188.

33 Su, X., Cremer, P. S., Shen, Y. R., Somorjai, G. A. *J. Am. Chem. Soc.* **1997**, 119, 3994.

34 Dellwig, T.; Rupprechter, G.; Unterhalt, H.; Freund, H.-J. *Phys. Rev. Lett.* **2000**, 85, 776.

35 Roke, S.; Roeterdink, W. G.; Wijnhoven, J. E. G. J.; Petukhov, A. V.; Kleyn, A. W.; Bonn, M. *Phys. Rev. Lett.* **2003**, 91, 258302.

36 Rioux, R. M. ; Toops, T. J. ; Grass, M. ; Niesz, K. ; Kuperman, A. ; Yang, P. ; Somorjai, G. A., to be submitted.

37 Rioux, R. M.; Song, H.; Grass, M.; Habas, S.; Niesz, K.; Hoefelmeyer, J. D.; Yang, P.; Somorjai, G. A. *Top. Catal*. **2006**, in press.

38 Campostrini, R.; Caruran, G.; Baraka, R. M. *J. Mol. Catal*. **1993**, 78, 169.

39 Shen, Y. R. The Principles of Nonlinear Optics; Wiley; New York; **1984**.

40 Kweskin, S. J.; Komvopoulos, K.; G. A. Somorjai, *Langmuir* **2005**, 21, 3647.

41 Yeganeh, M. S.; Dougal, S. M.; Silbernagel, B. G. *Langmuir* **2006**, 22, 637.

42 Yu, R.; Song, H.; Zhang, X.; Yang, P. *J. Phys. Chem. B* **2005**, 109, 6940.

43 Ferri, D.; Bürgi, T.; Baiker, A. *J. Phys. Chem. B* **2001**, 105, 3187.

44 Persson, B. N. J.; Ryberg, R. *Phys. Rev. B* **1981**, 24, 6954.

45 Brandt, R. K.; Sorbello, R. S.; Greenler, R. G. *Surf. Sci.* **1992**, 271, 605.

46 Mukerji, R. J.; Bolina, A. S.; Brown, W. A. *Surf. Sci.* **2003**, 527, 198.

47 Borodko, Y.; Habas, S. E.; Koebel, M.; Yang, P.; Frei, H.; Somorjai, G. A., to be

submitted.

48 Yoshida, M.; Prasad, P. N. *Appl. Optics* **1996**, 35, 1500.

49 de Caro, D.; Köhler, J.; Busser, W.; Bradley, *J. Macromol. Symp*. **2000**,156, 53.

50 Campbell, C. T.; Ertl, G.; Kuipers, H.; Segner, J. *J. Chem. Phys*. **1980**, 73, 5862.

51 Blyholder, G. *J. Phys. Chem.* **1964**, 68, 2772.

52 Eischens, R. P.; Francis, S. A.; Pliskin, W. A. *J. Phys. Chem.* **1956**, 60, 194.

53 McCrea, K. R.; Parker, J. S.; Somorjai, G. A. *J. Phys. Chem. B* **2002**, 106, 10854.

54 Berlowitz, P. J.; Peden, C. H. F.; Goodman, D. W. *J. Phys. Chem.* **1988**, 92, 5213.

55 McCabe, R. W.; Schmidt, L. D., *Surf. Sci*. **1977**, 66, 101.

56 Pang, S. F.; Kurosawa, Y.; Kondo, T.; Kawai, T. *Chem. Lett.* **2005**, 34, 544.

# Chapter 9

# Ethylene decomposition on platinum nanoparticle cubes

## 9.1 Introduction

In order to gain an understanding of the catalysts structure contribution to reaction selectivity, a molecular level investigation of catalytic processes must probe real industrial conditions (high temperature and pressure supported nanoparticles). In the 1960's, Boudart[1] classified structure sensitive reactions as those that showed a change in turnover frequency with the change in the catalyst particle size. Ammonia synthesis studies on single-crystal iron surfaces showed that the (111) and (210) faces were orders of magnitude more reactive than the (110) close-packed structure.

Several reactions have been carried out on single-crystal surfaces to determine the effect of structure on reactivity and selectivity. Application to nanoparticles impeded by difficulty in preparation and characterization of catalysts. Though structure insensitive,

ethylene hydrogenation was chosen as a probe reaction to assess the extent of reactivity and compare reaction parameters to classically prepared supported catalysts and single crystals. At standard conditions of 10 Torr $C_2H_4$, 100 Torr $H_2$, a room temperature turnover frequency of 10 $s^{-1}$ was measured for a Pt(111) single crystal.[2] In similar conditions, turnover frequencies as high as 20 $s^{-1}$ and as low as $10^{-3}$ $s^{-1}$ have been measured on supported Pt catalysts, depending on the catalyst type, preparation and measurement techniques.[3,4] Catalytic activity deactivation has been shown to decrease with smaller particles. The reason for this behavior is unknown at the time but may be related to stronger adsorption of ethylidyne and its subsequent decomposition on the surface of larger particles. Comparison of the initial heats of adsorption of ethylene and identification of adsorbed species by various surface spectroscopies suggests that the dehydrogenation of adsorbed ethylene is suppressed on small crystallites. Passos and Vannice[5] found that the initial heat of adsorption at 300 K was 10 kcal $mol^{-1}$ higher on large (~20 nm) Pt particles as compared with small Pt particles (~1 nm); the higher heat of adsorption on large crystals is attributed to the exothermic dehydrogenation of ethylene to ethylidyne or ethylidene.[6]

We have designed and constructed a reactor system for the in-situ high pressure SFG characterization of nanoparticles in total internal reflection (TIR) geometry. This technique is nondestructive and provides sensitivity and specificity to interface reaction intermediates and insight into conformational changes on the nanoparticle surface. A monolayer of {100} platinum cubes (7.1 nm) on (0001) aluminum oxide was investigated under catalytic flow conditions. SFG confirmed that the heterogeneous metal surface intermediates were identical to those observed previously on {100} platinum single

crystals. In this chapter, spectra obtained during the oxidation/reduction cycles at 373 K and in the presence of carbon monoxide (CO) will be examined.
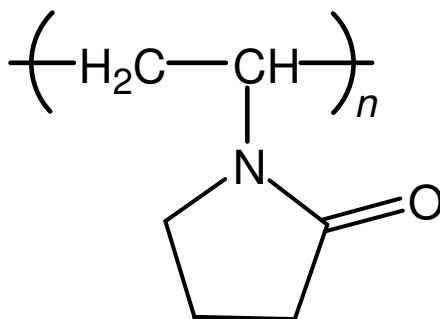
Platinum nanoparticles dispersed on high surface area inorganic oxides are a mainstay of modern industrial heterogeneous catalysis. Oxide supports stabilize the particles and promote reaction intermediates.[7] Studies on single crystals have demonstrated the importance of steps, kinks, and facets for metal catalyst surface reactivity and resistance to deactivation.[8,9] It was also shown that by specific engineering of the shape and size of the nanoparticles (crystal face), control can be gained over selectivity in many common reactions. Since most commercial catalytic processes do not occur on flat single-crystal metal substrates, it is important to link this model approach to practical material systems. Recent advances in colloidal chemistry reveal the ability to control the particle size and face of noble metals with tremendous accuracy. Presently, the traditional surface science techniques must expand to incorporate these experimentally difficult systems.

Although sum frequency generation (SFG) spectroscopy is a surface sensitive technique that has been applied successfully to various catalytic high pressure systems, it has primarily been utilized on flat substrates due to ease of collection and analysis. [10] Therefore, the application of this technique to irregular geometries such as nanoparticle catalysis was the objective of this study. The potential to control the particle shape to enhance activity and selectivity has motivated the present investigation on platinum nanoparticles with preferentially exposed {100} facets. Recent experimental evidence suggests that the unique ability of the {100} face to restructure imparts catalytic properties that may be tuned for a desired effect, such as dehydrogenation.[11]

The detection of a second-order nonlinear process photons from submicrometer sized materials is complicated by Rayleigh scattering and centrosymmetry inherent to particles of less than the wavelength of light. In TIR geometry, these effects are minimized. Due to the high index internal reflection element and the exponential decay of the incident electric field, coherent SFG is collected from particles during high pressure reaction conditions. By measuring the SFG signal produced from the ordered surface species on the platinum cubes, we can investigate the surface intermediates during reactant adsorption, active sites during CO chemisorption, and determine the effect of oxidation/reduction flowing conditions.

## 9.2 Experimental Procedures

**Synthesis and assembly of platinum nanoparticles.** The synthesis and assembly of Pt nanoparticles with predominant cubic shape has been published previously.[12] A brief summary is given below. Cubic platinum nanoparticles (7.1 nm) are produced by a modified polyol process in the presence of poly(vinylpyrrolidone) (PVP) (Fig. 9-1). Briefly, 2.5 mL of ethylene glycol (EG) is heated at reflux for for 5 min. A total of 0.5 mL of $AgNO_3$ solution ($2 \times 10^{-3}$ M, Ag/Pt = 1.1 mol %) was added to the boiling EG. Immediately, EG solutions of PVP (93.8 μL, 0.375 M) and $H_2PtCl_6 \cdot 6H_2O$ (46.9 μL, 0.0625 M) are added to the mixture every 30 s over a 16 min period. The resulting solution is heated for an additional 5 min. The products consisting of ~80% cubes are purified by repetitive precipitation and centrifugation and finally dispersed in chloroform.

**Figure 9-1:** Molecular structure of poly(vinylpyrrolidone) (PVP).

Platinum nanoparticles were assembled and deposited onto an equilateral sapphire prism by the Langmuir-Blodgett (LB) technique. A colloidal platinum solution was dispersed onto deionized water (resistivity = 18 MΩ cm) subphase on a LB trough (NIMA Technology, Type 611) at room temperature. The surface pressure was monitored with a Wilhelmy plate and adjusted to zero before spreading the particles. The resulting surface layer was compressed by moving a mobile barrier at a rate of 0.3 cm$^2$ min$^{-1}$. At a surface pressure of 6 mN m$^{-1}$, the Pt monolayer at the water-air interface was carefully transferred onto the sapphire using the Langmuir-Schäffer horizontal liftoff method.

**Flow Reactor.** Fig. 8-4 illustrates the experimental setup that enables in-situ SFG characterization of adsorbate adsorption on a well ordered monolayer of nanoparticles. An equilateral sapphire prism (Red Optronics, Mountain View, CA) was held in compression against a rubber O-ring (size?) by a teflon block fitted onto the apex of the prism secured by two set screws. A vacuum manifold connecting the cell and a mechanical pump enabled a vacuum of ~1 mTorr, while a gas manifold equipped with a series of mass flow controllers (Porter Instruments, Hatfield, PA) enabled operation of

the spectroscopy-reactor cell at atmospheric pressure. $H_2$ (Praxair, UHP, 99.999%), He (Praxair, UHP, 99.999%), 20% $O_2$/He mixture (Praxair, UHP, 99.999%), CO (AirGas, CP grade) and ethylene (Praxair, CP grade) were used as received. Flow rates of reactant gases were typically maintained at 95 $cm^3$ (STP) $min^{-1}$ when operating under continuous flow conditions. The temperature of the sapphire was measured by a thermocouple placed in direct contact with the underside of the sapphire prism while heating was conducted with two Kapton resistive elements (Omega Engineering Inc., Stamford, CT) on the sides of the prism. Temperature varations across the $20 \times 20$ mm area (area of the prism base) were very small, as seen by locating the thermocouple at different points across the surface.

**Sum frequency generation vibrational spectroscopy**. SFG vibrational spectroscopy is ideal for studying the composition and conformational behavior at interfaces. SFG spectra were obtained with Nd:YAG laser (Leopard, Continuum, Santa Clara, CA). In the present system, a tunable infrared (IR) beam was combined with 532 nm radiation at the sample interface at corresponding incident angles of 60° and 65° with respect to the surface normal. Due to the complicated nature of this system and complex dielectric dispersion, the critical angle and large Fresnel enhancement were avoided. Since the size of the particles is well below the necessary dimensions for 532 nm surface plasmon resonance, this enhancement was considered minor.[13] In this chapter, all the data are presented in ssp polarization combination, and incidence angle greater than 15° above the critical angle. Other polarization (ppp and sps) experiments were conducted, but mainly reflect the dielectric properties of the monolayer. The ssp polarization is more

sensitive to symmetric vibrational modes, and the signal produced is larger for this procedure.

## 9.3 Results and Discussion

**Synthesis and characterization of Pt monolayers.** During the synthesis, cubes were produced with ~80 % selectivity, with tetrahedra comprising 10% of the final composition. Fig. 8-6 is a representative TEM image of 7 nm nanoparticles deposited on a TEM grid. At the intermediate coverages (~ 40 %) used in this work, the spacing between particles ranged from a few nanometers (defined by the expected 1-2 nm PVP coating on each particle) to more than 20 nm. After evaporation of the chloroform, no significant migration of the particles was observed. Previous in-situ electron microscopy studies of these same nanoparticles have shown that the edges of the cubic nanoparticles become rounded upon heating at 623 K in vacuum,[14] which is in good agreement with the observed truncation of sodium polyacrylate capped tetrahedral and cubic Pt nanoparticles at temperatures between 623–723 K.[15] Based on these observations, PVP was removed from the catalyst surface by low temperature (373 K) cyclic oxidation reduction cycles or clean and oxidized surfaces were produced by heating in $O_2$ for 3 h at 373 K. The data presented for "clean" nanoparticles is based upon five oxidation-reduction cycles at 373 K, which was determined as an optimal pretreatment considering both polymer removal and maintenance of particle shape.[16]

**Characterization of polymer capping agent on Pt nanoparticle surface.** Molecular, polymeric or macromolecular (dendrimers) surfactants are used in solution phase nanoparticle synthesis to prevent particle aggregation, and they may also contribute

179

to size and shape control observed in a number of these syntheses.[17]  The mechanism by which these organic phases interact with metal ions and nanoparticles in solution has been investigated; it is primarily believed that PVP coordinates to metal ions or nanoparticles through its carbonyl group.  The interaction between PVP and metal ions is proposed to occur through the carbonyl group of the pyrrolidone side group and the ability of the polymer chain to interact with other sections (i.e. intramolecular) of the polymer chain containing Pt ions enable the encounter of zero valent metal ions and the formation of Pt nanoparticles.  The adsorption of PVP to 7 nm cubic Pt nanoparticles was studied by SFG vibrational spectroscopy for a PVP monolayer spin cast from a 5% wt. solution in chloroform onto a clean (0001) sapphire prism as a control.   The SFG vibrational spectrum of the sapphire/nanoparticle and sapphire/PVP monolayer for *ssp* polarization is shown in Fig. 9-2.  The spectrum of the sapphire/PVP interface in the C-H stretching region is composed two very broad peaks at 2890 and 2980 cm$^{-1}$, which are assigned to symmetric $CH_2(s)$ and asymmetric $CH_2(as)$ stretches of both the pyrrolidone ring and the backbone.  These values compare well with reported literature values for liquid phase 2-pyrrolidone.[18]  The intensity of the $CH_2(s)$ pyrrolidone ring peak indicates that the polymer is well ordered with the ring and main-chain backbone lying flat against the sapphire.  The spectrum of PVP capped Pt nanoparticles is comprised of two peaks at 2860 and 2940 cm$^{-1}$, which are attributed to symmetric and asymmetric methylene vibrations, respectively.  They are redshifted by 30-40 cm$^{-1}$ when compared to a spin cast PVP film, suggesting an electron density donation from PVP to platinum.  This suggests that the pyrrolidone ring is parallel to the surface and the vinyl backbone is also in close proximity to the surface.   It is proposed that PVP adsorbs to metal surfaces via the

carbonyl bond. The SFG set up used in this work suffers from low power at carbonyl stretching energies (1670 cm$^{-1}$) preventing its detection. The carbonyl stretch for PVP coordinated to 2.9 nm Pt nanoparticles has been observed at ~1625 cm$^{-1}$,[19] a 45 cm$^{-1}$ redshift relative to the liquid phase frequency. The complexity of the system prohibits further interpretation of the PVP spectra. Since there are multiple interfaces which can produce SFG signal (e.g. sapphire/polymer, top, side and bottom of the nanoparticles, and polymer/air), further investigations in this region are not pursued.
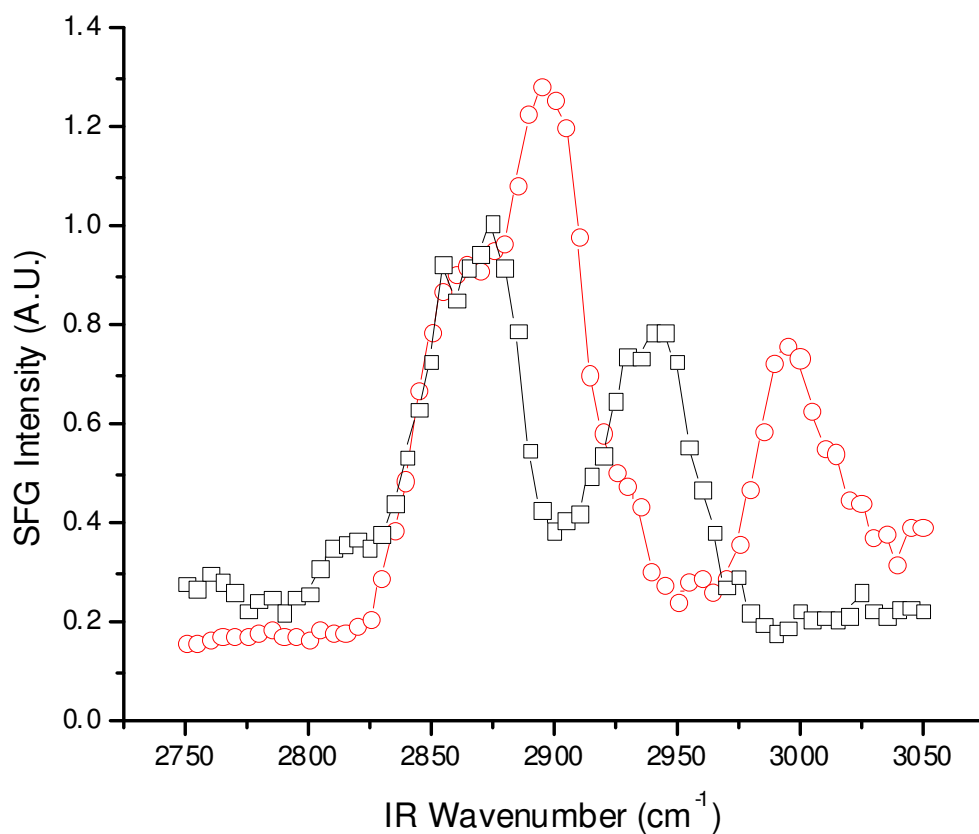
**Figure 9-2:** SFG spectra collected in *ssp* polarization of sapphire/nanoparticle (□) and sapphire/polymer (○) interfaces.

Dendrimer stabilized Pt nanoparticles are capable of adsorbing carbon monoxide in solution but not in the dried state, presumably due to the collapse of the dendrimer around the nanoparticle. [20] The removal of surface protecting agents from nanoparticle surfaces is an important step for maximizing the activity of these nanoparticles during gas-phase heterogeneous catalysts. The adsorption of carbon monoxide on PVP-capped Pt nanoparticles suggests that the polymer capping agent is extremely flexible, enabling CO to adsorb and causing a restructuring of PVP from an ordered to a disordered state

(Fig. 9-3). Both the symmetric and asymmetric $CH_2$ peaks of PVP decrease in intensity upon CO adsorption. Exposure of the Pt monolayer to oxygen leads to the CO removal by oxidation and the restructuring of the PVP adlayer. For the most part, the conformational change of PVP upon CO adsorption appears to be reversible although the asymmetric stretches fail to fully recover. The ability of carbon monoxide to adsorb is most likely due to a porous PVP layer, which suggests that the particles may be catalytically active even before removing the polymer. In fact, catalytic reactivity results have shown that PVP-coated Pt nanoparticles supported on silica is active for ethylene hydrogenation,[21] although they are significantly more active after calcination and reduction pretreatments. The CO stretching frequency was redshifted by 20 $cm^{-1}$ relative to CO adsorbed on a Pt nanoparticle monolayer, which had been calcined in $O_2$ at 373 K for 3 h (2090 $cm^{-1}$).
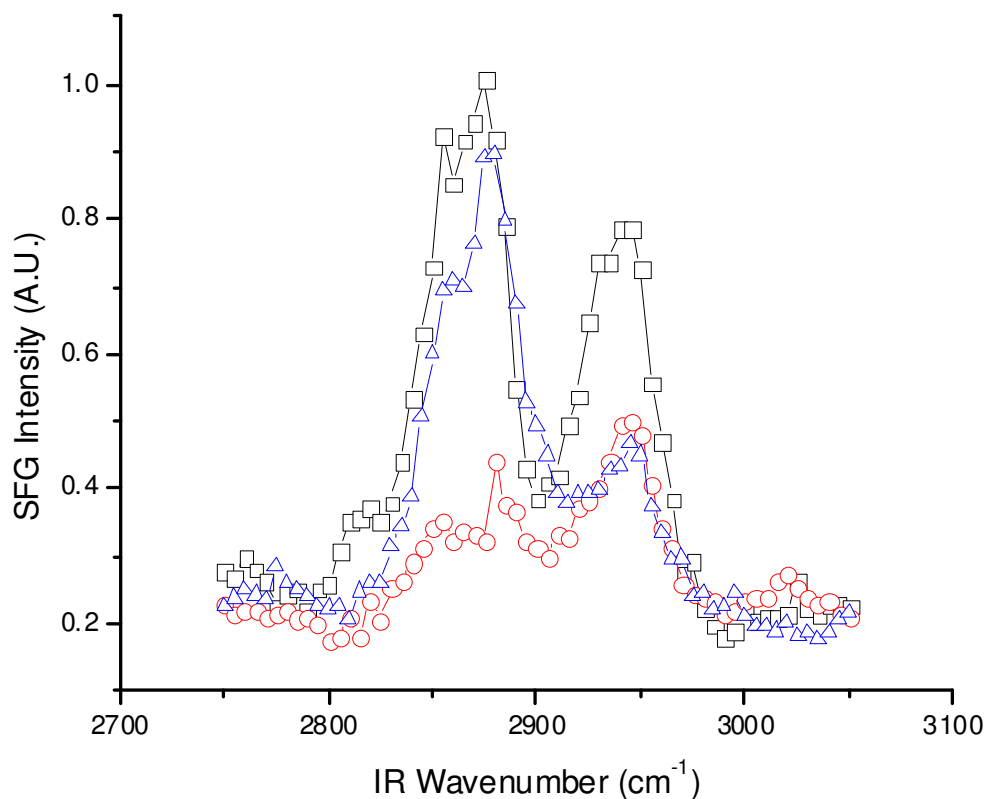
**Figure 9-3:** SFG spectra collected in *ssp* polarization of sapphire/nanoparticle interface for (□) as-deposited nanoparticle monolayer with PVP capping agent, (○) in flowing CO, and (Δ) in air again.

**Extent of PVP removal by oxidation-reduction determined by SFG investigation of CO adsorption.** The removal of PVP from the dried nanoparticle surface has proven challenging due to the strong coordination to the Pt nanoparticle surface, collapse and densification of PVP monolayer, and the inability to completely remove residual carbonaceous fragments from the Pt surface.[22] Recently, a cyclic oxidation-reduction cycle at low temperatures (373-673 K) has been developed for the removal of PVP from the surface of Pt nanoparticles supported on mesoporous silica.[23]

This method has been extended and utilized with the Pt nanoparticle arrays fabricated in this study. Fig. 9-2 demonstrates that peaks assigned to PVP are clearly identified on the nanoparticle surface after synthesis. The intense bands in the C-H stretching region suggest that PVP is well ordered on the surface and suggests that PVP is strongly coordinated to the surface. After five oxidation/reduction cycles at 373 K, the SFG spectrum (Fig. 9-5) of the sapphire/nanoparticle interface (intensity is scaled by 1/8 for PtO spectra) is essentially featureless with a large nonresonant background,[24] suggesting that PVP has been completely removed or the fraction of PVP which remains on the surface after the oxidation-reduction treatments is disordered. Adsorbate ordering at the interface is necessary for the generation of SFG from the adsorbate at an interface. In separate study, rates of olefin hydrogenation on supported Pt catalysts increased after each oxidation-reduction cycle, up to five, after which hydrogenation rates did not change with cycle number. These results suggest that lack of SFG signal in Figure 4 is due to PVP removal rather than it present as a disordered adlayer. Introduction of $H_2$ to surface after cyclic oxidation-reduction leads to the formation of a broad peak from 2750 to 2900 $cm^{-1}$. This feature most likely corresponds to C-H stretches from the remaining polymer.

Changes in the SFG spectra following the oxidation/reduction cycles become evident when comparing the adsorption of carbon monoxide before and after cyclic oxidation-reduction pretreatment. Accompanying changes in CO adsorption may provide insight into the effects of oxidation/reduction cycles on available adsorption sites on the platinum surfaces. Prior to oxidation-reduction treatment the spectrum shows a single peak at 2060 $cm^{-1}$, red-shifted approximately 30-40 $cm^{-1}$ compared with CO adsorption on a Pt(100) single crystal. [25,26] Following the first oxidation cycle at 373 K, the intensity

of the atop CO peak increased by a factor of two as a result of an increase in the exposed active surface area. Additionally, Fig. 9-4 illustrates the reduction of the platinum nanoparticle as a helium/hydrogen mixture flows through the reaction cell and shifts the atop CO peak due to the formation of surface water or co-adsorbed hydrogen.
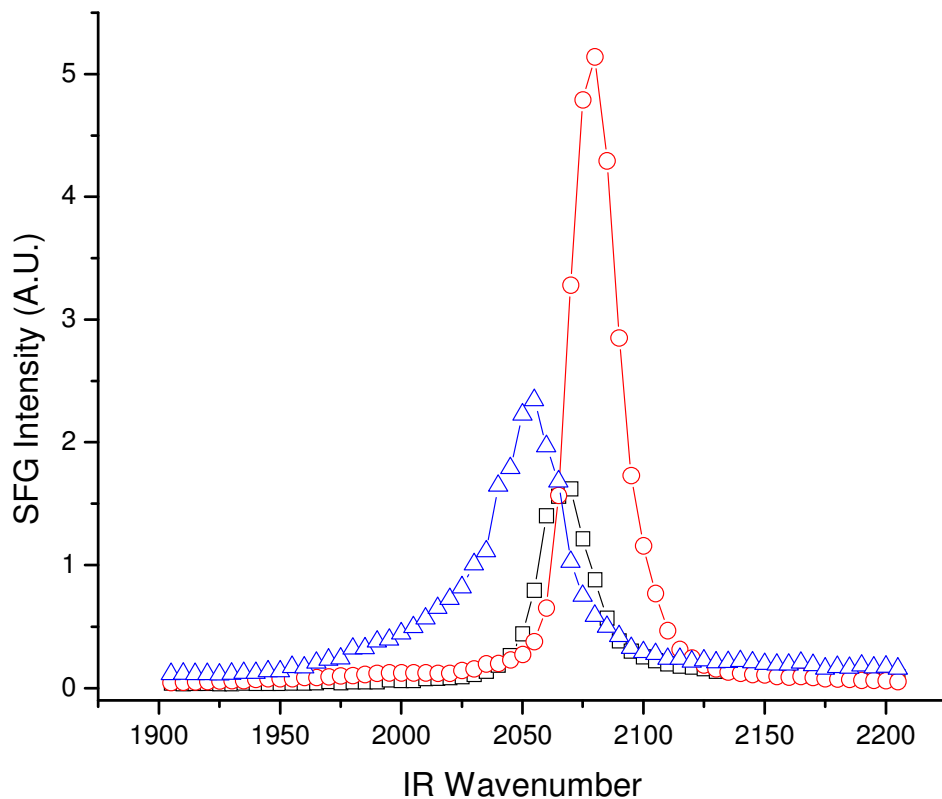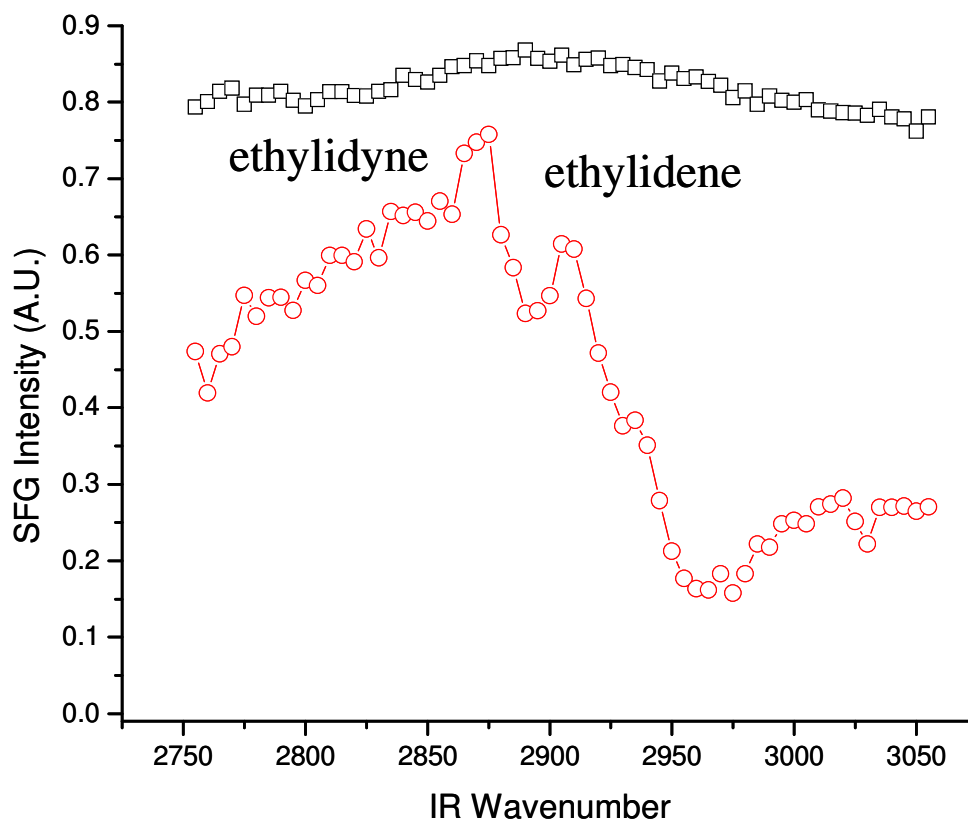


**Figure 9-4:** SFG spectra collected in *ssp* polarization of sapphire/nanoparticle interface in (□) flowing CO on as-synthesized sample, (○) after 5 oxidation/reduction cycles, and (Δ) in flowing hydrogen.

Adsorption of ethylene on clean Pt nanoparticle monolayers probed by SFG. The adsorption of ethylene on platinum has been extensively utilized as a probe molecule of

surface structure because different intermediates form as surface structure changes. The hexagonally ordered (111) face of platinum has been the most extensively studied surface.[27] Significantly less work has been conducted on other surfaces; Masel and coworkers have examined adsorption and decomposition of ethylene on a series of open and close packed surfaces.[28,29,30] These authors demonstrated a diverse surface intermediate chemistry as the structure of a series of Pt single crystals was changed. The adsorption of ethylene on small metal crystallites has also been studied extensively; in most cases the ability of ethylene surface chemistry to discern the surface structure of the small crystallites has not been possible. On Pt(111), the C-H stretching frequency of di-$\sigma$ bonded ethylene is ~2910 cm$^{-1}$, while at 2990 cm$^{-1}$, the C-H stretching of $\pi$-bonded species might be observed. Dehydrogenated species such as ethylidyne and ethylidene have also been observed on the Pt(111). These dehydrogenated species have a C-H stretching frequency of ~ 2880 and ~2960 cm$^{-1}$, respectively.[31] These species have been found to form on Pt(111) from low to high coverage at temperatures ranging from 90 K up to room temperature.

The adsorption of ethylene on a clean Pt nanoparticle array is shown in Fig. 9-5; two peaks arise at 2875 and 2910 cm$^{-1}$ associated with ethylidyne and di-$\sigma$-bonded ethylene. The surface structure of an ideal cube comprised of an fcc metal is identical to (100) oriented single crystal. The primary difference between these two structures is the occurrence of edge and corner atoms on the cubic nanoparticle, although at a particle size of 7 nm, the fraction of the surface atoms which are located at the edge and corner is small compared to the terrace atoms which have a cubic arrangement. The surface of (1 × 1)Pt(100) can reconstruct into a stable pseudohexagonal phase, (5 × 20)Pt(100) with a

surface structure similar to Pt(111) when prepared under the appropriate conditions.[32]  It

has been shown that both faces are stable to the adsorption of ethylene and upon heating.

Hatzikos and Masel have shown that the surface intermediates formed upon the

decomposition of low pressure ethylene are different; ethylidyne formed on the

pseudohexagonally reconstructed surface while high resolution electron energy loss

spectroscopy (HREELS) and temperature programmed desorption (TPD) provided

evidence for vinylidene and acetylinic intermediates on $(1 \times 1)$Pt(100).[33]  The spectra in

Fig. 9-5 compare very well with previous reported SFG spectra of ethylene adsorbed on a

Pt(111) single crystal.

**Figure 9-5:** SFG spectra collected in *ssp* polarization of the sapphire/nanoparticle interface after 5 oxidation/reduction cycles at 373 K in (□) oxygen, and (○) 700 torr ethylene.

## 9.4 Conclusion

Sum frequency generation (SFG) surface vibrational spectroscopy in total internal reflection geometry was employed to characterize the interaction of a surface templating polymer, poly(vinylpyrrolidone) (PVP) with a monolayer of platinum nanoparticles consisting primarily of cubes. Adsorption of carbon monoxide on a monolayer in which PVP was present resulted in a reduced adsorption capacity and a red-shift in the CO

stretching relative to CO adsorption on a clean Pt nanoparticle monolayer. A charge transfer mechanism in which PVP donates electron density into carbon monoxide mediated through the metal surface is supports the observed redshift. Adsorption of carbon monoxide on PVP capped nanoparticle tend to significant restructuring of adsorbed PVP which was reversible upon removal of CO by oxidation. Removal of PVP from the nanoparticle surface was accomplished with low temperature oxidation-reduction treatments. The adsorption of carbon monoxide and ethylene on clean nanoparticles was examined by SFG. Upon removal of PVP, there was a significant increase in the amount of adsorbed CO and a blue shift in stretching frequency relative to adsorption on the PVP covered monolayer. Adsorption of ethylene on the platinum nanoparticle monolayer led to an infrared spectrum with a similar lineshape to ethylene adsorbed on Pt(111). Two resonances in the spectrum were assigned to surface intermediates, ethylidyne and di-σ bonded ethylene; these results are surprising when compared with ethylene adsorption on Pt(100), in which a vinylidene species and not ethylidyne was postulated. The possible restructuring on the cubic nanoparticle surface to a pseudohexagonal phase is a possible explanation for the presence of ethylidyne on the Pt nanoparticle monolayer. The application of an inherently surface specific vibrational spectroscopy in total internal reflection geometry to the study of surfaces which are not optically flat is major advance in the application of sum frequency generation to relevant catalytic surfaces under in-situ reaction conditions.

# References

1 Strongin, D.R., Carrazza, J., Bare, S.R., and Somorjai, G.A. J. Catal. 1987, 103, 213.

2 Zaera, F. and Somorjai, G. A. J. Am. Chem. Soc. 106 (1984) 2288.

3 Schlatter, J. C.; Boudart, M. J. Catal. 24 (1972) 482.

4 Sinfelt, J. H. J. Phys. Chem. 68 (1964) 856.

5 Passos, F. B.; Schmal, M.; Vannice, M. A. J. Catal. 160 (1996) 118.

6 Carter, E. A.; Koel, B. E. Surf. Sci. 226 (1990) 339.

7 Grunes, J., Zhu, J., Yang, M., Somorjai, G. A., Catal. Lett. 2003, 86, 157.

8 Boudart, M. Adv. Catal. 1969, 20, 153.

9 Mavrikakis, M.; Bäumer, M.; Freund, H. J.; Nørskov, J. K. Catal. Lett. 2002, 81, 153.

10 Su, X., Cremer, P. S., Shen, Y. R., Somorjai, G. A. J. Am. Chem. Soc. 1997, 119, 3994.

11  McCrea, K. R., Somorjai, G. A. J. of Mol. Cat. A 2000, 163, 43.

12 Song, H.; Kim, F.; Connor, S.; Somorjai, G. A.; Yang, P. J. Phys. Chem. B 2005, 109, 188.

13 Baldelli, S.; Eppler, A. S.; Anderson, E.; Shen, Y. R.; Somorjai, G. A. J. Chem. Phys. 2000, 113, 5432.

14 Yu, R., Song, H., Zhang, X., Yang, P. J. Phys. Chem. B  2005, 109, 6940,

15

16 Rioux, R. M.; Song, H.; Grass, M.; Habas, S. E.; Niesz, K.; Hoefelmeyer, J. D.; Yang, P.;

Somorjai, G. A. Top. Catal. 2006, in press.

17 Wang, Z. L.; Petroski, J. M.; Green, T. C.; El-Sayed, M. A. J. Phys. Chem. B 1998, 102,

6145.

18 Peek, P. S.; McDermott, D. P. Spectrochim. Acta, Part A 1988, 44, 371.

19 Borodko, Y.; Habas, S. E.; Koebel, M.; Yang, P.; Frei, H.; Somorjai, G. A., to be

submitted.

20 Yoshida, M.; Prasad, P. N. Appl. Optics 1996, 35, 1500.

21 Rioux, R. M.; Song, H.; Hoefelmeyer, J. D.; Yang, P.; Somorjai, G. A. J. Phys. Chem. B

2005, 109, 2192.

22 Du, Y.K., Yang, P., Mou, Z.G., Hua, N.P., Jiang, L., J. Of Appl. Poly. Sci. 2006, 99, 23.

23 Rioux, R. M.; Toops, T. J.; Grass, M.; Niesz, K.; Kuperman, A.; Yang, P.; Somorjai, G.

A. To be submitted (2006).

24 Westerberg, S., Wang, C., Chou, K., Somorjai, G. A. J. Phys. Chem. B 2004, 108, 6374.

25 Campbell, C. T.; Ertl, G.; Kuipers, H.; Segner, J. J. Chem. Phys. 1980, 73, 5862.

26 Blyholder, G. J. Phys. Chem. 1964, 68, 2772.

27 Deng, R.; Herceg, E.; Trenary, M. Surf. Sci. 2004, 560, L195.

28 Backman, A. L.; Masel, R. I. J. Vac. Sci. Technol. A 1988, 6, 1137.

29 Yagasaki, E.; Backman, A. L.; Chen, B.; Masel R. I. J. Vac. Sci. Technol. A 1990, 8,

2616.

30 Backman, A. L.; Masel, R. I. J. Phys. Chem. 1990, 94, 5300.

31 Cremer, P.; Stanners, C.; Niemantsverdriet, J. W.; Shen, Y. R.; Somorjai, G. Surf. Sci.

1995, 328, 111.

32 Rønning, M.; Bergene, E.; Borg, A.; Ausen, S.; Holmen, A. Surf. Sci. 2001, 477, 191.

33 Hatzikos, G. H.; Masel, R. I. Surf. Sci. 1987, 185, 479.